Mechanobiology of Jamming: From Collective Migration to Mechanically Tunable Hydrogels

by

Grace Cai

A dissertation submitted in partial fulfillment
of the requirements for the degree of
Doctor of Philosophy
(Applied Physics)
in The University of Michigan
2023

Doctoral Committee:

Associate Professor Allen Liu, Chair
Professor Gary Luker
Associate Professor Geeta Mehta
Associate Professor Ann Miller
Associate Professor Qiong Yang

Grace Cai

gcai@umich.edu

ORCID iD: 0000-0003-4925-3116

Dedication

To my family, friends, and mentors

Acknowledgements

I would like to acknowledge my mentors, collaborators, family, and friends for their support throughout my PhD journey. I would like to thank my advisor, Dr. Allen Liu, for providing the encouragement and support that allowed me the freedom to explore different research topics and career paths. I would also like to thank my committee members, Dr. Ann Miller, Dr. Gary Luker, Dr. Geeta Mehta, and Dr. Qiong Yang, for their valuable feedback on my research and genuine interest in my career development. I would like to thank my undergraduate advisor, Dr. Kerstin Nordstrom, who encouraged me to apply for graduate school. I would like to acknowledge my collaborators, Dr. Max Bi, Dr. Xinzhi Li, and Anh Nguyen, whose contributions have been invaluable to my work. I would like to thank the members of the Liu lab, past and present, for creating an enjoyable lab atmosphere. I would also like to thank Olga and Jenny for providing perspective on my work at different stages of my journey. Special thanks to Pa Chia, Yen-Yu, Sung-Won, Hossein, and Sizhen who have always lent a listening ear and been a strong support system during the challenging times of graduate school. To my family, I am always grateful.

Table of Contents

List of Figures

Abstract

Cellular unjamming refers to the coordinated fluid-like motion of cells and has significant implications in various biological processes such as development, wound healing, and tumor progression. One of the contexts in which cellular unjamming becomes crucial is in tumor growth, where the unchecked proliferation of cancer cells within a confined space generates compressive stress. Since multiple cellular and molecular mechanisms are potentially operating simultaneously in this space, the predominant mechanism by which a densely packed monolayer or 3D aggregate of mechanically stressed cells can unjam is unknown. Furthermore, while cells within a multicellular aggregate are known to segregate into distinct groups based on their differential adhesive properties, the physical attributes in the tumor microenvironment that drive tumor-cell sorting and subsequent invasion remain poorly understood.

First, I investigate the role of cell-cell adhesion in unjamming transitions within a mechanically stressed monolayer and establish that increased collective cell migration is correlated with cell shape and distinct from the well-known epithelial-to-mesenchymal transition (EMT). Cell-cell adhesion plays a vital role in the transition to a fluidized state, resulting in increased collective motion and accelerated wound repair while maintaining epithelial characteristics. E-cadherin knockdown inhibits coordinated migration under mechanical compression, demonstrating that the unjamming transition is not primarily driven by EMT but rather by increased cell-cell adhesions and reduced traction forces within the bulk cell sheet. The findings provide a novel perspective on tumor development and cancer invasion, suggesting that compressive stress inhibits normal epithelial cell migration but enables cancer cells to migrate rapidly as a cohesive collective.

Next, I will investigate how matrix stiffness can regulate cell invasion and the sorting of

two cell types with different adhesiveness into the core and periphery of 3D spheroids. ECM stiffness is known to influence cancer spread and metastasis, and I demonstrate that single-cell cancer migration is restricted by high confinement. Moreover, matrix stiffness directly impacts 3D spheroid sorting, in addition to individual and collective cell invasion. Spheroid sorting leads to high local cell density in the core, where cells strengthen cell-cell adhesions, reduce volume, and exhibit jammed behavior. In contrast, less adhesive mesenchymal cells occupy the outer edges of the spheroid in an unjammed state, enabling rearrangements within the compartment boundary. My findings show that pressure-driven burst-like collective cell motion is observed when matrix confinement is lowered for sorted spheroids, allowing rapid escape into the surrounding matrix. This has significant implications for cancer cells sorted to the tumor periphery that proceed to degrade the matrix and ultimately induce burst-driven cell invasion.

Thus, my dissertation establishes compressive stress-mediated and adhesion-dependent collective cell behavior in both 2D and 3D contexts. Together, the findings shed light on the impact of compressive stress and matrix stiffness on the mechanisms of collective cell motion in cancer migration, tumor development, and distant metastasis. By improving our understanding of the mechanical inputs and forces contributing to collective migration in 2D and 3D settings, I hope that this research will lead to the development of improved therapies targeting cancer cell sorting and migration in the primary tumor.

Chapter 1 Introduction

1.1 Jamming in wound healing and cancer cell invasion

Jamming was initially introduced to explain the behavior of grains, colloids, and foams, and describes a transition from a solid-like state to a fluid-like state (*1–5*). In collective granular systems, jamming represents a transition from a flowing state to a rigid state (*2*, *3*). These transitions have been observed in a wide variety of systems, ranging from molecular liquids to granular matter to soft materials (*3*, *6*). In the process of jamming, the viscosity of granular particles, such as coffee beans or sand grains, increases with density. As the particles become denser, they undergo a phase transition in which friction between particles slows them down, hinders neighbor exchanges, and causes the material to become more viscous or solid-like (*1*, *4*, *7*). Squeezed grains become so tightly packed that they lose their ability to flow and maintain their shape (*8*). In soft matter and glassy materials, the density, temperature, and load (e.g., shear stress) are key parameters controlling the transition between an unjammed, deformable state and a jammed, solid-like state (*1*). These systems can become unjammed by reducing density, increasing temperature, or applying a load. Jamming goes beyond simple physical examples and has applications in understanding human movement, traffic, and even biological tissues (*9–12*).

Collective migration occurs at different scales in both natural and artificial systems and involves the movement of groups of individuals that move together and influence each other's behavior (*13–15*). The interactions between individuals migrating collectively result in emergent

behavior, leading to phenomena such as flocking patterns in birds or swirling motions in swarming bacteria, which are not seen during individual migration (*15*). In cellular systems, jamming is associated with the arrest of collective cell migration. Jamming is an inhibiting mechanism that describes a rigidity transition caused by the mutual hindrance of cells (*16–18*). In the context of cancer, most invasive cells infiltrate collectively, and cancer aggression is more closely linked to collective cell migration than to single-cell migration (*12, 19–21*). The process of jamming occurs when cellular rearrangements are diminished, and the cells become constrained by their neighbors (*18*). Consequently, jamming can arrest collective cell migration in both developmental and disease events.

While cancer is a collective phenomenon, most biological approaches to treatment are highly specific and target the disease at a single-cell level (*22, 23*). Although the immune system can eliminate the vast majority of individual cancer cells, most invasive cancers infiltrate as a collective group (*24*). Additionally, metastatic cells typically detach from tumors as aggregates (*22*). The mechanism behind how the collective migration of a group of cancer cells within a primary tumor enables them to leave the tumor and infiltrate other parts of the body remains an important area of research.

Compared to inanimate systems such as fluids and grains, cells and tissues are significantly more complex. The jamming transition in inert granular materials shares similar features with the loss of motility in the migrating epithelial layer (*10, 16–18*). In recent decades, there has been growing evidence that this behavior plays a vital role not only in tissue formation and maintenance but also in disease progression (*12, 20, 25–27*).

1.1.1 Cell jamming occurs at high cell density

The movement of cells as a cohesive and coordinated group during collective migration is crucial for essential biological processes such as embryogenesis, wound repair, and cancer metastasis (*25, 28, 29*). While biochemical signaling pathways play a role in regulating cellular dynamics, physical interactions between cells and their environment are also significant determinants of cellular behavior (*30, 31*). A hypothetical phase diagram has proposed physical control parameters for cell jamming: 1/density, 1/cell-cell adhesion, and motility (**Figure 1.1**) (*16*). When cells are sparse, they behave like a fluid, but as they proliferate, mutual crowding leads to a slowing down and eventual arrest of cell motion in a dense monolayer (*9*). As the cell monolayer matures, it undergoes a phase transition from a flowing state to a jammed state. This process plays a critical biological role in the development of tissue elasticity and the formation of protective barriers in epithelial tissue (*11, 26*). Additionally, in cancer, jamming acts as a suppressive mechanism for tumor growth (*12, 19*).

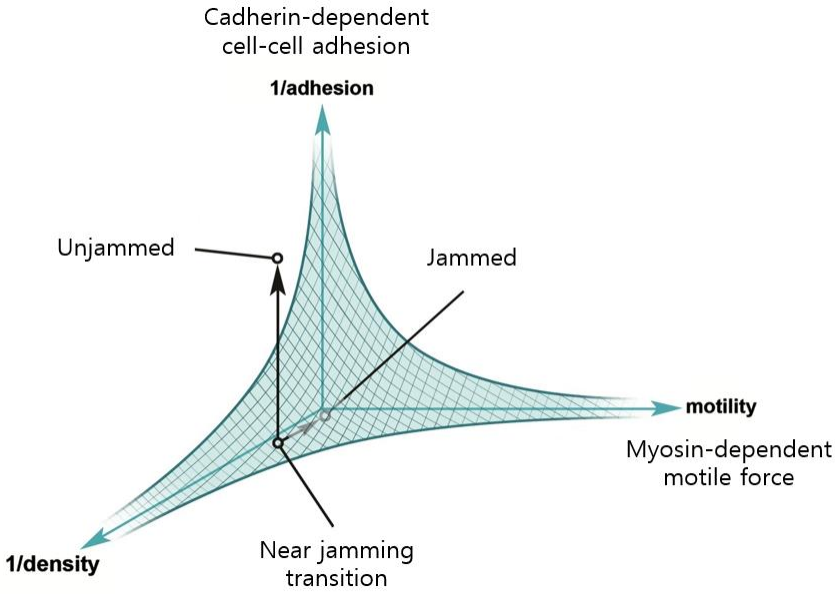

Figure 1.1. Hypothetical phase diagram for cell jamming.

Higher cell density, stronger cell-cell adhesion, or reduced cell motility results in jamming. The transition towards cell jamming is represented by the shaded region. Near the jamming transition, cells form larger and slower clusters with increasing density as they approach the jammed state. Adapted from ref (*16*).

Cell jamming describes the transition of cells from a migrating to a resting state during collective migration. An increase in cell density is a crucial contributing factor among the various routes to cell jamming (*11, 16*), and the jamming transition occurs at a packing density of one for a 2D cellular system at confluence (*19*). When the packing density reaches one, cells are densely packed and occupy all available space within a tissue, and further compression requires substantial external force. Experimental observations of cell jamming often involve tracking the evolution of a cell monolayer in a confined space over time (*9*). A simple method to reduce cell density is to create a wound, which allows cells at the boundary of the wound to invade and, consequently, prompts the jammed monolayer to rapidly revert to a flowing state (*32*). Wound-induced unjamming transitions have been observed in various cell types, including epithelial, endothelial, and cancer cells (*26*).

1.1.2 Cell shape determines density-independent jamming transitions

In cellular systems where density and space are not determining factors, such as flat tissues with closely packed cells, the behavior of the tissue can be predicted solely by cell shape (*33, 34*). Clinical studies have shown that epithelial tissues derived from non-asthmatic patients tend to become jammed and behave like solids, but this jamming is either delayed or absent in tissues from asthmatic patients (*35*). These different states are heavily dependent on cell shape.

In confluent tissues, the transition between jammed and unjammed states arises from the competition between fluctuations and cell-shape-induced geometric frustration (*11*). Cells in

jammed tissues may fluctuate, but they do not exchange places with their neighbors due to the balance of propulsive forces and adhesion, which limits cell motion (*36*). On the other hand, unjammed tissues frequently experience cellular rearrangements, in which increased force fluctuations and adhesion together contribute to unjamming. However, regardless of the magnitude of active fluctuations, tissues become jammed when the shape index approaches a critical value (*18, 34, 35*). Computational studies using a 2D vertex model of the cell layer have demonstrated that jamming is controlled by the preferred cell shape, with the mechanical energy associated with each cell depending on the cell area, perimeter, and cell-cell contact interfaces (*18*). The vertex model represents each cell in 2D as an irregular curved polygon with a shape index, where changes in cell shape are necessary for cells to exchange places with their neighbors. This change in energy defines an energy barrier, and as the shape index approaches the critical value of 3.81, cells become jammed (**Figure 1.2**) (*18, 35*).

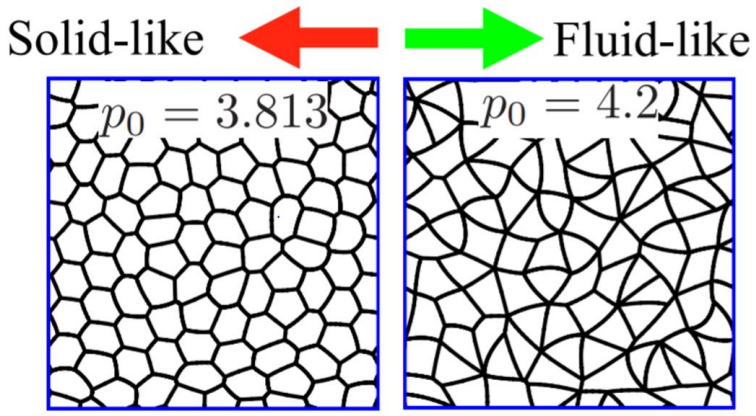

Figure 1.2. Jamming is controlled by the preferred cell shape.

Simulated tissues with input parameters of target cell shape index p_0 = 3.813, corresponding to a jammed tissue (left), and p_0 = 4.2, corresponding to a fluidized state (right). Cell shape index is calculated by $cell\ perimeter/\sqrt{projected\ cell\ area}$.

Adapted from ref (*35*).

During collective cell migration, cells move as cohesive sheets relying on E-cadherin-based cell-cell junctions, actomyosin contractility, and multicellular front-rear polarity (*30, 37–39*). Cells can invade by downregulating E-cadherin, losing contact with other cells, and migrating as single cells (*29*). In contrast, by retaining E-cadherin expression, cells can migrate collectively. Experimental observations suggest that jamming is associated with increased adhesion. As a cell monolayer ages, cell movement slows down monotonously, and cell-cell and cell-substrate adhesions strengthen, while the velocity correlation length first increases and then decreases, indicating the slowest motions (*9*).

1.1.3 Unjamming transition vs. epithelial-to-mesenchymal transition

Unjamming is the collective fluidization of cell motion and represents crossing the phase boundary from the other side (*35*). It is a distinct process from motility induction driven by chemoattractants, electrical currents, and wound formation (*26*). The unjamming transition describes the collective flow and rearrangement of the epithelial layer and has been linked to various biological processes, including development, wound repair, tumor growth, and metastasis (*40–42*).

In situations where cells are confined and densely packed, such as in tumors, they may undergo different modes of migration in response to physical forces exerted on the cells by the tissue microenvironment (*43–47*). One example of this is the epithelial-to-mesenchymal transition (EMT), where epithelial cells lose cell polarity and cell-cell adhesion and acquire invasive properties (*29, 46, 48*). Epithelial migration is characterized by strong cell-cell junctions and focal adhesions, while mesenchymal migration involves weak cell-cell adhesions and decreased focal adhesions in follower cells (**Figure 1.3**) (*48*). Studies have found that applying compressive stress

to a monolayer of primary human bronchial epithelial cells stimulates a jammed-to-unjammed transition, which is not primarily driven by EMT (*35*, *49*). This demonstrates the distinct nature of the unjamming transition.

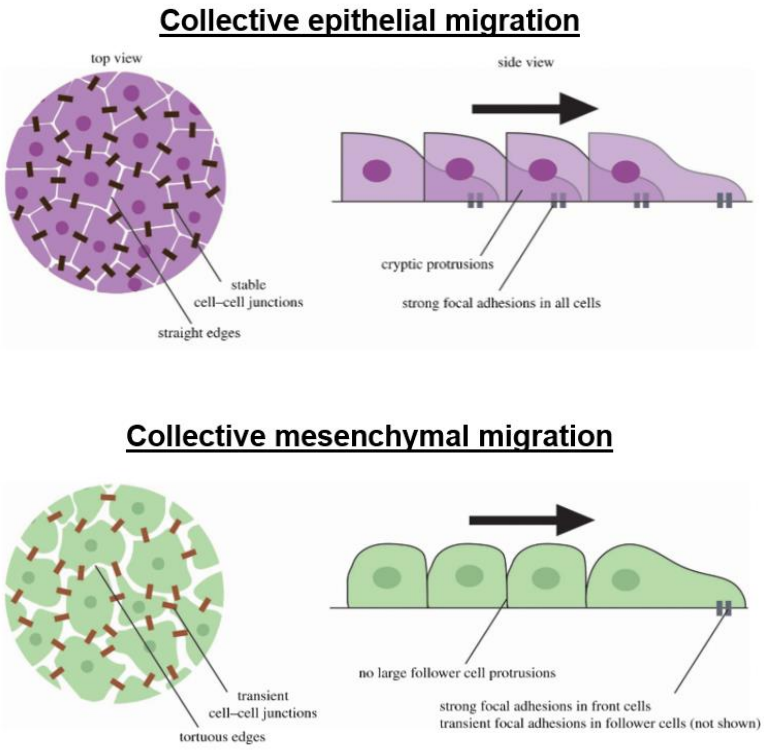

Figure 1.3. Collective migration of unjammed epithelial and mesenchymal cells.

Top panel: epithelial migration consists of collectively migrating cells with intact intercellular junctions and epithelial markers like E-cadherin. Leader cells form forward protrusions and are aided by follower cells' traction. Bottom panel: mesenchymal migration results from epithelial-to-mesenchymal transitions, causing weaker adhesions and gene expression changes (E-cadherin to N-cadherin). Adapted from ref (*15*).

Epithelial and mesenchymal cells display contrasting collective behaviors. Epithelial cells, when jammed in position, lack the energy to overcome high junctional tension (*40*). Unjamming

occurs when tension is reduced and cell adhesion is high, resulting in a tightly bound group where all cells contribute equally to collective movement (*50*). On the other hand, mesenchymal cells migrate as a loosely connected pack, resembling collective motion of animals, bacteria, and self-propelled particles (*15*). During EMT, intercellular adhesions weaken, and epithelial adhesion markers such as E-cadherin are replaced by the upregulation of N-cadherin. Leader cells maintain strong focal adhesions, while follower cells experience weakened adhesions and reduced traction forces (*29*). In contrast, unjammed cells maintain strong cell-cell junctions while exhibiting fluid-like collective motion characterized by elongated cell shapes (*49*).

1.2 Cell migration in 2D vs. 3D

Cell migration depends on multiple factors, including dimensionality, cell morphology, cell-cell and cell-ECM interactions, and modes of migration (*51–54*). To overcome the limitations of current imaging tools in studying cell migration in vivo, researchers have developed 2D and 3D tissue model systems to study cell motility in vitro (*55*). In a 2D environment, cells move on a flat surface and are confined to a single plane. They exhibit an elongated and spread-out morphology and primarily use focal adhesions to interact with the ECM on their basal side (*51*). Transitioning from 2D glass and plastic dishes to 3D hydrogels and tissues leads to a significant decrease in substrate stiffness, from a GPa to kPa range (*55*). In 3D matrices, cells tend to have a more rounded and amoeboid morphology and encounter complex barriers and gradients due to the surrounding matrix components (*56–58*). As a result, they tend to migrate more slowly and take irregular paths due to the resistance posed by the ECM. Notably, the ability of cells to interact with surrounding cells and the ECM on all sides changes in 3D environments, increasing cell-cell and cell-ECM interactions and leading to collective behavior (*58*). In 3D settings, cells tend to develop smaller and

more dispersed focal adhesions, which show rapid turnover and remodeling that facilitate cell migration and tissue invasion.

Cell migration in 3D is often enabled by proteolytic degradation or the alignment of ECM fibers via integrin-mediated cell pulling (*59*). The porosity of the ECM determines the space through which cells will squeeze, and squeezing the nucleus can trigger changes in gene expression and potentially cause nuclear rupture, leading to DNA damage and cell death (*60*). This mechanical compression can activate mechanosensitive pathways and influence the expression of genes related to stress response, inflammation, and cell fate. Interestingly, cancer cells possess a softer nucleus compared to cells in healthy tissue (*61*).

In 3D environments, cells encounter signaling gradients, mechanical resistance, and varying matrix density, which result in distinct migration responses compared to cells in 2D systems (*57, 58*). For example, while 2D monolayer models provide a controlled setting for studying cellular interactions, they exhibit higher susceptibility to chemotherapeutic agents when compared to 3D embedded conditions (*62*). This difference in drug response can be attributed to the formation of complex and dense cell structures and the ECM and neighboring cells acting as diffusional barriers, which can limit drug penetration. As a result, the 2D culture system may not accurately represent the response to treatments and the transfer of small molecules observed in vivo.

1.2.1 Modes of 3D cell migration

3D cell migration by individual cells and groups of cells plays a critical role in tissue and organ formation as well as cancer invasion (*54, 63*). While 2D cell migration generally involves lamellipodial or filopodial protrusions at the leading edge and the formation of focal adhesions, migration modes in 3D environments can vary significantly based on the mechanical properties of

the surrounding ECM. Migration through 3D environments presents challenges as cells must navigate dense and complex ECMs, requiring them to adapt to the mechanical properties of the matrix through remodeling or degradation (*60*). In such environments, interactions between neighboring cells and between cells and the surrounding matrix are increased. For collective migration, cells need to maintain interactions with the surrounding tissue as well as other cells in a group (*64*). Various modes of migration are observed in 3D settings, including mesenchymal, amoeboid, and lobopodial migration (*54*).

Mesenchymal migration is characterized by elongated cell morphology and is commonly observed during development and tissue repair. Cells use actin polymerization to generate lamellipodia or filopodia that protrude at the leading edge and secrete proteolytic enzymes like matrix metalloproteinases (MMPs) to remodel the ECM, creating paths for migration (*54, 65*). They typically adhere to and move along ECM fibers, such as collagen and fibronectin, and exhibit front-rear polarity, with the cell moving forward by contracting its rear end and pulling itself in the direction of migration (*60*).

Amoeboid migration, on the other hand, is faster, lacks prominent protrusions, and involves minimal proteolytic degradation (*66*). Rapidly moving amoeboid cells, such as leukocytes, are highly deformable and migrate by selecting the path of least resistance in terms of ECM pore size (*67*). They possess a rounded morphology, exhibit weak adhesions, and use actomyosin contractility to generate the force required to squeeze through ECM pores (*59*). Actin protrusions or hydrostatic membrane blebs drive deformations of cell shape and push the cell forward (*65*). Cancer cells often use amoeboid migration to infiltrate surrounding tissues and metastasize to distant sites (*68*). Associated with amoeboid movement, lobopodia are blunt cylindrical protrusions that extend from the leading edge of a migrating cell and are driven by intracellular pressure (*69*). Migration in this

mode is driven by the assembly of actin filaments at the leading edge, which adhere to the ECM and provide traction for forward movement, while actin filaments at the rear of the cell disassemble. In 3D environments, cells tend to utilize lobopodia instead of lamellipodia and filopodia commonly observed in 2D settings (*70*).

Cells can switch between the different modes of migration depending on the cell type, the properties of the surrounding ECM, and biochemical signaling cues. For instance, cells can switch between migration modes in response to protease inhibition, viscoelastic properties, adhesion strength, and confinement level (*68*, *71*). Understanding these diverse migration modes and their regulation is essential for gaining insights into tissue development and repair, as well as cancer progression.

1.2.2 From cell sorting to invasion

Tissues usually comprise multiple cell types that cooperate to perform specific functions and uphold tissue integrity. Understanding the interactions and organization of different cell types provides insights into development and disease processes, which can pave the way for targeted therapeutic interventions. Cell sorting is a significant biological event in tissue development, morphogenesis, tumor growth, invasion, and the formation of complex structures like organoids (*72*). Sorting refers to the spatial organization of cells based on their adhesive and mechanical properties (*73*).

The differential adhesion hypothesis (DAH) proposes that cells behave dynamically like a fluid, and that cells with higher adhesion tend to aggregate together and become surrounded by cells with weaker adhesion (*74*, *75*). The latter cells are more likely to segregate or form separate clusters, while the highly adhesive cells preferentially adhere to each other. The final sorted state corresponds

to an equilibrium thermodynamic state with minimum free energy (*74*). An extension to the DAH is the differential interfacial tension hypothesis (DITH), which states that differential adhesion, together with differences in cortical tension due to actomyosin contractility, can predict sorting behavior (*72*). Surface tension in spheroids is determined by the ratio of adhesion tension to cortical tension. Cell stiffness and contractility can also lead to sorting, with stiffer and more contractile cells congregating in clusters and displacing softer cells (*73*, *76*).

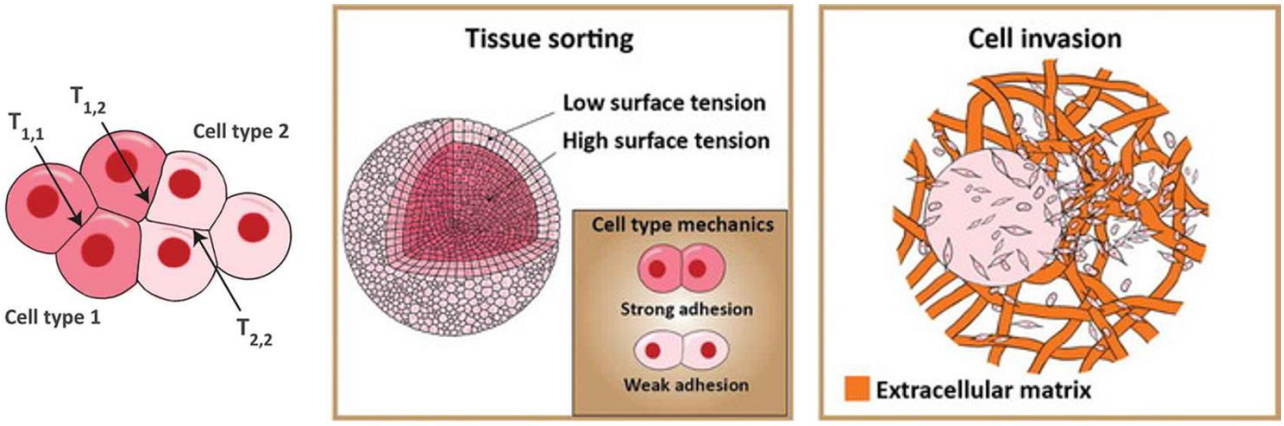

Figure 1.4. Surface tension in a multicellular aggregate.

Left panel: schematic of contact tension in tissues, showing differences in homotypic tensions $T_{1,1}$ and $T_{2,2}$ and heterotypic tension $T_{1,2}$. Middle panel: tissue spreading is governed by relative surface tensions influenced by differences in cell adhesion, with lower surface tension tissues enveloping those with higher surface tension. Right panel: the rearrangement of cells based on intercellular adhesion can affect the direction and efficiency of invasion. Adapted from ref (*77*).

The spatial arrangement of cells has a critical impact on cell migration, especially in fibrous 3D matrices, where physical barriers and chemoattractant gradients become more complex. While individual cells may invade using mesenchymal or amoeboid migration, groups of sorted cells can collectively invade by maintaining strong cell-cell adhesions (*78*). Cancer cell migration is a key element of the invasion-metastasis cascade, where invasive cells secrete matrix-degrading enzymes

and extend protrusions to promote migration (*60, 65*). In soft collagen matrices, cancer aggregates have been observed to display increased pressure within the aggregate due to cell swelling caused by the matrix's insufficient mechanical feedback in response to cell pulling forces (*79*). In cancer metastasis, pressure within the tumor can cause cells to break away from the primary tumor and invade surrounding tissues (*80*). Understanding the molecular mechanisms underlying cell sorting and invasion is crucial for inhibiting invasive behavior in disease processes.

1.3 Spheroids as 3D multicellular model systems

To replicate in vivo behavior, more complex cell culture models are required for tissues and tumors. Spheroids are widely used in vitro 3D multicellular models that mimic tissues, providing valuable insights into cellular mechanics and various biological events, including morphogenesis, tissue remodeling, tumor growth, and cancer metastasis (*62, 81–83*). Compared to traditional 2D cell culture, spheroids more accurately replicate the architecture and microenvironment of tissues and tumors, allowing the study of cell-cell and cell-ECM interactions, signaling, and migration in a more physiologically relevant context (*81, 84*).

Spheroids are formed by aggregating cells, which self-organize due to cell-cell adhesion forces and lack of attachment to a substrate. Several methods, such as hanging drop cultures, low-attachment plates, and bioprinting, can be used to generate spheroids (*81*). They are valuable model systems because they closely resemble in vivo structures, exhibiting cell-cell contacts, nutrient and oxygen gradients, and an outer layer of proliferating cells surrounding a quiescent core (*84, 85*). Increased intercellular interactions in spheroids enhance cell-cell communication and signaling compared to 2D monolayers and provide a more relevant model for studying tumor behavior and cell invasion. However, spheroids larger than 500 μm in diameter experience cell death in the core

due to inadequate nutrient and oxygen penetration (*86*).

While single-cell mechanics depends on cytoskeletal and plasma membrane properties, spheroid mechanics are influenced by the relationship between cell adhesion, the cytoskeleton, and the ECM. For instance, the Yes-associated protein (YAP) is a transcriptional regulator known as a universal mechanotransducer, as demonstrated in 2D culture studies where YAP localizes to the nucleus and activates the expression of YAP target genes (*87, 88*). However, recent research revealed that YAP does not mediate mechanotransduction in 3D cultures of breast cancer patient samples (*88*).

In 3D cultures, the presence of a matrix and ECM density have a significant impact on spheroid topology. Spheroids grown in suspension exhibit an apical-out topology, whereas those encapsulated in collagen gel show an apical-in topology (*77*). Similar reverse topology patterns have been observed in colon cancer, where large clusters of cancer epithelial cells display an apical-out topology, differing from the apical-in topology seen in normal epithelial cells (*89*). These observations underscore the value of spheroids as essential tools for studying complex cellular behaviors within a 3D context. Overall, spheroids offer a more physiologically relevant model system for studying cellular interactions and responses in a 3D environment.

1.4 Mechanical properties of the tumor microenvironment regulate cancer cell migration

The tumor microenvironment is a complex system comprising diverse cellular and extracellular components, including tumor cells, stromal cells, immune cells, carcinoma-associated fibroblasts, and non-cellular components within the ECM (*45, 90, 91*). In addition to biochemical signals, physical cues from the microenvironment can significantly impact cell proliferation,

migration, and metastatic potential (*91–93*). The ability of cells to migrate collectively is influenced by microenvironmental conditions, such as cell density and ECM properties. Tumors are often stiffer than normal tissue due to increased concentrations of ECM components such as collagen and fibronectin (*94*). Mechanical inputs, such as ECM stiffness or interstitial pressure, and mechanical forces, including tension and compression, have been shown to modulate cancer cell metabolism, proliferation, migration, and stemness (*94*, *95*).

In 3D environments, cells encounter various degrees of physical confinement in tissues, as well as mechanical forces like compressive and shear stresses during both single and collective cell migration (*47*). High mechanical stress in tumors can prompt cancer cells to acquire stem-like cell properties, driving tumor progression and promoting metastasis (*96*). The mechanical properties of the tumor microenvironment, such as solid stress, matrix stiffness, and interstitial fluid flow, change as tumor growth and development occur. Compressive stress in human tumors can reach levels of 35-142 mm Hg, impacting cancer cells and surrounding blood and lymphatic vessels (*96*). While spheroid models replicate multicellular tissues, hydrogels replicate the tissue microenvironment, which is essential for investigating tumor growth and cell invasion under relevant physical forces such as confinement.

1.4.1 Matrix stiffness and physical confinement guide cell migration

The cellular ECM is a complex network of proteins and fibers, including collagen, elastin, and fibronectin, with mechanical properties that vary depending on tissue type. Mechanosensitive proteins like integrins and focal adhesion kinase play a crucial role in converting mechanical signals from the cellular microenvironment into biochemical cues that guide cell migration (*97*). Of particular significance is the impact of changes in matrix stiffness on cell behavior and migration,

mediated through mechanotransduction pathways and signaling mechanisms. Notably, breast cancer tissue is significantly stiffer (~4 kPa) than normal breast tissue (~0.2 kPa), emphasizing the role of mechanical cues in cancer progression (*98*). Studies have shown that cells cultured on stiffer substrates exhibit an elongated morphology, increased spreading, and faster migration due to enhanced contractile forces generated on rigid surfaces (*99*). Cells establish stronger cell-ECM adhesions and traction forces, resulting in rapid and efficient migration.

ECM stiffening is driven by the excessive activity of proteins and enzymes, leading to crosslinking of collagen fibers and other ECM components (*100–102*). For instance, hepatic fibrosis results from the high accumulation of ECM due to hepatic stellate cell activation in response to liver damage (*103*). In the context of confined 3D cell migration, cells can actively remodel and degrade the surrounding matrix to create migration pathways (*60, 101*). The stiffness and porosity of the ECM influence the degree of physical confinement experienced by cells. In response to different levels of confinement, cells may switch their migration mode between mesenchymal and amoeboid migration (*68, 71*). Amoeboid migration is favored when navigating tight gaps in dense tissues, whereas mesenchymal migration is typically employed in less dense environments. Moreover, increased physical confinement stemming from high matrix stiffness can result in cell nucleus deformation, leading to changes in cell polarity and gene expression (*60*).

1.4.2 Hydrogel microenvironments for modeling tumor-cell invasion and migration

Hydrogels have emerged as valuable tools for modeling tumor invasion and studying cancer progression in a physiologically relevant manner, as they can mimic the ECM of tissues. Commonly used hydrogels, such as those based on collagen and Matrigel, offer cell adhesion sites and closely resemble the ECM, providing a favorable environment for cell interactions and exhibiting inherent

bioactivity (*104–107*). For example, Type I collagen is the most abundant collagen type in many tissues and serves as a major structural component (*108*).

In natural hydrogels, cell-mediated proteases, such as MMPs, lead to degradation (*109*). This process can be replicated in synthetic hydrogels by using peptide crosslinkers designed to degrade in response to MMPs (*107, 110*). Synthetic hydrogels are widely used due to their biocompatibility and tunable properties. They can be modified with specific cell-adhesive ligands to mimic the ECM and support cell adhesion and migration (*105*). Additionally, the mechanical stiffness of synthetic hydrogels, such as polyethylene glycol and polyacrylamide, can be adjusted to match the stiffness of different tissues (*111, 112*). One significant advantage of synthetic hydrogels is the ability to tailor their mechanical and chemical properties to specific requirements. Different polymerization techniques and functional groups can be employed to provide greater control over tuning the mechanical properties of the hydrogel.

To further replicate the tumor microenvironment, hybrid hydrogels can be created by combining components of natural and synthetic hydrogels (*113*). This allows for the incorporation of natural ECM components and fine-tuning of mechanical properties, chemical composition, and degradation rates, resulting in a closer representation of the complex tumor microenvironment. Moreover, the use of synthetic components can improve batch-to-batch consistency in large-scale production (*114*).

1.5 Dissertation outline

I use a combination of experimental and modeling approaches to understand the role of mechanobiology in regulating collective migration and jamming transitions in both 2D and 3D contexts. In Chapter 2, I discover that compressive stress induces a jamming to unjamming

transition for faster wound healing of breast cancer cells in a mechanism that is distinct from EMT. Compressive stress is found to accelerate the collective migration of breast cancer cells via an increase in E-cadherin-mediated cell-cell adhesion and corresponding changes in cell shape that are correlated with unjamming. In Chapter 3, I develop a 3D co-culture spheroid model encapsulated in a composite hydrogel with tunable mechanical properties to examine the impact of confinement stress on cell sorting and migration in tumors. In Chapter 4, I discuss the implications of my findings in the context of incorporating mechanobiology to the parameters governing jamming and unjamming transitions in 2D and 3D cellular systems and explore future directions in the field.

Chapter 2 Compressive Stress Drives Adhesion-Dependent Unjamming Transitions in Breast Cancer Cell Migration

The results of this chapter were published in Frontiers in Cell and Developmental Biology (2022). G.C. and A.P.L. contributed to conception and design of the study. A.N. and D.B. contributed to the simulation study. G.C. and Y.B. contributed to methodology and formal analysis of the work. G.C., A.N., D.B., and A.P.L. contributed to the original draft, and S.-S.L. contributed to review and editing. D.B. and A.P.L. provided supervision and administered the project.

2.1 Abstract

Cellular unjamming is the collective fluidization of cell motion and has been linked to many biological processes, including development, wound repair, and tumor growth. In tumor growth, the uncontrolled proliferation of cancer cells in a confined space generates mechanical compressive stress. However, because multiple cellular and molecular mechanisms may be operating simultaneously, the role of compressive stress in unjamming transitions during cancer progression remains unknown. Here I investigate which mechanism dominates in a dense, mechanically stressed monolayer. I find that long-term mechanical compression triggers cell arrest in benign epithelial cells and enhances cancer cell migration in transitions correlated with cell shape, leading us to examine the contributions of cell-cell adhesion and substrate traction in unjamming transitions. I show that cadherin-mediated cell-cell adhesion regulates differential cellular responses to compressive stress and is an important driver of unjamming in stressed monolayers. Importantly,

compressive stress does not induce the epithelial—mesenchymal transition in unjammed cells. Furthermore, traction force microscopy reveals the attenuation of traction stresses in compressed cells within the bulk monolayer regardless of cell type and motility. As traction within the bulk monolayer decreases with compressive pressure, cancer cells at the leading edge of the cell layer exhibit sustained traction under compression. Together, strengthened intercellular adhesion and attenuation of traction forces within the bulk cell sheet under compression leads to fluidization of the cell layer and may impact collective cell motion in tumor development and breast cancer progression.

2.2 Introduction

Cell jamming impacts many fundamental biological and disease processes including embryogenesis (*13*), tissue repair (*27*, *115*), and tumor growth (*44*, *93*). A jamming transition is a transition from a solid-like state to a fluid-like state in which cellular rearrangements are diminished. Jamming transitions during embryogenesis are typically governed by cell density (*12*). As a monolayer ages, cells proliferate, slow down, and become jammed as a dense cell layer. Jammed cells are observed to be confined in "cages" of the size of a single cell by their neighbors (*9*), and the friction between cells increases, leading to reduced collective and individual motion. A dense cell layer in a solid-like state can quickly revert to a flowing state when a wound is inflicted (*32*). During wound repair, the ability for cells to rearrange is essential for closing gaps in epithelial tissues and may be regulated by jamming transitions. Although jamming plays a crucial role in many biological events, the main parameters of cell jamming remain poorly understood.

Recent research suggests cellular unjamming is involved in tumor growth and cancer progression (*20*, *116*, *117*). During tumor growth, cancer cells proliferate in a dense and confined

environment, subjecting tumor cells to solid compressive stress (*118*). Solid stresses affect tumor pathophysiology by directly compressing cancer and stromal cells and indirectly deforming blood and lymphatic vessels (*47*). For tumors to grow and proliferate, cancer cells must be able to divide and move, and cells in parts of the tumor can fluidize and migrate collectively in an unjamming transition. Here I investigate the idea that unjamming transitions in cancer cells are driven by compressive stress. As solid stress increases within a tumor, microenvironmental factors may prime cells toward invasive phenotypes, giving rise to cellular rearrangements and enhanced migration (*119*, *120*).

Cellular rearrangements cease when the cell shape index approaches a critical value (*25*). Based on the vertex model, which defines a shape index ($cell\ perimeter/\sqrt{projected\ cell\ area}$) of 3.81 as the jamming threshold (*35*), structural rearrangement requires cell shape changes. In this way, cells can overcome the jamming constraints of density by adapting their shapes. Densely packed cells can still move if they elongate (i.e., increase the shape index above 3.81), whereas the tissue becomes jammed as the shape index decreases and approaches the critical value. Thus, the jamming transition can be controlled by the preferred cell shape.

It is known that cell-cell and cell-substrate adhesion forces act together to generate a preferred cell shape (*18*, *31*, *121*). Adhesions are major sites of force transmission in cells and generally strengthen as cells approach jamming (*9*). Cell-cell adhesion is mediated by cadherins that are anchored to the cytoskeleton (*122*), whereas integrin-dependent cell-substrate adhesion is governed by focal adhesions that generate internal cytoskeletal tension (*123*). In nonconfluent tissues, decreasing cell-cell adhesion reduces cell crowding and cell-cell contacts, increasing the fluidity of the tissue (*11*). In confluent tissues, the role of cell-cell adhesion tends to be cell-type specific and depends on invasive potential (*124*). Strong cell-substrate adhesion combined with high

traction stresses are shown to contribute to unjamming in confluent systems (*52*, *125*). Relatively small changes in cell-cell and cell-substrate adhesion can have profound effects on tissue rheology and can be used to regulate cell arrest (*25*, *126*). How cell-cell and cell-substrate adhesion manipulate jamming transitions in a mechanically stressed monolayer remains unclear.

Here I characterize the role adhesion complexes play in regulating cell jamming—unjamming transitions in dense monolayers subjected to mechanical compression. As compressive stress is applied to normal breast epithelial cells (MCF10A) and metastatic breast cancer cells (4T1), MCF10A cells are rendered immobile while 4T1 cells become fluid-like and migrate as a highly coordinated collective. In the process, 4T1s become elongated and develop strong cell-cell adhesions, whereas E-cadherin is disrupted at the cell-cell contacts of MCF10As. Since mesenchymal markers are not upregulated in compressed 4T1s, this compression-induced transition is distinct from the epithelial-to-mesenchymal transition (EMT). Compression reduces traction stresses in micropatterned cell islands and within the bulk monolayer for both cell lines. Together, I show that upregulated intercellular adhesion and reduced traction within the bulk cell sheet regulate the observed differential cellular responses to mechanical compression and contribute to jamming—unjamming transitions.

2.3 Materials and Methods

2.3.1 Cell culture

The human non-tumorigenic breast epithelial cell line MCF10A was a gift from Sofia Merajver (University of Michigan) and was obtained from Dr. Heppner at the Michigan Cancer Foundation where the cell line was originally developed. The mouse breast cancer cell line 4T1 was a gift from Lance Munn (Harvard Medical School) and was originally obtained from ATCC. The

mouse breast cancer cell line 67NR was obtained from the Karmanos Cancer Institute (Detroit, MI). All cell lines were cultured in RPMI medium (Corning) supplemented with 10% FBS, except for MCF10A. MCF10A cells were cultured in DMEM/F12 medium (Corning) supplemented with 5% horse serum, 20 ng/ml epidermal growth factor (EGF), 0.5 μg/ml hydrocortisone, 100 ng/ml cholera toxin and 10 μg/ml insulin. Cells were cultured in a humidified atmosphere containing 5% CO_2 at 37°C.

2.3.2 Generation of E-cadherin knockdown 4T1 cells

4T1 cells expressing inducible shRNA knockdown of E-cadherin was generated using a transfer plasmid provided by Valerie Weaver at UCSF (*127*). The transfer vector consisted of a modified pLKO.1 neo plasmid (Addgene) with expression of the shRNA sequences under control of 3× copies of the lac operator and a copy of the mNeonGreen fluorescence protein. The E-cadherin shRNA had the following sequence: 5' - GAACGAGGCTAACGTCGTAAT - 3'; scramble shRNA (Sigma #SHC002) had the following sequence:

CCGGCAACAAGATGAAGAGCACCAACTCGAGTTGGTGCTCTTCATCTTGTTGTTTTT.

Lentiviruses were generated by transfecting HEK 293T cells with the transfer vector, psPAX2 packaging vector, and pMD2.G envelope vector. Viral supernatant was collected 48 h after transfection. 4T1 cells were transduced with E-cadherin shRNA or scramble non-targeting control shRNA in RPMI medium and after 24 h, shE-cadherin and scramble cells were selected with 200 μg/ml G-418 (Sigma) and 2 μg/mL puromycin, respectively. E-cadherin knockdown was induced in shE-cadherin cells by adding 200 μM isopropyl-β-D-thiogalactoside (IPTG; Sigma) 72 h prior to experiments.

2.3.3 Mechanical compression using an in vitro compression setup

Vertical compression was applied by adding a weight of 26 or 52 g over an area of 426 mm^2

to achieve stresses of 600 or 1,200 Pa, respectively, using a previously established setup (*124, 128*). The fixed weight applies a constant stress to a UV-treated 1% agarose gel cushion in contact with cells. The agarose gel allows nutrient and oxygen diffusion. The agarose gel was used without the weight as a negative control. Samples for live imaging, immunofluorescence staining, and RT-qPCR were compressed for the specified durations under cell culture conditions.

2.3.4 In vitro scratch-wound assay and time-lapse imaging

Cells were plated onto 6 well plates 72 h prior to experiments and grown to confluence. MCF10A and 4T1 cells were serum-starved in DMEM/F12 medium without horse serum and EGF and RPMI medium without FBS, respectively, for 4 h prior to experiments. Cells were then incubated with Hoechst 33342 diluted in PBS for 30 min at 37°C. Cells were washed with PBS and placed in complete medium. Scratches were created using a p-200 pipette tip to induce migration. After wounding, vertical compressive stresses of 0, 600 and 1,200 Pa were applied. Images of the wound area were captured using a 4× objective at 30 min time points for 16 h using fluorescence microscopy on a Cytation 5 automated plate reader. Collective cell migration was quantified by measuring the area between wound edges using MATLAB. Spatiotemporal velocity maps were generated using the software AveMap+ (*129*). Results were collected from three independent experiments.

2.3.5 Immunofluorescence staining

Cells on glass coverslips were washed with PBS and fixed with 4% paraformaldehyde for 10 minutes, washed with PBS, and permeabilized with 0.1% Triton X-100 in PBS for 10 minutes. Cells were washed with PBS and blocked with 3% BSA in PBS for 1 h. Cells were incubated with a rabbit anti-E-cadherin antibody at 1:400 (Cell Signaling) and a primary mouse anti-vinculin antibody at 1:800 (Sigma-Aldrich) in 3% BSA overnight at 4°C. Cells were washed 3× with PBS

and incubated with DAPI, phalloidin, and secondary antibodies in 3% BSA for 1 h at room temperature. Cells were washed 3× with PBS, mounted onto glass slides with Fluoromount-G (Invitrogen), and imaged by spinning disk confocal microscopy. Fluorescence levels relative to the control condition were quantified. E-cadherin at cell–cell contacts was quantified by measuring fluorescence intensity at the cell membrane.

2.3.6 Confocal microscopy

Images of immunostained cells were taken using an oil immersion Plan-Apochromat 60 x/1.4 NA objective on an inverted microscope (Olympus IX-81) equipped with an iXON3 EMCCD camera (Andor Technology), AOTF-controlled lasers (Andor Technology), and a Yokogawa CSU-X1 spinning disk confocal. Acquisition of images was controlled by MetaMorph (Molecular Devices). Single and z-stack images of cells fluorescently labeled for DAPI, F-actin (by 488-phalloidin), E-cadherin, and vinculin were captured with 405 nm, 488 nm, 561 nm, and 640 nm excitations, respectively, at exposure times of 200-500 ms.

2.3.7 Quantification of cell and nuclear shapes

Immunofluorescence images were acquired as described above. For each pressure condition, more than 200 cells and nuclei were manually traced using ImageJ software (National Institutes of Health) from ten different fields of view. The cell and nuclear shape indices were computed for each traced cell and nucleus, respectively.

2.3.8 Quantification of vinculin intensity

Cells were immunostained for E-cadherin using a rabbit anti-E-cadherin antibody (Cell Signaling) and vinculin using a primary mouse anti-vinculin antibody (Sigma-Aldrich), followed by fluorophore conjugated secondary antibodies. ImageJ was used to threshold the image and compute the fluorescence intensity of particles at the basal plane. E-cadherin staining was used to

define a mask at intercellular contacts, and vinculin fluorescence intensity was measured within the mask at the same plane as E-cadherin.

2.3.9 RNA extraction and RT-qPCR

RNA was extracted using the RNeasy micro kit (Qiagen). RNA quality and quantity were measured using a NanoDrop 1000 spectrophotometer. Reverse transcription was performed using the iScript cDNA synthesis kit (Bio-Rad). qPCR assays were conducted using SYBR Green (Bio-Rad) and specific primers quantifying *gapdh*, *cdh1*, *cdh2*, and *vim* (OriGene) on the Bio-Rad CFX thermocycler. *Gapdh* was used as a control for quantifying relative gene expression. Mean C_t values from duplicates were used to calculate ΔC_t values normalized to GAPDH. Relative transcript levels were determined by calculating the change between ΔC_t values of control and compressed samples as $\Delta\Delta C_t$ and calculating $2^{-\Delta\Delta Ct}$. Results were collected in duplicates from three independent experiments.

2.3.10 Fabrication of soft silicone substrates

CY52-276 A/B (Dow Corning) with an A:B ratio of 1:1 was cast in 35 mm glass bottom dishes. After 10 min of degassing, the silicone substrates were cured on a hot plate at 70°C for 30 min. The substrates were then exposed to deep UV light for 5 min. 19 mg EDC (1-Ethyl-3-(3-dimethylaminopropyl)-carbodiimide) (Thermo Fisher), 11 mg sulfo-NHS (N-Hydroxysulfosuccinimide) (Thermo Fisher), and 15 µl 2% w/v 0.5 µm carboxylate fluorescent beads (Thermo Fisher) were added to 1 ml DI water. The substrates were incubated with this suspension for 30 min to conjugate fluorescent beads to the surface of the soft silicone (*130, 131*).

2.3.11 Micropatterning of silicone substrates

Micropatterned substrates were made with standard soft lithography technique to create a silicon master mold. Polydimethylsiloxane (PDMS) was prepared by mixing Sylgard-184 elastomer

and curing agent (Dow Corning) in a 10:1 (w/w) ratio. After 10 min of degassing, the PDMS mixture was poured over the master and cured overnight at 60°C. PDMS stamps with 400 μm circular patterns were incubated with fibronectin (Corning) at a concentration of 40 μg/ml for 1 h. Soft silicone substrates were UV-treated for 5 min and then immediately placed in contact with the stamps (*132*). Printed substrates were passivated with anti-adherence rinsing solution (STEMCELL Technologies) for 1 h.

2.3.12 Traction force microscopy

A seeding density of 20,000 cells cm^{-2} formed confluent monolayers after 72 h. The same seeding density formed cell islands on micropatterned substrates after 48 h. Cells labeled by Hoechst 33342 and red fluorescence beads on the substrate surface were imaged before and after the removal of cells using 10% sodium dodecyl sulfate (SDS). PIVlab (*133*) was used to process image pairs (bead images before and after cell removal) and then used with the fast Fourier transform window deformation method to quantify the displacement of the beads, resulting in a displacement vector field. The Young's modulus of the substrate was previously measured to be 7.2 kPa using sphere indentation (*134*). Fourier transform traction cytometry was used to compute the traction stress field using MATLAB (*135–138*). To compute traction stresses at the leading edge during wound healing, regions parallel to the wound margin and within 5-7 cell layers were analyzed, and the rest of the cells were considered as bulk.

2.3.13 Statistical analysis

Statistical analysis was carried out in Origin and performed with one-way ANOVA followed by Tukey post-hoc multiple comparisons test. Analysis of wound healing assays was performed by comparing the percentage of wound closure at 16 h between different conditions. Results were collected from three independent experiments and data from individual cells, field of view, or cell

islands are plotted as mean ± S.E. or shown as boxplots, depending on the experiment. Statistical significance was denoted by asterisks in the figure panels, with $* = p < 0.05$, $** = p < 0.01$, $*** = p < 0.001$.

2.3.14 Theoretical model and simulation details

Cells in a 2D monolayer in the SPV model (*18*) are represented by polygons determined from a Voronoi tessellation of their center positions (r_i). The center of each cell obeys the over-damped equation of motion

$$\frac{d\boldsymbol{r_i}}{dt} = \mu \boldsymbol{F_i} + v_0 \hat{\boldsymbol{n}}_{\boldsymbol{i}} \qquad (1)$$

The first term on the right hand side (RHS) of Eq. (1) comes from cell-cell interactions and the mechanical behavior of a single cell. Here μ is the single cell mobility constant and the interaction force is given by $\boldsymbol{F}_i = -\boldsymbol{\nabla}_i E$, where E is the total mechanical energy of the tissue given by

$$E = \sum_{i=1}^{N} [K_A (A_i - A_0)^2 + K_P (P_i - P_0)^2] \qquad (2)$$

In this equation, A_i and P_i are area and perimeter of cell ith, A_0 and P_0 are the cell preferred area and perimeter, respectively. K_A and K_P are the area and perimeter moduli. The term involving cell area models cell's incompressibility and monolayer's resistance to height fluctuation. The quadratic term in perimeter results from active contractility of subcellular cortex. The linear term in perimeter is a combination of cortical tension and membrane tension due to cell-cell adhesion. The membrane line tension can be reduced by either increasing cell-cell adhesion, which encourages the cell to lengthen its shared edges with its neighbors, or by reducing actin-myosin contractility. Therefore, P_0 is positively correlated to cell-cell adhesion and negatively correlated to cell contractility (*121*). For simplicity, we assume that the contribution of cell-cell adhesion to line tension is greater than

the contribution of actin-myosin contractility, so P_0 is positive as a consequence. N is the total number of cells in the monolayer. To nondimensionalize cell shape quantities, we adapt a target shape index parameter $p_0 = P_0/\sqrt{A_0}$.

In addition to the interaction force, cells are driven by a self-propelled force due to their own polarized motility. In the SPV model, this is captured by the second term on the RHS of Eq. (1), where v_0/μ is the self-propulsive force magnitude. For each cell, this force acts along a polarization vector, given by

$$\hat{\boldsymbol{n}}_{\boldsymbol{i}} = (cos\,\theta_i\,, sin\,\theta_i) \qquad (3)$$

that determines the direction of the self-propelled force. The polarity of cells is stochastic and obeys rotational Brownian dynamics, given by

$$d\theta_i/dt = \eta_i(t) \qquad (4)$$

where $\eta_i(t)$ is a white noise process with zero mean and variance $2D_r$, given by

$$\langle \eta_i(t)\eta_j(t')\rangle = 2D_r\delta(t-t')\delta_{ij} \qquad (5)$$

The magnitude of the rotational noise D_r defines a time scale $\tau = 1/D_r$ of persistent motion.

We employ an open source implementation of the SPV model to perform CellGPU (*139*) simulations of 900 cells for 5 million time steps with dt = 0.05 at each parameter of p_0, v_0. We choose $D_r = 1, K_A = 1, K_P = 1, A_0 = 1$.

In the SPV model, the traction force or the total force exerted by the cell onto the substrate is given by a sum of the viscous friction between the cell and the substrate and the self-propulsive force

$$\vec{f}_{traction} = -\boldsymbol{v_i}/\mu + v_0\hat{\boldsymbol{n}}_{\boldsymbol{i}}/\mu \qquad (6)$$

Since the net force on each cell is balanced according to Equation (1), the traction $\vec{f}_{traction}$ is always

equivalent to the interaction force. Therefore, we use the interaction force to determine the magnitude of the traction of every cell in the system.

2.4 Results

2.4.1 Long-term compressive stress drives cell jamming—unjamming transitions

I first asked whether the effects of long-term mechanical compression on collective cell migration depended on invasive potential. Solid compressive stress ranges from 0.1-10 kPa have been reported in human tumors 0.25-8 kPa in murine tumors (*80*). To address this, I conducted wound healing assays of non-tumorigenic (MCF10A) and cancer (4T1) breast epithelial cells subjected to different levels of compressive stress. The 4T1 cell line is a widely used breast cancer model with the capacity to metastasize efficiently to sites affected in human breast cancer and is therefore particularly useful for stage IV human breast cancer research (*140–142*). Confluent MCF10A and 4T1 monolayers were scratched to create a uniform wound, inducing migration, and normal compressive force was applied to the cells while the wound margin was monitored over 16 hours (**Figure 2.1A**). This in vitro model has been used previously by us and others and mimics the solid compressive stress experienced by cells during tumor development (*124*, *128*).

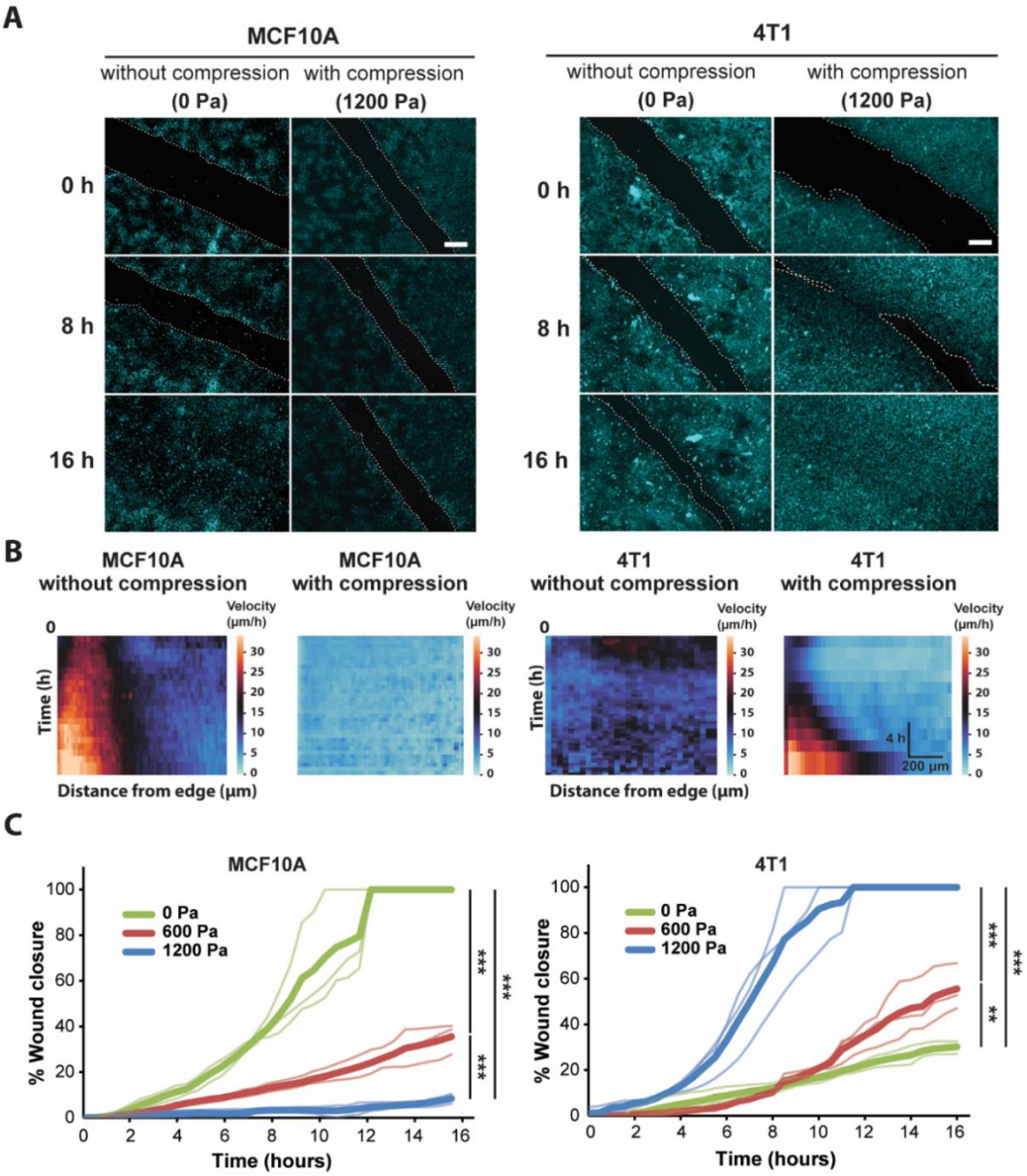

Figure 2.1. Compressive stress inhibits migration in MCF10A cells and enhances migration in 4T1 cells.

(A) Representative fluorescence images of MCF10A and 4T1 wound areas at the indicated time points post-wound with and without compression. Cell nuclei are labeled with Hoechst 33342. Lines are scratched on each well using a p-200 pipette tip and cell migration is captured by fluorescence microscopy at 30 min time intervals for 16 h post-wound. Cell edges used to calculate wound area are outlined by white dashed lines. Scale bars, 200 μm. **(B)** Heat maps show spatiotemporal evolution of the velocity for control and compressed cells. **(C)** Quantification of wound area (between white dashed cell edges) for each cell type and compressive pressure. Mean wound area at

each time point is plotted from three independent replicates with the individual experiments plotted as thin lines.

During wound healing, control MCF10A cells migrated together at a constant velocity to close the wound. The epithelial sheet was in a seemingly motile but locally jammed state as the cells migrated collectively in a coordinated manner, however only cells near the wound edge exhibited high cell velocity, suggesting that the cells in the bulk of the monolayer were caged by their neighbors (**Figure 2.1B**). Control 4T1 cells displayed low cell velocity, leading to minimal collective migration and failure to close the wound. Applying compressive stress to MCF10A cells resulted in exceptionally low migratory activity, and the cells became nearly immobile (**Figure 2.1B**). However, compressed 4T1 cells underwent highly collective, fluid-like migration and abruptly closed the wound (**Figure 2.1A**). By applying different levels of mechanical compression and tracking the wound margin over time, I demonstrated that compressive stress attenuated cell motility in MCF10A cells, which quickly entered a jammed state. On the other hand, 4T1 cells reacted actively to compressive stress by transitioning to a fluid-like state (**Figure 2.1C**), and the wound closure rate was positively correlated with the level of external stress applied. The percentage of wound closure after 16 hours was not correlated with the initial wound width for all compressive stresses tested (**Figure 2.2**).

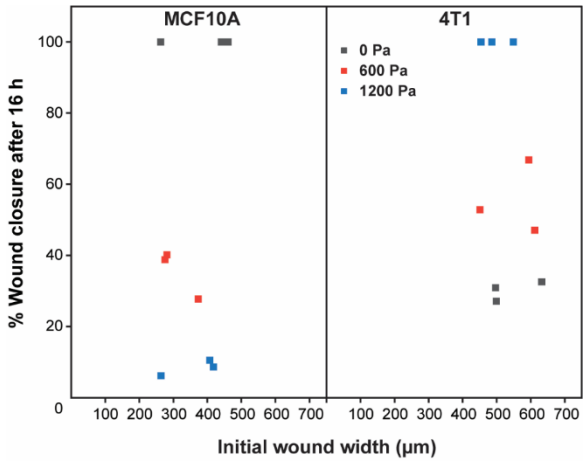

Figure 2.2. Wound healing does not depend on wound width.

Percentage of wound closure after 16 h does not depend on initial wound width in wound healing assays for MCF10A and 4T1 cells under different compressive stresses.

2.4.2 Unjamming is linked to changes in cell shape and nuclear shape

I next investigated cell shape as a marker for cellular fluidity in mechanically stressed monolayers. Previously published work used the vertex model to define a critical shape index of 3.81 as the jamming threshold (*18*). Studies using human bronchial epithelial cells show that regardless of the magnitude of intracellular stress fluctuations, cellular rearrangements cease when the shape index approaches the jamming threshold (*35*). Applying compressive stress to MCF10A cells lowered the shape index, which approached the critical value of 3.81 (**Figure 2.3, A and B, Figure 2.4**), leading to more compact cells. In contrast, the cell and nuclear shapes of compressed 4T1 cells became elongated (higher shape index) and more variable compared to control cells (**Figure 2.3B**). Although the shape index depends on elongation and tortuosity, the cell aspect ratio (AR) emphasizes elongation and deemphasizes tortuosity (*49*). In 4T1 cells, substantial increases in AR were accompanied by smaller increases in shape index (**Figure 2.5A**), resulting in elongated cells with straight edges. Therefore, cell elongation can be better captured by plotting the mean of

AR vs. the standard deviation (s.d.) of AR. I found this to have a positive linear relationship (**Figure 2.3C**), in agreement with what has been shown previously (*17*). As the cell AR increased with compressive stress, indicative of unjamming, its variability from cell to cell increased. Compressed cells tended to have higher values of $\overline{AR}$ and s.d. of AR. Increased cell elongation and shape variability suggest more disordered cell packing and fluid-like behavior and may be an indicator for increased metastatic potential. These results, together with the earlier wound healing observations, demonstrate a correlation between cell shape and jamming—unjamming transitions.

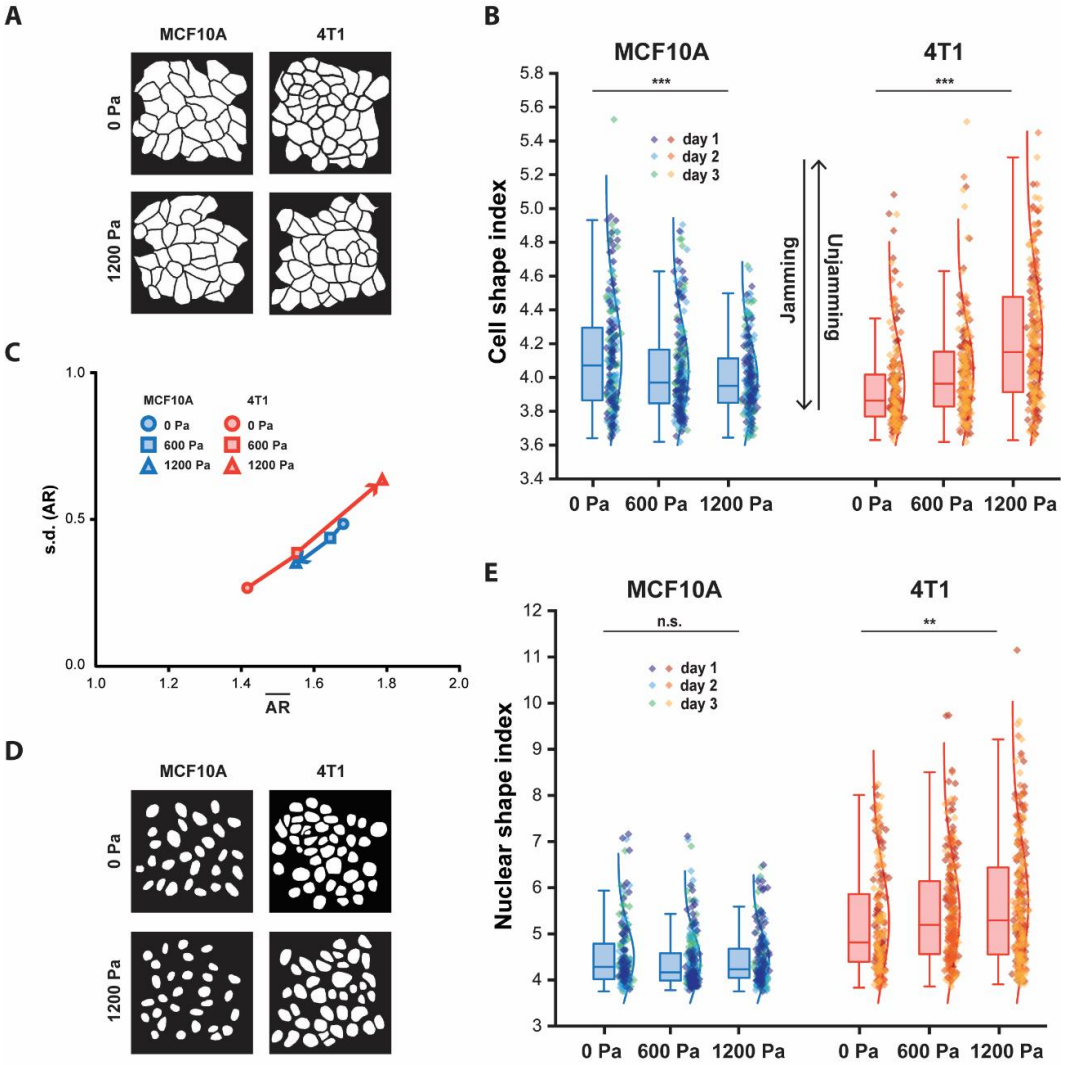

Figure 2.3. With compression, MCF10A cells and nuclei become more compact, whereas 4T1 cells and nuclei elongate.

(A) Representative binary images outlining fixed MCF10A and 4T1 cells labeled with E-cadherin with and without compression. **(B)** Boxplot of cell shape index for MCF10A and 4T1 cells subjected to 0, 600 or 1,200 Pa for 12 h. **(C)** Cell aspect ratio (AR), which emphasizes elongation, of control and compressed MCF10A and 4T1 cells is plotted as mean of AR ($\overline{AR}$) vs. standard deviation (s.d.) of AR for each cell type and compressive pressure. **(D)** Representative binary images outlining fixed MCF10A and 4T1 cell nuclei (labeled with DAPI) with and without compression. **(E)** Boxplot of nuclear shape index for control and compressed MCF10A and 4T1 cells. Boxplots of cell and nuclear shape indices show median and quartiles for three independent replicates. Whiskers are maximum and minimum data points, and data from each replicate is denoted as a different color. Number of MCF10A cells and nuclei analyzed: 0 Pa (n = 234), 600 Pa (n = 229), 1200 Pa (n = 222). Number of 4T1 cells

and nuclei analyzed: 0 Pa (n = 205), 600 Pa (n = 231), 1200 Pa (n = 224).

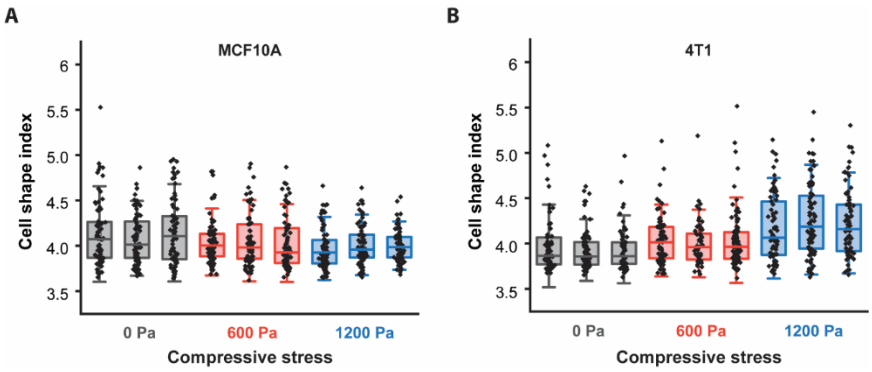

Figure 2.4. Analysis of cell shape index in response to different compressive stresses.

Cell shape index measurements of MCF10A **(A)** and 4T1 **(B)** under different compressive stresses are similar for independent experiments. Each boxplot shown displays mean ± S.D. for data from a single day of experiment.

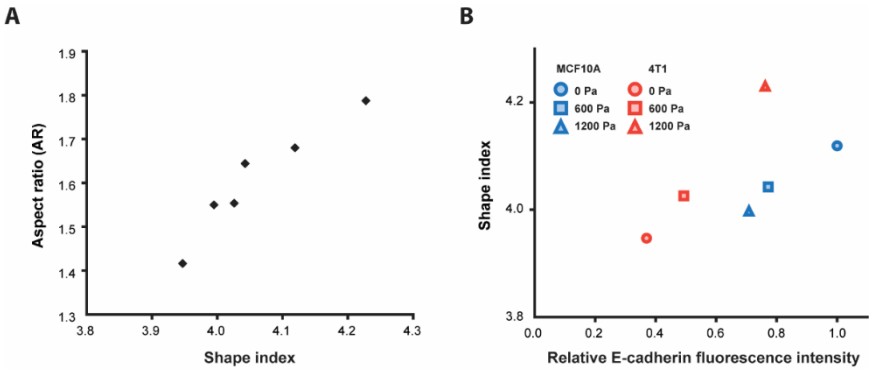

Figure 2.5. Correlations between shape index and aspect ratio or E-cadherin expression.

(A) Plot shows shape index, which emphasizes perimeter, vs. aspect ratio (AR), which emphasizes elongation. Substantial increases in AR are accompanied by smaller increases in shape index. **(B)** Plot shows E-cadherin fluorescence level vs. cell shape index for MCF10A and 4T1 under specified compressive stresses. As the relative E-cadherin fluorescence intensity at cell-cell contacts is elevated, the shape index increases as well.

Along with cell shape, nuclear shape has recently been linked to tissue fluidity (*117*) and is a critical marker for tumor aggressiveness in clinical cancer grading (*143*). Cancer cell nuclei are generally larger and softer than non-malignant cell nuclei (*44*, *144*, *145*), and studies of multiple cancer cell types, including breast cancer cells, have found that the cells and their nuclei become significantly softer upon extravasation (*146*). Since nucleus deformability is known to play a central role in cell motility in dense environments (*147*), I next asked whether changes in nuclear shape were correlated with changes in cell shape in cells subjected to mechanical compression. As 4T1 cells elongated with compression, a higher cell shape index corresponded to an increased nuclear shape index and high variance in nuclear shape (**Figure 2.3, D and E**), which has been associated with more aggressive tumors (*117*). Our results show that cell and nuclear shape indices increase with compressive stress in unjamming transitions and are important indicators of cell motility and tissue fluidity. More importantly, mechanical compression resulted in elongated cell and nuclear shapes in metastatic 4T1 cells, which became unjammed, but not in non-tumorigenic, jammed MCF10A cells.

2.4.3 The compression-induced unjamming transition is distinct from EMT

To further elucidate how compressive stress impacts cell-cell organization, I next investigated the factors which shape cells and support migration in a mechanically stressed monolayer. I first examined the intensity of E-cadherin at adherens junctions after long-term compression. Immunofluorescence staining revealed that compressive stress disrupted E-cadherin localization at the intercellular contacts of MCF10A cells (**Figure 2.6, A and B**). Surprisingly, compressed 4T1 cells gained strong cell-cell contacts evidenced by the increased recruitment of E-cadherin to cell junctions (**Figure 2.6, C and D**), which was also strongly evident in micropatterned 4T1 cell islands (**Figure 2.6, E and F**). To form micropatterned cell islands, microcontact printing

was used to generate fibronectin-coated, circular adhesive islands with a diameter of 400 μm. Compressed 4T1 cell islands showed higher E-cadherin expression and localization to the cell-cell membrane. In a wound healing assay, the lack of collective migration exhibited by 4T1 cells in the absence of applied stress can be attributed to weak cell-cell adhesion. As compressive stress strengthened intercellular adhesion, strong adhesion forces maintained high cell density and encouraged highly directed and coordinated migration, leading to fluidization of the cell layer. Furthermore, compression-induced changes in E-cadherin expression were correlated with cell shape index, with elongated cells having increased localization of E-cadherin to intercellular contacts (**Figure 2.5B**). This result supports that adhesion strength is higher in a more unjammed cell layer.

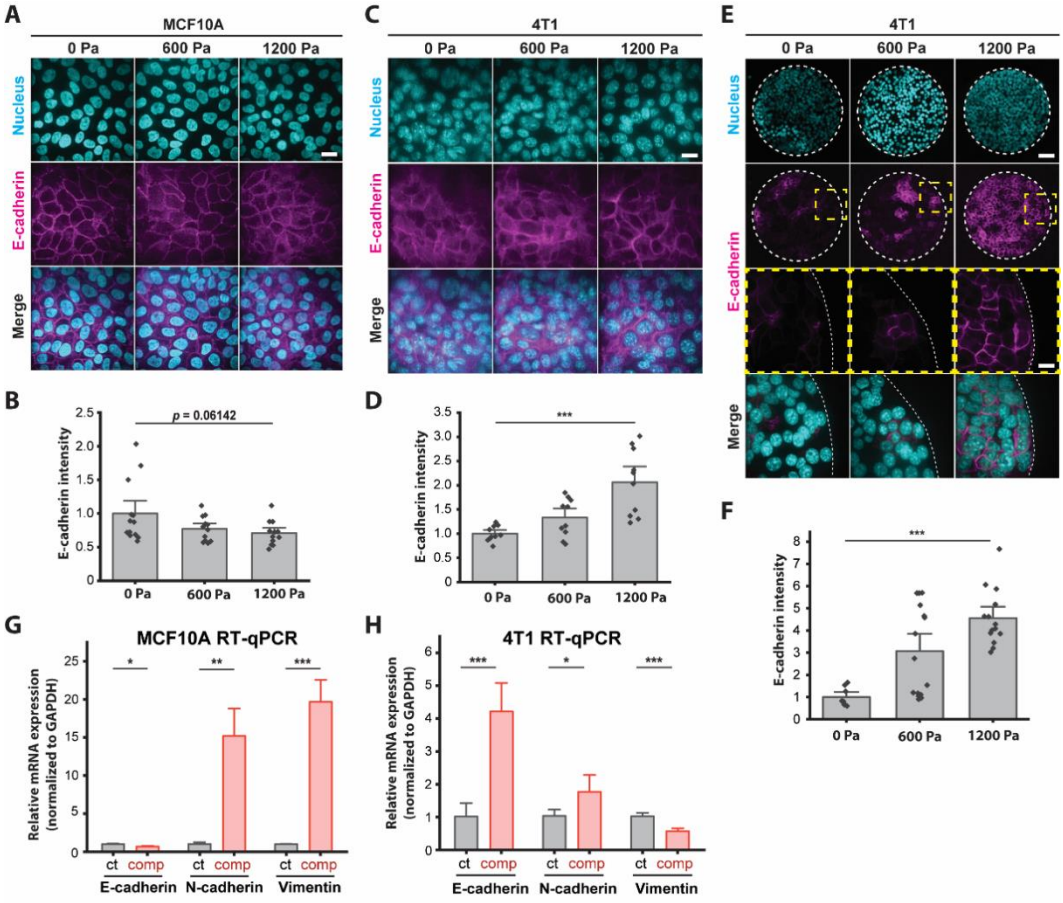

Figure 2.6. E-cadherin is upregulated in unjammed 4T1 cells under mechanical compression.

(A) Representative immunofluorescence images of MCF10A cells labeled with DAPI and an E-cadherin antibody. Cell monolayers are subjected to specified compressive pressures for 12 h. Scale bar, 20 μm. **(B)** Quantification of relative E-cadherin fluorescence at MCF10A cell-cell contacts. Mean fluorescence intensity at the cell membrane ± S.E. is plotted from three independent replicates (n = 12-13). **(C)** Representative microscopy images of 4T1 cells labeled with DAPI and an E-cadherin antibody in the same experimental conditions as in (A). Scale bar, 20 μm. **(D)** Quantification of relative E-cadherin fluorescence at 4T1 cell-cell contacts. Mean fluorescence intensity at the cell membrane ± S.E. is plotted from three independent experiments (n = 10). **(E)** Representative microscopy images of microcontact printed 4T1 cell islands labeled with DAPI and an E-cadherin antibody. Micropatterned cell islands are exposed to specified stresses for 12 h. Scale bars, 80 μm (top) and 20 μm (bottom). **(F)** Quantification of relative E-cadherin fluorescence at the cell-cell contacts of 4T1 cell islands. Mean fluorescence intensity at the cell membrane ± S.E. is plotted from three independent replicates (n = 8-15). qPCR analysis of E-cadherin, N-cadherin, and vimentin mRNA levels with and without compression (1,200 Pa) for

MCF10A **(G)** and 4T1 **(H)** cell monolayers. Transcript levels are calculated using the $\Delta\Delta C_t$ method normalized to GAPDH. Mean mRNA level ± S.E. is plotted from three independent experiments with duplicates per experiment.

To identify a possible mesenchymal molecular signature in compressed cells that attributes increased migratory capability to EMT (*18, 49*), I conducted qPCR assays to quantify mRNA levels of epithelial marker E-cadherin and mesenchymal markers N-cadherin and vimentin. Compressive stress significantly downregulated E-cadherin and upregulated vimentin in MCF10A cells (**Figure 2.6G**). Surprisingly, E-cadherin was upregulated in compressed 4T1 cells by ~4-fold, while vimentin was downregulated **(Figure 2.6H)** – these are features associated with mesenchymal—epithelial transition (MET), as opposed to EMT. N-cadherin was upregulated by compression in both cell types, although upregulation was higher in MCF10A cells. Altogether, I find that enhanced collective migration and a higher cell shape index are associated with increased levels of cell-cell adhesion **(Figures 2.3 and 2.6)**. The upregulation of E-cadherin and downregulation of vimentin in unjammed 4T1 cells suggest that the factors governing unjamming transitions in this system is distinct from the transitions between epithelial and mesenchymal cells.

2.4.4 Cadherin-mediated cell-cell adhesion is required for unjamming

To probe the role of E-cadherin further, I attenuated cell-cell adhesions by knocking down E-cadherin (encoded by CDH1 gene) in 4T1 cells and tested the effect of knockdown on compression-induced unjamming compared to cells transduced with scramble shRNA (**Figure 2.7, A and B**). Upregulated E-cadherin in unjammed cells suggests a role for cell-cell adhesion in dense monolayers under mechanical compression, and knockdown of E-cadherin is known to switch the migration mode of cells from collective to single-cell migration (*148*). Knocking down E-cadherin initially increased cell motility, consistent with recently published work (*50*); however collective

movement was substantially inhibited in E-cadherin knockdown (E-cad KD) cells upon compression (**Figure 2.8**). Upregulation of E-cadherin expression by compression was significantly reduced in E-cad KD cells relative to scramble cells (**Figure 2.7C**). This upregulation was not due to recovery of E-cadherin expression as E-cadherin remained downregulated over the course of 18 hours when uncompressed (**Figure 2.9**). Additionally, the mesenchymal markers N-cadherin and vimentin were upregulated in KD cells and further upregulated by compression (**Figure 2.7, D and E**). Applied compressive stresses of 600 and 1,200 Pa decreased the collective migration of E-cad KD cells (**Figure 2.7, F and G**), lowering the rate of wound closure from ~31% for 0 Pa to ~9% for 1,200 Pa (**Figure 2.7H**). Our results indicate that E-cad KD cells existed in a jammed state when compressed, similar to what I observed in MCF10A cells.

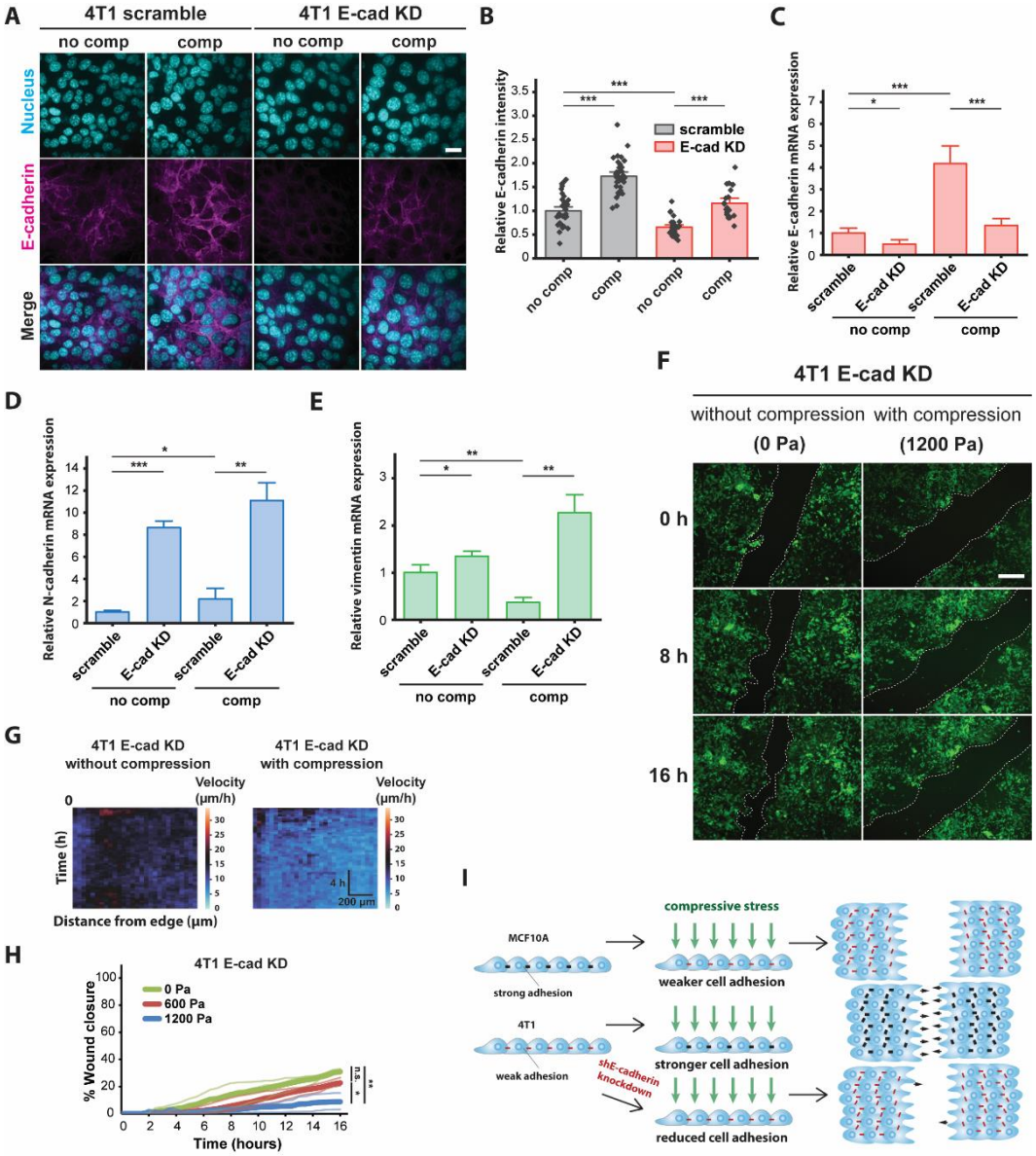

Figure 2.7. E-cadherin knockdown inhibited compression-induced upregulation of E-cadherin in 4T1 cells, triggering jamming.

(A) Representative microscopy images of 4T1 scramble and E-cad KD cells labeled with DAPI and an E-cadherin antibody. E-cad KD is induced in 4T1 shE-cadherin cells by adding 200 μM IPTG 72 h prior to experiments. Cell monolayers are exposed to specified stresses for 12 h. Scale bar, 20 μm. **(B)** Quantification of relative E-cadherin fluorescence at the cell-cell contacts of 4T1 scramble and E-cad KD cells. Mean fluorescence intensity at the cell membrane ± S.E. is plotted from three independent replicates (n = 22-36). qPCR analysis of E-cadherin **(C)**, N-cadherin **(D)**, and vimentin **(E)** mRNA levels in 4T1 scramble and E-cad KD cells. Transcript levels are calculated using the $\Delta\Delta C_t$ method normalized to GAPDH. Mean mRNA level ± S.E. is plotted

from three independent experiments with duplicates per experiment. **(F)** Representative images of 4T1 E-cad KD wound area at the indicated time points post-wound. 4T1 shE-cadherin cells express mNeonGreen. Cell edges used to calculate wound area are outlined by white dashed lines. Scale bar, 200 μm. **(G)** Heat maps of spatiotemporal evolution of the velocity for 4T1 E-cad KD cells under different levels of mechanical compression. **(H)** Quantification of wound area (between white dashed cell edges) for each condition. Mean wound area at each time point is plotted from three independent replicates as a representative trace. **(I)** Summary depicting the effect of compressive stress on collective migration in MCF10A WT, 4T1 WT, and 4T1 E-cad KD cells. Strong cell-cell contacts are denoted by black dashes. Red dashes indicate weak cell-cell adhesion. Number of small black arrows (right) represent relative cell velocity during wound healing.

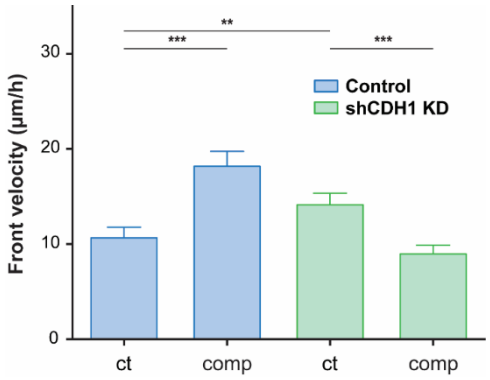

Figure 2.8. Front velocities for migrating WT and shCDH1 KD cell sheets.

Front velocities were computed for migrating 4T1 cell sheets by averaging the velocity measurements within 228 μm from the leading edge over 16 h. Cell velocity increases when shCDH1 is KD (compared to control cells) and decreases upon compression (1200 Pa) in KD cells. Data represent n = 9 wound edges for each condition. Mean velocity ± S.E. is plotted from 3 independent experiments.

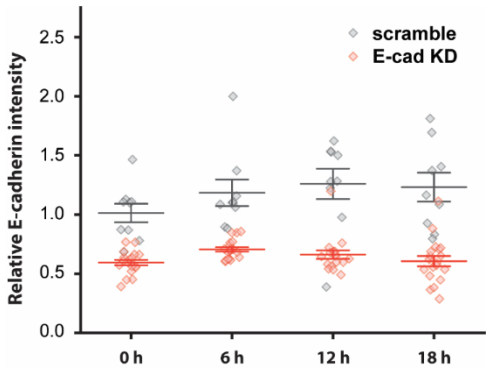

Figure 2.9. E-cadherin KD is consistent and maintained throughout the experiment duration.

E-cad KD is stable over 18 hours as measured by immunofluorescence of E-cadherin at the cell membrane starting from 72 h following treatment with IPTG. Markers represent mean values ± S.E. of data from three independent experiments. Both scramble and E-cad KD data are normalized to the scramble condition at 0 h.

To assess the generality of our finding, I explored the effect of mechanical compression on the nonmetastatic mouse breast cancer cell line 67NR, which is derived from the same primary breast cancer as 4T1 and expresses N-cadherin and vimentin, but not E-cadherin (*149*). Although 67NR cells have been shown to exhibit increased cell motility attributed to higher cell-substrate adhesion under compression (*124*), I did not observe unjamming behavior in compressed 67NR cells (**Figure 2.10A**), suggesting that expression and localization of E-cadherin is required for compression-induced, fluid-like unjamming transitions. Consistent with our findings for MCF10A, compressive stress did not increase E-cadherin levels in 67NR cells (**Figure 2.10B**). Based on our findings, schematically summarized in **Figure 2.7I,** that compressive stress significantly inhibited the coordinated migration of 4T1 E-cadherin KD cells, and that upregulation of E-cadherin is required for compression-induced unjamming, I conclude that E-cadherin-dependent cell-cell adhesion is a key regulator and effector upon compression.

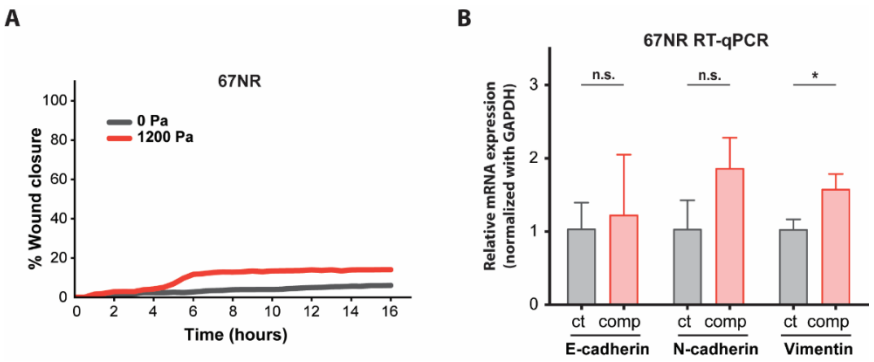

Figure 2.10. Compressive stress did not accelerate migration or increase E-cadherin levels in 67NR cells.

(A) Quantification of wound area for 67NR cells with and without compression. Mean wound area at each time point is plotted from 3 independent replicates as a representative trace. **(B)** qPCR analysis of E-cadherin, N-cadherin, and vimentin mRNA levels with and without compression (1,200 Pa). Transcript levels are calculated using the $\Delta\Delta C_t$ method normalized to GAPDH. Mean mRNA level ± S.E. is plotted from 3 independent experiments with duplicates per experiment.

2.4.5 Compressive stress reduces traction forces within the bulk cell sheet

I have shown thus far that increased cell-cell adhesion promotes the unjamming of mechanically compressed 4T1 cancer cells. Since high traction stresses have been shown to reverse the effect of density on shape-dependent cellular rearrangements (*52*) and to contribute to unjamming in a confluent monolayer (*125*), I next explored the role of substrate traction as a potential parameter working together with cell-cell adhesion to promote unjamming in tissues. Vinculin is a cytoskeletal protein responsible for regulating integrin-mediated cell adhesion and is found in focal adhesions as well as adherens junctions (*123*). In micropatterned 4T1 cell islands, compressive stress reduced vinculin intensity at the basal plane and enhanced the enrichment of vinculin at adherens junctions (**Figure 2.11, A and B**). A decrease in vinculin intensity at the basal plane is indicative of lowered cell-matrix adhesion, while increased vinculin at the cell-cell membrane is consistent with the increased localization of E-cadherin (**Figure 2.6, E and F**). Vinculin can strengthen the connection between the cadherin-catenin complex and the actin cytoskeleton by binding to alpha-catenin, which, in turn, associates with beta-catenin, facilitating its interaction with the cytoplasmic tail of E-cadherin and thereby enhancing the stability of cell-cell adhesions. I turned to traction force microscopy (TFM) to further disentangle the individual contributions of cell-cell adhesion and substrate traction (*11*).

In line with recently published work which showed that the perturbation of intercellular adhesion (by inactivation of the E-cadherin gene) increased traction forces (*150*), I used microcontact printing to generate circular adhesive islands with a diameter of 400 μm on a soft silicone substrate coated with fluorescent beads. 4T1 cell islands with low cell-cell adhesion exerted high traction and, consistent with this, MCF10A cell islands that expressed high intercellular adhesion had low traction stresses (**Figure 2.11C**). Applying compressive stress to micropatterned cell islands for 3 hours reduced traction for both cell types. Compressing MCF10A cell islands by 1,200 Pa reduced average traction stresses by 33.6% and strain energy by 52.1% (**Figure 2.11, D and E**). Compressive stress also largely obliterated traction forces in 4T1 cell islands; average traction forces and total strain energy decreased by 83.5% and 87.1%, respectively, compared to control cell islands (**Figure 2.11, D and E**). Together with earlier data from **Figure 2.6, E and F**, compression significantly elevated cell-cell adhesion in 4T1 cell islands while reducing cell-substrate stresses. Since microcontact-printed cell islands lack the leading edges of coordinated migration, these results suggest that the traction forces of cells within the bulk monolayer are reduced by compressive stress regardless of collective cell motility or the cell type I looked at.

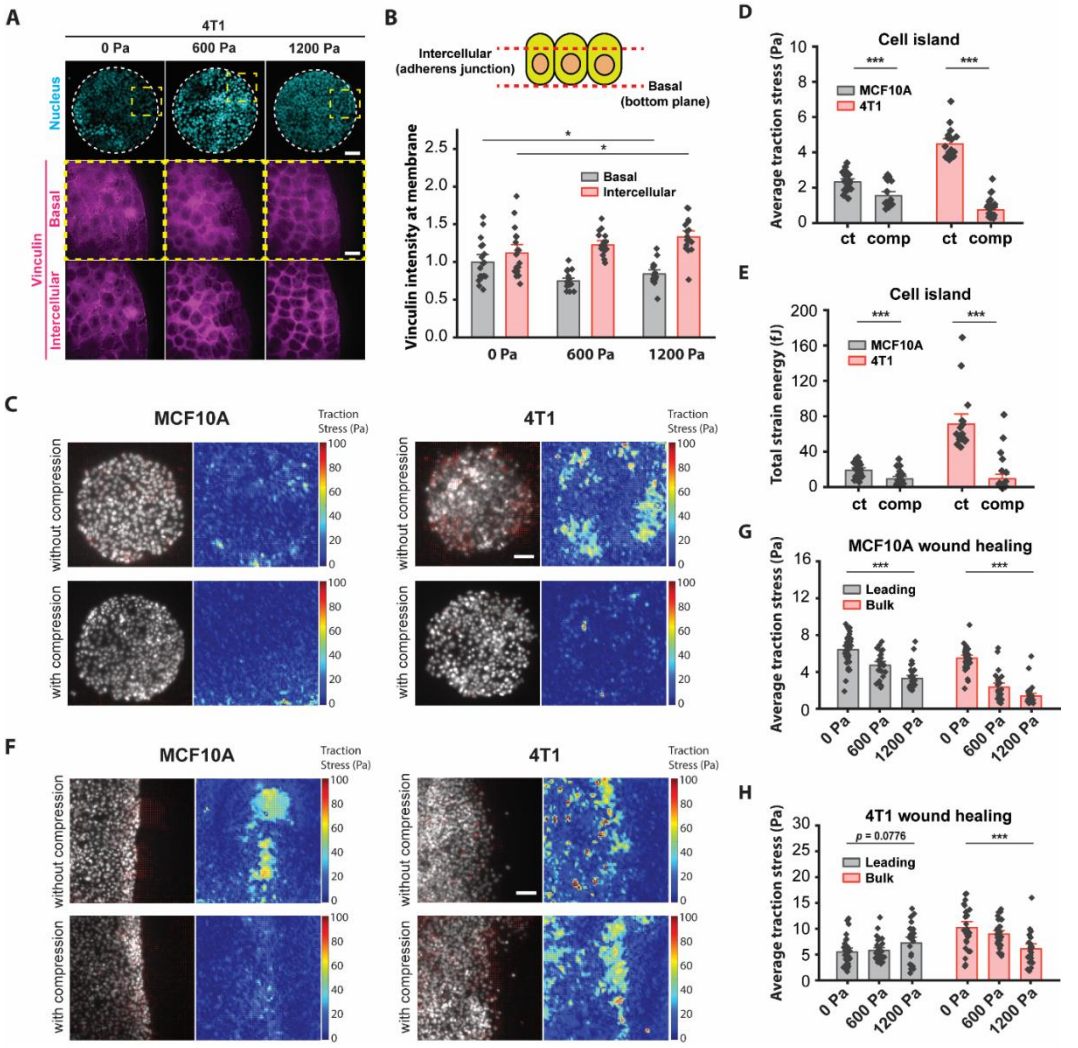

Figure 2.11. Compressive stress reduced traction stresses within the bulk cell sheet.

(A) Representative microscopy images of 4T1 cell islands labeled with DAPI and a vinculin antibody. Vinculin staining is shown at two different imaging planes. Micropatterned cell islands were exposed to specified pressures for 12 h. Scale bars, 80 μm (top) and 20 μm (bottom). **(B)** Quantification of relative vinculin intensity of individual cells at the basal plane and at intercellular junctions. Mean fluorescence ± S.E. is plotted from three independent replicates (n = 18). **(C)** Traction stress vector field and traction stress magnitude of micropatterned cell islands with and without 1,200 Pa compression for 3 h. Cell nuclei are labeled with Hoechst 33342. Scale bar, 80 μm. Mean traction stresses **(D)** and total strain energy **(E)** with and without compression on micropatterned islands. Number of images analyzed for MCF10A: control (n = 21), compressed (n = 21). Number of images analyzed for 4T1: control (n = 18), compressed (n = 30). **(F)** Traction stress vector field and traction stress magnitude of a wounded edge with and without 1,200 Pa compression for 3 h. Cell

nuclei are labeled with Hoechst 33342. Scale bar, 80 μm. Mean traction stresses exerted by MCF10A cells **(G)** and 4T1 cells **(H)** at the leading edge (within 5-7 cell layers of the wound margin) and within the bulk monolayer for 0, 600, and 1,200 Pa compressive stress for 3 h. Number of images analyzed for MCF10A: 0 Pa (n = 37), 600 Pa (n = 26), 1,200 Pa (n = 32). Number of images analyzed for 4T1: 0 Pa (n = 28), 600 Pa (n = 33), 1,200 Pa (n = 24).

Our observations using micropatterned cell islands indicated that cell-substrate stresses may not be the principal determinant of compression-driven unjamming in breast cancer cell migration. However, considering that traction forces were measured on microcontact printed cell islands, which do not permit coordinated migration, I cannot completely rule out the contribution of cell-substrate contraction. Previous studies of collective migration during wound healing suggest that the leading edge of a cell sheet presents more cell-substrate adhesion than follower cells (*124*), which enables coordinated migration. I grew monolayers of MCF10A and 4T1 cells on silicone substrate containing fluorescent beads. I initiated a wound healing assay and then applied mechanical compression to the cells for 3 hours. Subsequentially, I observed that traction forces were localized to the leading edge (within 5-7 cell layers of the wound margin) of MCF10A cell sheets and were attenuated by compressive stress (**Figure 2.11F**). Average traction stresses at the leading edge of compressed MCF10A cell sheets were reduced by 26.5% (600 Pa) and 48.9% (1,200 Pa) (**Figure 2.11H**). Control 4T1 cells generally exerted higher traction throughout the cell layer compared to MCF10A cells. Compression of 4T1 cell sheets by 1,200 Pa diminished average traction by 40.3% within the bulk monolayer while changes in traction at the leading edge was not statistically significant although traction stress appeared to increase at the leading edge (**Figure 2.11, F and H**). As traction stresses within the bulk monolayer decreased significantly with compressive stress, cells at the leading edge maintained high traction under compression (**Figure 2.11H**). Given these results, our observations point to a differential leader-follower traction force

response to compressive stress (i.e., reduced traction within the bulk monolayer and sustained traction at the leading edge) as a contributing factor in the unjamming behavior of 4T1 cells. Altogether, mechanical compression strengthens intercellular adhesion and attenuates traction forces exerted by cells within the bulk monolayer, leading to fluidization of the cell sheet.

2.4.6 Mapping condition of cells in vitro to theoretical simulation

To connect the experimental results to our theoretical model, we use (1) the observed cell aspect ratio (AR) values and (2) the cell traction forces to map the conditions of 4T1 and MCF10A cells to theoretical simulation parameters.

We performed simulations of the self-propelled Voronoi (SPV) model for a large range of v_0- p_0 values. For each simulation step, we compute the cell AR of each cell using the open-source function. The mean aspect ratio for each simulation was then calculated by averaging the AR over every cell over simulation time steps. A contour map of mean AR in the v_0-p_0 space is shown in **Figure 2.12**. On the other hand, the experimental values of mean AR for each condition are labeled in the v_0-p_0 space and the locus of (v_0, p_0) pairs having these values of AR form contours. However, this alone does not give a definitive value of (v_0, p_0). The jamming phase boundary demarcates solid-like states from fluid-like states, which is determined from the collective diffusive property at the tissue level. We next map the experimental values of cell tractions to the theoretical ones.

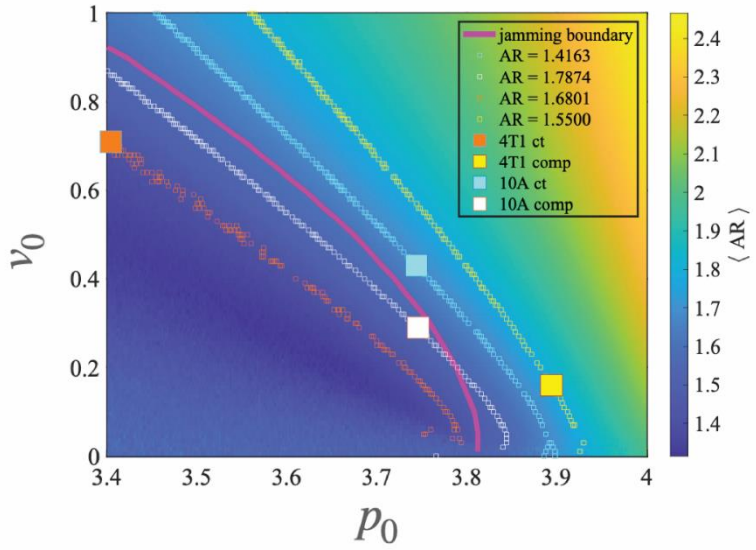

Figure 2.12. Contour plot of mean AR at different v_0 and p_0 is represented as a color plot.

Contour plot of mean AR at different v_0 and p_0 is represented as a color plot. The empty squares represent contour lines with the particular value of AR observed in experiments. The filled squares represent different cell lines and experimental conditions mapped by extrapolating from cell traction.

The average traction magnitude of the simulation systems that are on these contours is computed. We denoted the average traction magnitude to be T. To connect experimental traction values to simulations, we choose the traction values of 4T1 cells in the compressed case to map to the simulation traction value at ($p_0 = 3.404,\ v_0 = 0.71$). As a result, T(4T1 control) = 4.4790 was mapped to simulation traction of T($p_0 = 3.404,\ v_0 = 0.71$) = 0.626. This is an assumption in the analysis. However, the particular choice of this mapping does not influence the final qualitative conclusion in our work. The simulation traction magnitude of the system at this position is divided by the experimentally measured 4T1 traction to obtain the conversion factor. The traction values of other cell types and conditions are converted to simulation units by multiplying them by the factor of conversion. The positions of other cell conditions on the phase diagram are then determined by

matching both the AR and traction values between the experiment and simulation.

2.4.7 Theoretical simulation using the SPV model suggests distinct paths of jamming—unjamming

Our observed experimental data shows that there are two distinct responses to long-term compression from the two cell types of interest. The initially jammed 4T1 cells become unjammed under compression, whereas the MCF10A cells behave the opposite way, in a cell-adhesion dependent manner. Seeking a theoretical explanation for this distinction, we investigated the SPV model and mapped the observed cell's condition to a phase diagram of two model parameters (1) cell motility v_0 and (2) target cell shape index p_0 (the model and parameters are elaborated in more detail in the **Method** section). The SPV model is well-adapted to capture cell morphological metrics, which are crucial for studying cellular collectives. In the SPV model, the effect of cell-cell adhesion is captured by the parameter target shape index p_0 (*33*). In this theoretical model, the effects of increased cell-cell adhesion lead to a higher value of p_0. From the experimental results measuring E-cadherin fluorescence of MCF10A cells (**Figure 2.6B**), which shows an insignificant difference in relative E-cadherin intensity between control MCF10A and compressed MCF10A cells, we expect to see in the phase diagram that the difference in p_0 of controlled and compressed MCF10A cells is small. This expectation is observed in **Figure 2.13**, where p_0 of the mapped control MCF10A cells is 3.744, while of the mapped MCF10A compressed cells is 3.746. On the contrary, **Figure 2.6D** shows a significant difference in relative E-cadherin fluorescence between control and compressed 4T1 cells. 4T1 cells under long-term compression express much more E-cadherin, which suggests a drastic increase in p_0 for 4T1 cells under the effect of compression. This feature is also observed in the phase diagram, where p_0 of 4T1 cells increases from 3.404 to 3.894

in response to compression. This E-cadherin – p_0 comparison solidifies our experimental – theoretical mapping.

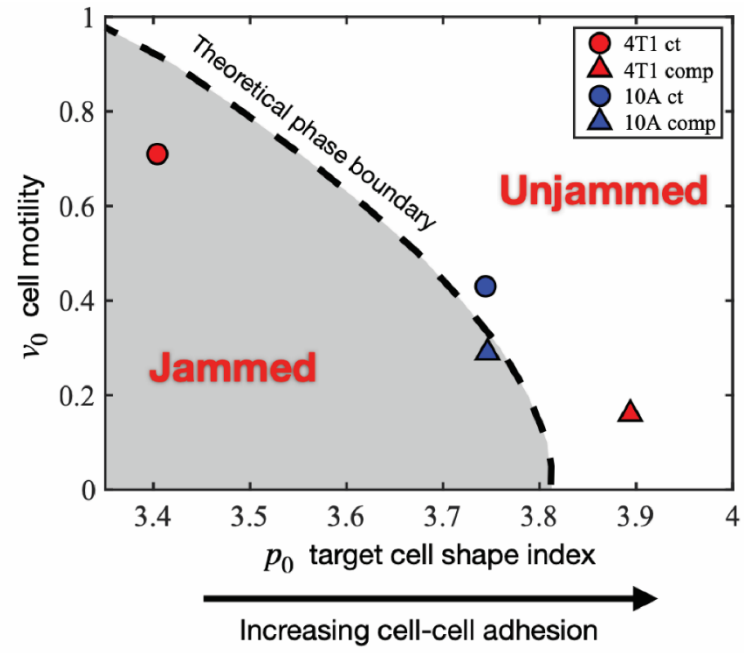

Figure 2.13. Mapping the experimentally observed tissue states to the theoretical jamming—unjamming phase diagram.

The jamming—unjamming phase diagram is shown in terms of the two pertinent parameters of the SPV model: the single cell motility v_0 and the target cell shape index p_0. By mapping the experimentally observed cell traction forces and cell shapes to theoretical simulation results, the positions of 4T1 and 10A cells are placed on the phase diagram (see **Methods**).

Under the effect of compression, the initially jammed 4T1 cells become unjammed, crossing the phase boundary, and undergoing a decrease in v_0 and an increase in p_0. In the model, this corresponds to decreased single cell motility and increased cell-cell adhesion. In contrast, MCF10A cells went from unjammed to jammed as a result of compression, suffering a small decrease in v_0 and no change in p_0. Using a jammed—unjammed boundary, we were able to see

two distinct transition paths taken by 4T1 and MCF10A cells under mechanical compression.

2.5 Discussion

In the present study, I show that cell-cell adhesion is an important mechanism for unjamming transitions in a mechanically stressed monolayer. I first establish increased collective cell migration in a transition correlated with cell shape and distinct from EMT. Increased migratory behavior has traditionally been associated with EMT (*48, 151, 152*), during which cells lose epithelial features and become mesenchymal. However, in the transition I observe, coordinated migration is enhanced, and the tissue fluidizes as the epithelial marker E-cadherin is upregulated and the mesenchymal marker vimentin is downregulated. These findings support a recently published characterization of the unjamming transition in which epithelial character is maintained without gaining mesenchymal character (*49*). As cell-cell adhesion increases, cells undergo a fluid-like unjamming transition, during which collective cell motion is increased and wound repair is accelerated. I discover that E-cadherin knockdown inhibits coordinated migration under mechanical compression, demonstrating that strong cell-cell adhesion, accompanied by the accumulation of vinculin at intercellular contacts, is important for regulating unjamming transitions. The attenuation of traction stresses in micropatterned MCF10A and 4T1 cell islands suggests that substrate traction may not be the dominant parameter in compression-induced unjamming transitions. Further investigation of cell traction during wound healing suggests that in a compressed 4T1 cell sheet, the cells within the bulk monolayer present substantially lower traction forces and higher cell-cell adhesion, allowing for greater structural rearrangements and highly correlated, fluid-like migration where the bulk cells are more easily pulled by the cells at the leading edge. Our results suggest that 4T1 cells respond to compressive stress by elongating, strengthening cell-cell adhesions, and

reducing traction within the bulk monolayer, leading to increased fluidization of the cell sheet and highly coordinated migration during wound healing.

One open question is how compressive stress leads to increased recruitment of E-cadherin to promote cell-cell adhesion. Mechanical stimuli are known to remodel epithelial cell-cell junctions by junction elongation and contraction mediated via mechanosensitive channels (*153*). It is also well documented that adherens junctions become reinforced when cells are under tension (*122, 154, 155*). Our lab has previously found that mechanical compression activates mechanosensitive channel Piezo1 leading to calcium influx using a similar experimental setup (*128*). Interestingly, it was recently identified that Piezo1 directly binds to E-cadherin, and Piezo1 is tethered to the actin cytoskeleton via the cadherin-β-catenin complex (*156*). While these findings help support the idea of cell-cell junction stabilization during mechanical perturbation, it remains enigmatic how compressive stress could increase recruitment of E-cadherin to the cell membrane. Surface expression of E-cadherin would be a balance of endocytosis and vesicular trafficking to the plasma membrane (*157*). Imbalance of trafficking of E-cadherin, for instance by reduced constitutive endocytosis, would alter the surface level of E-cadherin. Our lab and others have shown that endocytosis is reduced when cell tension is elevated (*132, 158, 159*). Thus, it is plausible that elevated tension, due to the application of compressive stress, could slow down the turnover of E-cadherin on the cell surface. It becomes more interesting considering that cancer cells are softer than normal cells (*160, 161*). A softer cell would become more deformed for a given compressive stress compared to a stiffer cell. In this way, the plasma membrane of cancer cells becomes more stretched by compressive stress, thereby resulting in reduced endocytosis and membrane protein turnover. Whether this could contribute to the increased E-cadherin level at cell-cell junctions in cancer cells in response to compressive stress remains to be further investigated.

It will also be of great interest to understand how upregulation of cell-cell adhesion translates to cells detaching from the solid tumor and migrating to adjacent tissues (*148*). The fluid-like transition I observe occurs when mechanical compression strengthens adherens junctions, maintaining high cell density and enabling cancer cells to migrate collectively in a coordinated manner. Recent studies found that the deregulation of adherens junctions in epithelial migration results in a transition from coordinated to uncoordinated collective movement, whereas increased collagen density leads to local cell individualization (*50*). I found that the front velocities of migrating 4T1 cell sheets increased with E-cadherin KD, consistent with what was recently reported (*50*). However, the application of compressive stress to E-cadherin KD cells reduced front velocity, indicating that compressive stress activates mechanotransduction pathways to influence collective cell migration. In cancer cells, heterogeneities in cell-cell adhesion within a tumor may be exacerbated by ECM confinement, allowing individual cells and cell clusters to move separately from their neighbors. Further studies will be necessary to decipher how these heterogeneities impact collective migration and invasion. Furthermore, the sensitivity of different cell types to compressive stress may be related to characteristics of the nucleus. The nucleus is mechanosensitive, influences cellular force generation (*117*), and may be actively involved in unjamming transitions. During wound healing, nuclear tension has been reported to decrease with distance from the wound edge, indicating higher tension in cells near the wound edge than within the bulk cell sheet (*162*).

Our findings suggest a new physical picture of tumor development and cancer invasion, in which compressive stress inhibits the migratory activity of normal epithelial cells and permits cancer cells to migrate rapidly as a cohesive collective. The way 4T1 cells react to mechanical compression stimulates dense cell sheets to structurally rearrange in an unjamming transition that is not primarily driven by EMT. Cell-cell adhesion is an important regulator of jamming—

unjamming transitions, and increased adhesion strength and attenuation of traction forces within the bulk cell sheet govern unjamming transitions under compression.

Chapter 3 Matrix Stiffness Modulates 3D Spheroid Sorting and Burst-Like Collective Migration

This chapter is currently in submission and is available as a preprint in bioRxiv. G.C. and A.P.L. contributed to conceptualization, and G.C., X.L., S.C., and K.K. contributed to methodology. G.C., S.-S.L., S.C., and K.K. contributed to experimental investigation, and G.C. and X.L. contributed to visualization. X.L. and D.B. contributed to computational modeling. D.B. and A.P.L. provided supervision. G.C and X.L. contributed to the original draft, and G.C., S.-S.L., D.B., and A.P.L. contributed to review and editing.

3.1 Abstract

While it is known that cells with differential adhesion tend to segregate and preferentially sort, the physical forces governing sorting and invasion in heterogeneous tumors remain poorly understood. To investigate this, I develop a composite hydrogel that uncouples matrix stiffness and collagen fiber density and mimics changes in the stiffness of the tumor microenvironment to explore how physical confinement influences individual and collective cell migration in 3D spheroids. The mechanical properties of the hydrogel can be tuned through crosslinking and crosslink reversal. Using this hydrogel system and computational Self-Propelled Voronoi modeling, I show that spheroid sorting and invasion into the matrix depend on the balance between cell-generated forces and matrix resistance. Sorting is driven by high confinement and reducing matrix stiffness triggers a collective fluidization of cell motion. Cell sorting, which depends on cell-cell adhesion, is crucial

to this phenomenon, and burst-like migration does not occur for unsorted spheroids irrespective of matrix stiffness. The findings support a model where matrix stiffness modulates 3D spheroid sorting and unjamming in an adhesion-dependent manner, providing insights into the mechanisms of cell sorting and migration in the primary tumor and toward distant metastatic sites.

3.2 Introduction

The primary tumor microenvironment plays a crucial role in facilitating the movement of cancer cells beyond the primary tumor. These cells navigate through the stroma, eventually infiltrating nearby microvessels through the process of intravasation (*43, 163, 164*). In confined tumors that exhibit a high cellular density, cancer cells must proliferate and migrate in order to promote tumor growth and metastasis. However, unchecked proliferation within these restricted spaces can lead to confinement stress (*41, 124, 128*). This stress in turn induces changes in cell-cell interactions and influences tumor development and compartmentalization (*165, 166*). Many cell-cell interactions depend on E-cadherin-based cell-cell junctions to preserve tissue cohesion and maintain active force transmission (*50, 167, 168*). During cancer metastasis, E-cadherin is downregulated in the epithelial-to-mesenchymal transition (EMT), which destabilizes cell-cell junctions and promotes invasiveness (*169, 170*). Cancer invasion and metastasis have been shown to occur in both E-cadherin-expressing and -deficient tumors (*50*). However, how the tumor microenvironment directly impacts intercellular interactions in tumors exhibiting intratumoral heterogeneity remains unclear.

A heterogeneous cell composition effectively replicates the physiological tumor microenvironment and introduces heterotypic cell-cell interactions (*171, 172*). Heterotypic interactions between subpopulations of epithelial cells have been demonstrated to play a crucial

role in the collective invasion observed in primary breast tumors (*173, 174*). Mixtures of two cell types with differences in cell-cell adhesion have been observed to undergo sorting (*72, 175*), however the cell-cell and cell-substrate interactions driving such sorting in tumors are not well understood. Recent work suggests that changes to cell-cell adhesion associated with EMT are related to cell jamming and unjamming (*26, 53*). When cells are jammed, they behave as a solid-like state in which individual cellular motion becomes arrested, and unjamming represents a shift to a fluid-like state in which cells exchange neighbors and the tissue flows in response to fluctuations (*16, 19*). In essence, the physical mechanisms that orchestrate jamming—unjamming behavior are driven by cellular properties, such as cell-cell and cell-substrate interactions (*11*).

In addition to adherens junctions, microenvironmental conditions involving cell-substrate interactions play a key role in regulating collective migration (*45, 92*). Many cell types exert integrin-based traction forces on the extracellular substrate to migrate and higher cell-substrate adhesion leads to increased cell spreading and motility (*11, 30, 176*). Notably, the mechanical attributes of the substrate are also an important factor, as cells tend to spread more and migrate faster on stiffer substrates (*177–179*). Prior studies tuned matrix stiffness by changing the concentration of collagen (*79*). To disentangle the influence of matrix stiffness from that of collagen fiber density, I developed a tunable collagen-alginate composite hydrogel to investigate how physical forces, such as confinement stress, influence cancer cell invasion. Our choice of type I collagen, the most abundant ECM protein in mammals (*180*), stemmed from its ability to provide adhesion sites for cells. In contrast, alginate, which cells cannot adhere to, is viscoelastic and controls gel stiffness by tunable crosslinking (*113, 181*). By leveraging calcium and calcium chelators like ethylene glycol tetraacetic acid (EGTA), I can manipulate the stiffness of the hydrogel in a time-dependent manner, mimicking the physical properties found in the tumor

microenvironment. Invasive cancer cells can degrade collagen by secreting matrix metalloproteinases (MMPs) (*109*); however, alginate is not degradable and is more applicable to contexts where degradation is limited or not possible. Overall, collagen-alginate composite hydrogels offer the ability to adjust the matrix stiffness independently of collagen fiber density.

In our investigation into the impact of matrix stiffness on cancer migration, I propose that tumor cell migration occurs in two distinct stages. Mesenchymal cells are segregated and sorted to the tumor periphery, where they proliferate and secrete enzymes to degrade the surrounding ECM. Following this, cellular invasion takes place. In this study, I utilize a composite hydrogel with tunable mechanical properties to illustrate the critical role that ECM stiffness plays in tumor development and distant metastasis. When matrix degradation is limited in a stiff hydrogel with low available ECM space, the pressure inside the spheroid core increases, and the cells become jammed. A reduction in matrix confinement causes the collective fluidization of cell motion, propelling normal epithelial cells and cancer cells into the matrix with high velocity. Using a computational Self-Propelled Voronoi (SPV) model to simulate a heterogeneous tissue, I confirm the experimental finding and further show that decreasing the cell-medium contact tension downregulates confinement stress and leads to cell invasion. The results yield insights into the interplay between confinement stress, cell-cell adhesion, and 3D jamming–unjamming transitions in breast cancer metastasis.

3.3 Materials and Methods

3.3.1 Cell culture

The cell lines MCF10A, MCF7 and MDA-MB-231 were gifts from Sofia Merajver (University of Michigan). MCF10A cells were obtained from Gloria Heppner at the Michigan

Cancer Foundation where the cell line was originally developed, MCF7 cells were originally obtained from ATCC, and MDA-MB-231 cells were obtained from Janet Price (MD Anderson Cancer Center) where the cell line was originally developed. MCF10A cells were cultured in DMEM/F12 medium (Gibco) supplemented with 5% horse serum, 20 ng/ml epidermal growth factor (EGF), 0.5 μg/ml hydrocortisone, 100 ng/ml cholera toxin and 10 μg/ml insulin. MCF7 and MDA-MB-231 cells were cultured in DMEM medium (Gibco) supplemented with 10% FBS. Cells were cultured in a humidified atmosphere containing 5% CO_2 at 37°C.

3.3.2 Stable cell lines

Stable cell lines expressing EGFP or Lifeact-RFP were generated via lentiviral transduction. EGFP lentivirus was produced from pSMPVW-EGFP obtained from Andrew Tai (University of Michigan). The lentiviral transfer plasmid pLVX-puro-RFP-Lifeact was cloned from RFP-Lifeact obtained from Gaudenz Danuser (UT-Southwestern). Lentiviruses were generated by transfecting HEK 293T cells with the transfer vector, psPAX2 packaging vector, and pMD2.G envelope vector. Viral supernatant was collected 48 h after transfection and used to infect the target cell lines. After 24 h, transduced cells were selected with 2 μg/mL puromycin for 5 days.

3.3.3 E-cadherin knockdown

MCF10A cells expressing inducible shRNA knockdown of E-cadherin was generated using a transfer plasmid provided by Valerie Weaver at UCSF (*127*). The transfer vector consisted of a modified pLKO.1 neo plasmid (Addgene) with expression of the shRNA sequences under control of 3× copies of the lac operator. The E-cadherin shRNA had the following sequence: 5’ - GAACGAGGCTAACGTCGTAAT - 3’; scramble shRNA (Sigma #SHC002) had the following sequence:

CCGGCAACAAGATGAAGAGCACCAACTCGAGTTGGTGCTCTTCATCTTGTTGTTTTT.

MCF10A cells were transduced with E-cadherin shRNA or scramble non-targeting control shRNA for 48 h. shCDH1 and scramble cells were selected with 200 μg/ml G-418 (Sigma) and 2 μg/mL puromycin, respectively. E-cadherin knockdown was induced in shCDH1 cells by adding 200 μM isopropyl-β-D-thiogalactoside (IPTG; Sigma) 72 h prior to experiments.

3.3.4 Encapsulation of tumor spheroids in a collagen-alginate hydrogel

Inverse pyramidal PDMS microwells (AggreWell™, Stem Cell Technologies) were treated with anti-adherence rinsing solution (Stem Cell Technologies) to prevent cell adhesion. Cells were detached with 0.25% trypsin-EDTA (Life Technologies) and added to the microwells at a concentration of ~1,000 cells per microwell. For co-culture spheroids, MCF10A cells were mixed with MDA-MB-231, MCF7 or MCF10A shCDH1 KD cells at a 2:1 ratio. The cells were centrifuged at 300g for 5 min to aggregate the cells at the bottom of the microwells, and spheroids formed overnight. The following day, the spheroids were harvested from the microwells and encapsulated in collagen-alginate hydrogels consisting of 3 mg/ml type I rat tail collagen (RatCol, Advanced BioMatrix) and 0.25% alginate (Nalgin HG, Tilley Chemical). Subsequently, the hydrogels were incubated at 37°C for 1 h for collagen polymerization, and then the encapsulated spheroids were imaged (day 0). Alginate crosslinking density and hydrogel stiffness were independently modulated through the concentration of $CaCl_2$ that was added to the cell culture medium after imaging on day 0. On day 4, the spheroids were imaged and then washed 1× with PBS. Afterward, the spheroids were either fixed for immunofluorescence staining or incubated with 0, 5 or 10 mM EGTA in PBS for 1 h to reverse the alginate crosslinking process. The solution was then replaced with fresh medium, and on day 6, the spheroids were fixed for immunofluorescence staining.

The Young's moduli of collagen-alginate hydrogels were measured after 4 days of incubation with 0, 5 or 10 mM $CaCl_2$ using a MicroSquisher (CellScale). A microbeam with a

diameter of 203.2 μm, modulus of 411,000 MPa, and length of 59.5 mm was fixed to a 0.75 mm diameter glass bead and mounted to the vertical actuator. The samples were submerged in a solution of 1% BSA in PBS to reduce adhesion and compressed 3–4 times at different locations with a vertical displacement of 50–150 μm and at a loading rate of 1 μm/s. The Young's modulus was calculated using the linear slope of the stress-strain curve.

3.3.5 Confocal microscopy

Images were taken using an oil immersion UplanFL N 10 x/1.30 NA (Olympus) objective on an inverted microscope (Olympus IX-81) equipped with an iXON3 EMCCD camera (Andor Technology), National Instrument DAQ-MX controlled laser (Solamere Technology), and a Yokogawa CSU-X1 spinning disk confocal unit. Z-stack images of spheroids expressing EGFP or Lifeact-RFP and fluorescently labeled for DAPI were taken at excitation wavelengths of 488, 561 and 405 nm, respectively. Z-stack images of spheroids fluorescently labeled for E-cadherin, vimentin, or F-actin (by 670-phalloidin) were taken at an excitation wavelength of 640 nm.

3.3.6 Immunofluorescence staining and analysis

Spheroids embedded in hydrogels were washed with PBS and fixed with 4% paraformaldehyde for 1 h, washed with PBS, and permeabilized with 0.1% Triton X-100 in PBS for 4 h. Then, cells were washed with PBS and blocked with 3% BSA in PBS overnight at 4°C. The following morning, cells were incubated with a mouse anti-E-cadherin antibody at 1:500 (610181, BD Biosciences) or a rabbit anti-vimentin antibody at 1:400 (D21H3, Cell Signaling) in 3% BSA overnight at 4°C. Next, cells were washed 3× with PBS for 30 minutes per wash and incubated with DAPI and a secondary antibody in 3% BSA overnight at 4°C. Hydrogels were washed 3× with PBS as described above and imaged by spinning disk confocal microscopy.

To quantify cell sorting and the E-cadherin signal, the median slice from each z-stack was

analyzed. Using the Fit Ellipse and Centroid options in Fiji, the coordinates of the center of the spheroid and the semi-major axis of the spheroid were extracted. Using the Multi-point tool, the coordinates of individual cells were recorded. As a measure of cell sorting, the distance index (DI) was calculated by dividing the cell's distance from the spheroid center by the spheroid's semi-major axis (*175*). The E-cadherin signal at cell–cell contacts was quantified by measuring fluorescence intensity at the cell membrane and was calculated per cell by dividing the integrated density by the number of cells (indicated by DAPI) for each image.

3.3.7 Time-lapse imaging and analysis

For time-lapse imaging, images were acquired on an Olympus IX-81 inverted microscope, as previously described, or a Nikon-A1 laser scanning confocal microscope, equipped with an environmental chamber. Cell motility was recorded at 1-hour intervals over 18 or 24 h, with a 4 μm z-step. Individual cell trajectories were obtained using TrackMate in Fiji, where the LoG detector was used for spot detection with median filtering and subpixel localization, and the linear motion LAP tracker was used to link spots. After exporting the tracks as XML files, cell motility rates were calculated for each spheroid (*182*), and MSDs were analyzed using a MATLAB per-value class for MSD analysis of particle trajectories (*183*) and plotted in log-log scale, where the slope gives the diffusion coefficient α.

To calculate distance index from time-lapse sequences, z-stacks captured at 0, 8, 16 and 24 h were analyzed. Using the 3D projections of z-stacks taken at 0 h, the initial time point, the centroid location and semi-major axis of each spheroid were extracted in MATLAB via the "regionprops" function, which approximates spheroids as ellipses. Next, individual cell positions were acquired in TrackMate using the median slice of each z-stack. After exporting the cell coordinates as XML files, the distance index for each cell at all four time points was calculated using custom MATLAB

code.

3.3.8 Western blotting

Samples were run on SDS–PAGE 4–20% Bio-Rad gels (15 well/15 µl). SDS-PAGE gels were run at a constant 120 V for 90 min. Proteins were transferred to a nitrocellulose membrane using the iBlot transfer system and the membrane was blocked in 5% milk in TBS-T for 1 h at room temperature. Blots were incubated with a primary rabbit GAPDH antibody at 1:1000 (D16H11, Cell Signaling), a mouse anti-E-cadherin antibody at 1:2000 (610181, BD Biosciences), and a primary rabbit anti-vimentin antibody at 1:1000 (D21H3, Cell Signaling) in 5% BSA in TBS-T overnight at 4 °C. GAPDH was used as a loading control for quantifying relative gene expression. Blots were washed 3× with TBS-T, incubated with secondary antibodies for 1 h at room temperature, and then washed again with TBS-T as described above. Western blots were imaged using an Azure Biosystems Sapphire System.

3.3.9 Statistical analysis

Statistical analysis was carried out in Origin and performed with one-way ANOVA followed by Tukey post-hoc multiple comparisons test. Results were collected from three independent experiments and data from individual cells or spheroids were plotted as mean ± S.E. or shown as boxplots, depending on the experiment. Statistical significance was denoted by asterisks in the figure panels, with $* = p < 0.05$, $** = p < 0.01$, $*** = p < 0.001$.

3.3.10 Self-Propelled Voronoi (SPV) model of a heterogeneous tissue

To investigate how cells behave invasively under different confinement levels, we use the recently developed Self-Propelled Voronoi (SPV) model (*18, 184*). In the SPV model, the basic degrees of freedom are the set of 2D cell centers $\boldsymbol{r}_i$ and cell shapes are given by the resulting Voronoi tessellation. The complex biomechanics that govern intracellular and intercellular

interactions can be coarse-grained (*33, 36, 185–189*) and expressed in terms of a mechanical energy functional for individual cell shapes.

$$E = \frac{1}{2}\sum_{i=1}^{N}[K_A(A_i - A_0)^2 + K_P(P_i - P_0)^2] + 2\sum_{<ij>}\lambda_{ij}L_{ij}\,. \qquad (1)$$

The SPV energy functional is quadratic in both cell areas (A_i) with modulus K_A and cell perimeters (P_i) with modulus K_P. The parameters A_0 and P_0 set the preferred values for area and perimeter, respectively. To simulate a heterogeneous tissue (*190*), we have a linear tension term in the energy function Eq. (1). λ_{ij} is the junctional tension shared by cells i and j with contact edge length L_{ij}. In a heterogeneous tissue with two types of cells, λ_{ij} is determined by the cell type of i and j. For example, in a tissue with two cell types A and B, we can define tensions as τ_{AA}, τ_{BB} and τ_{AB} for A-A, B-B and A-B cell contacts.

The deformation of the actin-myosin cortex concentrated near the cell membrane is mainly responsible for changes to cell perimeters. After expanding Eq. (1), the term $\frac{1}{2}K_P P_i^2$ corresponds to the elastic energy associated with deforming the cortex. The linear term in cell perimeter, $-K_P P_0 P_i$, and $\lambda_{ij}L_{ij}$ represent the effective line tension in the cortex and gives rise to a 'preferred perimeter' P_0. The value of P_0 can be decreased by upregulating the contractile tension in the cortex (*33, 187, 188*) and it can be increased by upregulating cell-cell adhesion. A_0 is set to be equal to the average area per cell and $\sqrt{A_0}$ is used as the unit of length. After non-dimensionalizing Eq. (1) by $\frac{1}{2}K_A A_0^2$ as the unit energy scale, we choose $K_P/(K_A A_0) = 1$ such that the perimeter and area terms contribute equally to the cell shapes. The choice of K_P does not affect the results presented. The preferred cell

perimeter is rescaled $p_0 = P_0/\sqrt{A_0}$ and varied between 3.7 (corresponding to the perimeter of a regular hexagon with unit area) and 4.6 (corresponding to the perimeter of an equilateral triangle with unit area) (*33*). The ground states of Eq. 1 are amorphous tilings where the cells have approximately equal area, but varying perimeters as dictated by the preferred cell perimeter p_0. It has been shown that at a critical value of $p_0^* \approx 3.81$, the tissue collectively undergoes a solid-fluid transition (*33*). When $p_0 < p_0^*$, the cells must overcome finite energy barriers to rearrange and the tissue behaves as a solid, while above p_0^*, the tissue behaves as a fluid with a vanishing shear modulus as well as vanishing energy barriers for rearrangements (*33*).

The effective mechanical interaction force experienced by cell i is defined as $\boldsymbol{F}_i = -\boldsymbol{\nabla}_i E$. In addition to $\boldsymbol{F}_i$, cells can also move due to self-propelled motility. Just as in SPP models, we assign a polarity vector $\hat{\boldsymbol{n}}_i = (\cos\theta_i, \sin\theta_i)$ to each cell; along $\hat{\boldsymbol{n}}_i$ the cell exerts a self-propulsion force with constant magnitude v_0/μ, where μ is the mobility (the inverse of a frictional drag). Together these forces control the over-damped equation of motion of the cell center $\boldsymbol{r}_i$

$$\frac{d\boldsymbol{r}_i}{dt} = \mu \boldsymbol{F}_i + v_0 \hat{\boldsymbol{n}}_i. \qquad (2)$$

The polarity is a minimal representation of the front/rear characterization of a motile cell (*191*). While the precise mechanism for polarization in cell motility is an area of intense study, here we model its dynamics as a unit vector that undergoes random rotational diffusion,

$$\begin{aligned} \partial_t \theta_i &= \eta_i(t), \\ \langle \eta_i(t)\eta_j(t')\rangle &= 2D_r \delta(t-t')\delta_{ij}, \end{aligned} \qquad (3)$$

where θ_i is the polarity angle that defines $\hat{\boldsymbol{n}}_i$, and $\eta_i(t)$ is a white noise process with zero mean and variance $2D_r$. The value of angular noise D_r determines the memory of stochastic noise in the system, giving rise to a persistence time scale $1/D_r$ for the polarization vector $\hat{\boldsymbol{n}}$.

The mechanical state of cell i is characterized by a local stress tensor $\sigma^i_{\alpha\beta}$ given by (*34*, *192*)

$$\sigma^i_{\alpha\beta} = -\Pi_i \delta_{\alpha\beta} + \frac{1}{2A_i} \sum_{l_{ij} \in i} \tau^{\alpha}_{ij} l^{\beta}_{ij}, \qquad (4a)$$

$$\Pi_i = -\frac{\partial E}{\partial A_i}, \quad \tau_{ij} = \frac{\partial E}{\partial \mathbf{l}_{ij}}, \qquad (4b)$$

where $\tau_{ij} = \tau_{ij}\hat{\boldsymbol{l}}_{ij}$ is the edge tension shared by cell i and j with $\hat{\boldsymbol{l}}_{ij} = \boldsymbol{l}_{ij}/|\boldsymbol{l}_{ij}|$, and Π_i is the hydrostatic cellular pressure. Here $i, j, \ldots$ are cell labels, and α, β denote Cartesian components. Both the tension along the edge and the intracellular pressure force perpendicularly to an edge contribute to the mechanical force balance at every vertex for a solid tissue (*193*). In our simulations, the instantaneous tensions and pressures can be calculated based on Eq. (4b),

$$\tau_{ij} = K_P\big[(P_i - P_0) + \big(P_j - P_0\big)\big] + 2\lambda_{ij}, \; \Pi_i = -K_A(A_i - A_0), \qquad (5)$$

where P_i is the perimeter and A_i is the area of cell i respectively. The tissue stress is related to the cellular stress as

$$\sigma_{\alpha\beta} = \frac{1}{A_T}\sum_i A_i\,\sigma^i_{\alpha\beta}, \qquad (6)$$

where A_T is the area of the tissue. The tissue compressive stress is the trace of the stress tensor $\sigma_n = (\sigma_{xx} + \sigma_{yy})/2$.

We simulate tissues containing two cell types (A and B) under periodic boundary condition. Each cell type has $N_A = N_B = 72$ cells. To initialize the simulation, a set of random cell centers are generated. Each cell is also randomly assigned a cell index and cell type label, A or B. $A_0 = 1$, $P_0 = 4.2$ and motility $v_0 = 0.3$ are set to be constant values for all cells throughout the simulations. The cell shapes are obtained via Voronoi tessellations based on cell centers at each time step of the simulation. Therefore, the initial configuration is an amorphous tissue with cells A and B randomly mixed.

Junctional tensions are defined based on the types of neighboring cells, τ_{AA}, τ_{BB} and τ_{AB} for A-A, B-B, and A-B cell contacts. In accordance with prior studies of cell sorting and the differential adhesion hypothesis (*74*, *75*), we set $\tau_{AB} > \frac{\tau_{AA}+\tau_{BB}}{2}$ to obtain an engulfed state.

Subsequently, we used the engulfed configuration as the starting state and manipulate the contact tensions between cells and medium τ_{AM} and τ_{BM}, to investigate the effects of confinement on cell invasion. We solved Eq. (2) using Euler's method by running 2×10^5 steps with time interval $\Delta t = 0.01$. To quantify the cell invasion, we calculated the sorting index $I_A = 1 - N_{A\ cluster}/N_A$ for A cells and $I_B = 1 - N_{B\ cluster}/N_B$ for B cells under changing confinements. Here, $N_{A\ cluster}$ means the total number of isolated clusters of A cells. When the state is well sorted, there is only one A or B cell cluster, and the sorting index is $I \approx 1$. At low confinement, cells are

invading into the medium to form a mixed configuration, therefore the sorting index is $I \approx 0$.

3.4 Results

3.4.1 3D matrix confinement inhibits single-cell cancer migration

Spheroids are extensively utilized as a three-dimensional in vitro multicellular model, mirroring the structure and function of tissues (*81*, *82*). To form co-culture spheroids, I selected MCF10A, a non-tumorigenic breast epithelial cell line, and MDA-MB-231, a triple negative, highly invasive cancer cell line (*194*). MCF10A cells have stable adherens junctions with high E-cadherin expression, whereas MDA-MB-231 cells lack E-cadherin (*195*). I generated stable cell lines expressing Lifeact or a soluble fluorescence protein as markers to denote different cell types and mixed normal epithelial cells and cancer cells to replicate intratumoral heterogeneity. Subsequently, I encapsulated mixed spheroids in collagen-alginate hydrogels and manipulated the matrix stiffness by varying the concentration of $CaCl_2$ to crosslink alginate (**Figure 3.1A**), yielding Young's moduli ranging from ~2.67 kPa to ~5.75 kPa (**Figure 3.2**). This falls within the ECM stiffness range of 2-20 kPa found in breast tumors (*196*, *197*). By maintaining the concentration of collagen, the number of cell adhesion sites, which depend on the density of collagen fibers, remains constant.

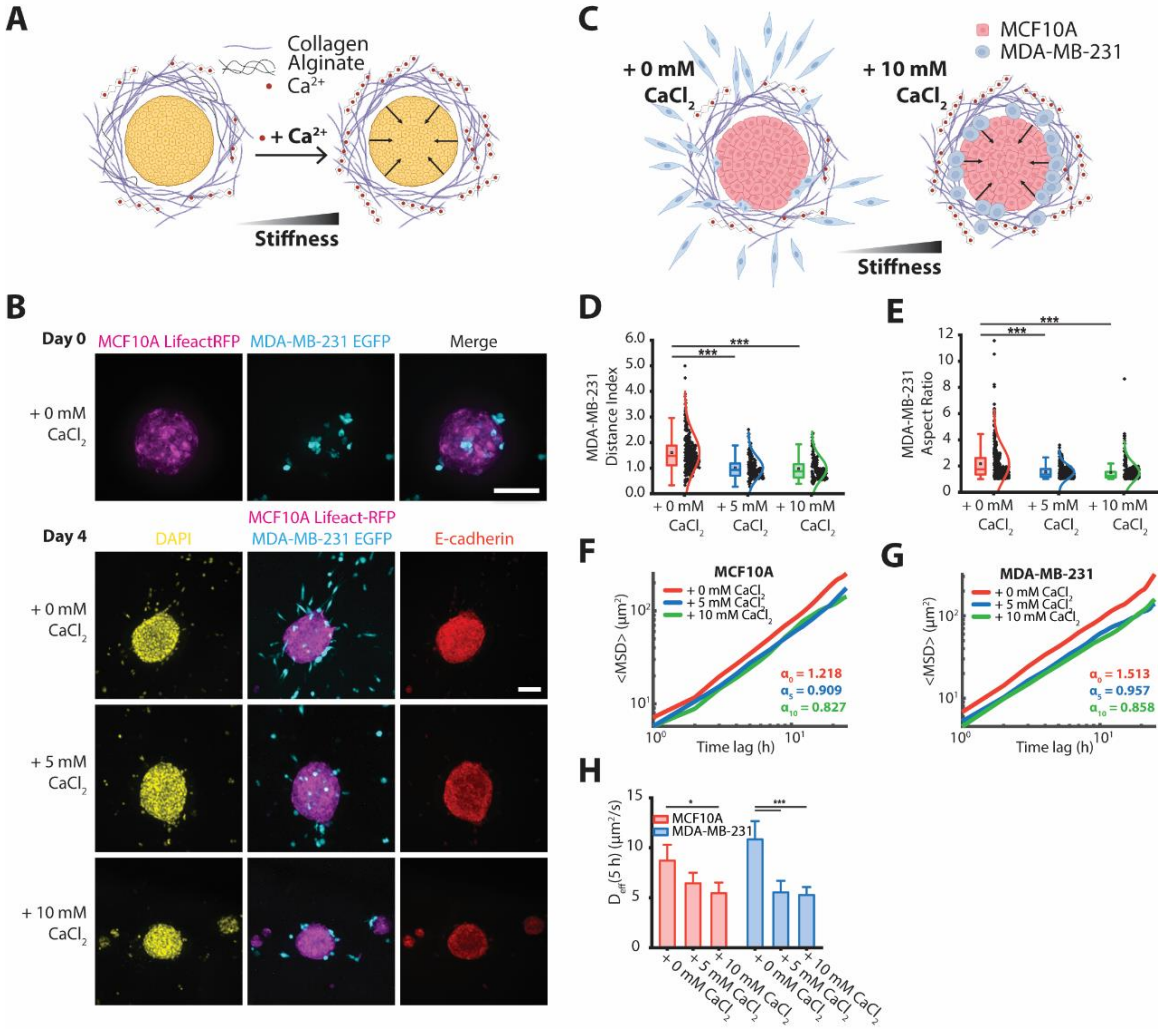

Figure 3.1. 3D matrix confinement inhibits the migration of cancer cells in co-culture spheroids.

(A) Schematic depicting a spheroid encapsulated in a collagen-alginate hydrogel. Adding Ca^{2+} to crosslink sodium alginate into calcium alginate increases matrix stiffness, leading to high matrix confinement. **(B)** Representative fluorescence images of MCF10A and MDA-MB-231 co-culture spheroids encapsulated in collagen-alginate hydrogels, imaged on days 0 and 4, and immunostained for E-cadherin and DAPI. On day 0, the spheroids were encapsulated and 0, 5 or 10 mM $CaCl_2$ was added. **(C)** Schematic depicting a MCF10A (red) and MDA-MB-231 (blue) co-culture spheroid embedded in a collagen-alginate hydrogel. Addition of Ca^{2+} increases confinement stress. **(D)** Boxplot of distance index for MDA-MB-231 cells in co-culture spheroids (with MCF10A cells) after 4 days of culture. **(E)** Boxplot of cell aspect ratio for MDA-MB-231 cells on day 4. **(F & G)** Mean square displacements (MSDs) of **(F)** MCF10A EGFP cells or **(G)** MDA-MB-231 EGFP cells in co-culture spheroids (with MCF10A Lifeact-RFP cells) plotted over an 18-h period. Each line represents the mean

MSD for n = 12 spheroids. The plots are shown in log-log scale, and the power law exponent α is shown for each condition. **(H)** Effective diffusion coefficient is shown for MCF10A and MDA-MB-231 cells for n = 12 spheroids per condition. Scale bars are 90 µm. ∗ = $p < 0.05$, ∗∗∗ = $p < 0.001$.

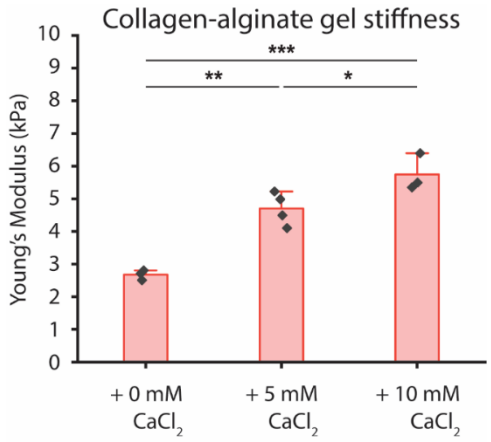

Figure 3.2. Collagen-alginate hydrogel stiffness increases with calcium concentration.

Young's moduli of collagen-alginate hydrogels measured by a MicroSquisher following 4 days of incubation with 0, 5 or 10 mM $CaCl_2$. Error bars denote S.E. * $p < 0.05$, ** $p < 0.01$, *** $p < 0.001$.

Over the course of 4 days, MDA-MB-231 cells sorted to the spheroid boundary and migrated as single cells into the surrounding matrix, depending on hydrogel stiffness (**Figure 3.1, B and C**). Under low confinement, single cancer cells escaped the tumor spheroid and invaded into the hydrogel after 4 days of culture, whereas the higher confinement in crosslinked gels inhibited cancer cell migration into the matrix (**Figure 3.1B**). Breast carcinoma cells, which are known to be mechanically soft compared to the surrounding normal cells (*195*), possessed low F-actin (**Figure 3.3**), suggesting higher deformability than the MCF10A cells confined to the spheroid. As a measure of cell sorting and migration, a distance index was calculated for each cell using the relative distance of the cell to the spheroid center (*175*). Cancer cells in hydrogels with low matrix stiffness

exhibited a higher distance index (**Figure 3.1D**) and were more elongated (**Figure 3.1E**). Although MDA-MB-231 cells localized to the spheroid boundary after 4 days of culture regardless of gel stiffness, high matrix stiffness restricted the cancer cells to the periphery and prevented invasion into the matrix. Furthermore, cancer cells cultured in a stiffer matrix displayed a round morphology (**Figure 3.1B**). Cancer cell invasion was not impeded in mixed spheroids cultured in collagen gels with 10 mM $CaCl_2$ (**Figure 3.4**), showing that the behavior observed was not caused by the presence of calcium.

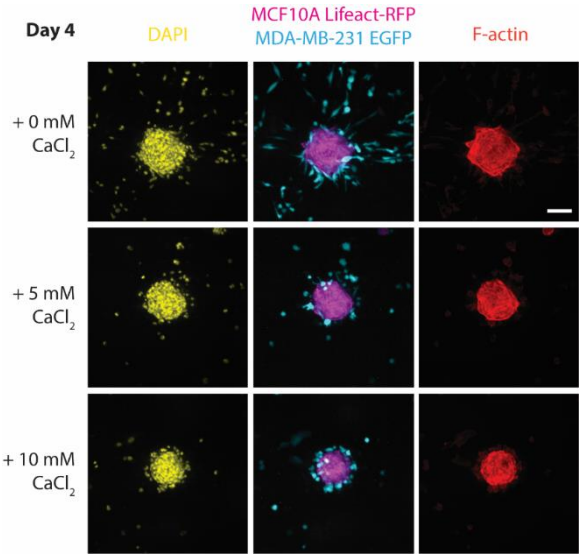

Figure 3.3. High confinement inhibits cancer cell migration in collagen-alginate hydrogels.

Representative fluorescence images of MCF10A Lifeact-RFP and MDA-MB-231 EGFP co-culture spheroids embedded in collagen-alginate hydrogels with different concentrations of $CaCl_2$ and stained for DAPI and F-actin after 4 days of culture. Scale bar: 90 µm.

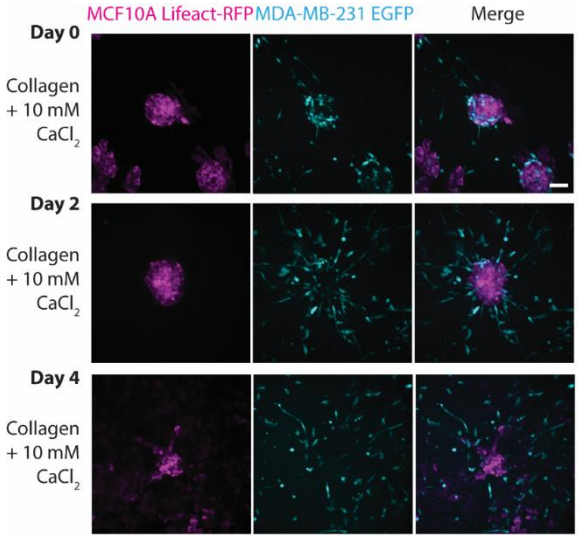

Figure 3.4. MCF10A and MDA-MB-231 mixed spheroids cultured in collagen hydrogels invade into the surrounding matrix.

Representative fluorescence images of MCF10A Lifeact-RFP and MDA-MB-231 EGFP co-culture spheroids embedded in collagen hydrogels with different concentrations of $CaCl_2$ and imaged at days 0, 2 and 4. On day 0, the spheroids were encapsulated and 10 mM $CaCl_2$ was added. Scale bar: 90 µm.

To study the kinematics of 3D cancer cell migration in co-culture spheroids, I performed experiments with varying degrees of alginate crosslinking and computed the mean square displacement (MSD) in log-log scale of cells in different conditions of matrix confinement, with the average slopes (α values) representing super-diffusive ($\alpha > 1$), diffusive ($\alpha = 1$), and sub-diffusive ($\alpha < 1$) cell motility (*175*, *183*). Under low confinement, MDA-MB-231 cells were more diffusive than MCF10A cells (i.e., α of ~1.51 vs. ~1.21), whereas diffusivity was similar for both cell types under high confinement (i.e., α of ~0.86 vs. ~0.83, **Figure 3.1, F and G**). Normal breast epithelial cells and cancer cells both demonstrated lower diffusivity when cultured in crosslinked hydrogels (**Figure 3.1H**). Cancer cells cultured in hydrogels with low matrix stiffness were more elongated, which possibly correlated with super-diffusive behavior (**Figure 3.1G**), linking cell

shape to diffusive motion (*10*, *117*).

3.4.2 High ECM confinement drives spheroid sorting

To investigate how the metastatic potential of the cancer cell line impacts migration behavior under confinement, I generated MCF10A and MCF7 co-culture spheroids. MCF7 is a poorly metastatic breast epithelial cell line that does not express membrane type 1-matrix metalloproteinase 1 (MT1-MMP)/MMP14 (*50*). As a result, MCF7 cells are unable to degrade or remodel ECM and are non-invasive. When under matrix confinement due to alginate crosslinking, these mixed spheroids undergo different degrees of sorting, showing minimal sorting in 0 mM $CaCl_2$, intermediate sorting in 5 mM $CaCl_2$, and complete sorting in 10 mM $CaCl_2$ (**Figure 3.5, A and B**). After 4 days of culture, mixed spheroids cultured in low-stiffness hydrogels were significantly larger than those cultured in crosslinked, stiffer hydrogels (**Figure 3.6**). To quantify the spatial organization of MCF10A and MCF7 cells within spheroids as matrix confinement increased, I measured the distance index for the subpopulations, which yielded notable cell sorting under high matrix stiffness (**Figure 3.5C**). Cell sorting was evident, as the subpopulations were distinctly separated into the core and edge regions of the spheroids **(Figure 3.5C)**. This observation is correlated with differences in E-cadherin expression, as measured by fluorescence intensity normalized to the number of each cell type, where MCF10A cells at the core expressed higher E-cadherin levels than MCF7 cells localized to the boundary compartment (**Figure 3.5D**). As a measure of the differential E-cadherin expression in sorted spheroids, the relative adhesion ratio was calculated for individual spheroids as the ratio of E-cadherin expression of the adhesive cell type to the less adhesive cell type, based on their fluorescence intensity (**Figure 3.5E**). The adhesion ratio increased with spheroid sorting in hydrogels with high matrix stiffness, indicating that sorting is indeed linked to intercellular adhesion strength, consistent with the differential adhesion

hypothesis (DAH) (*74*).

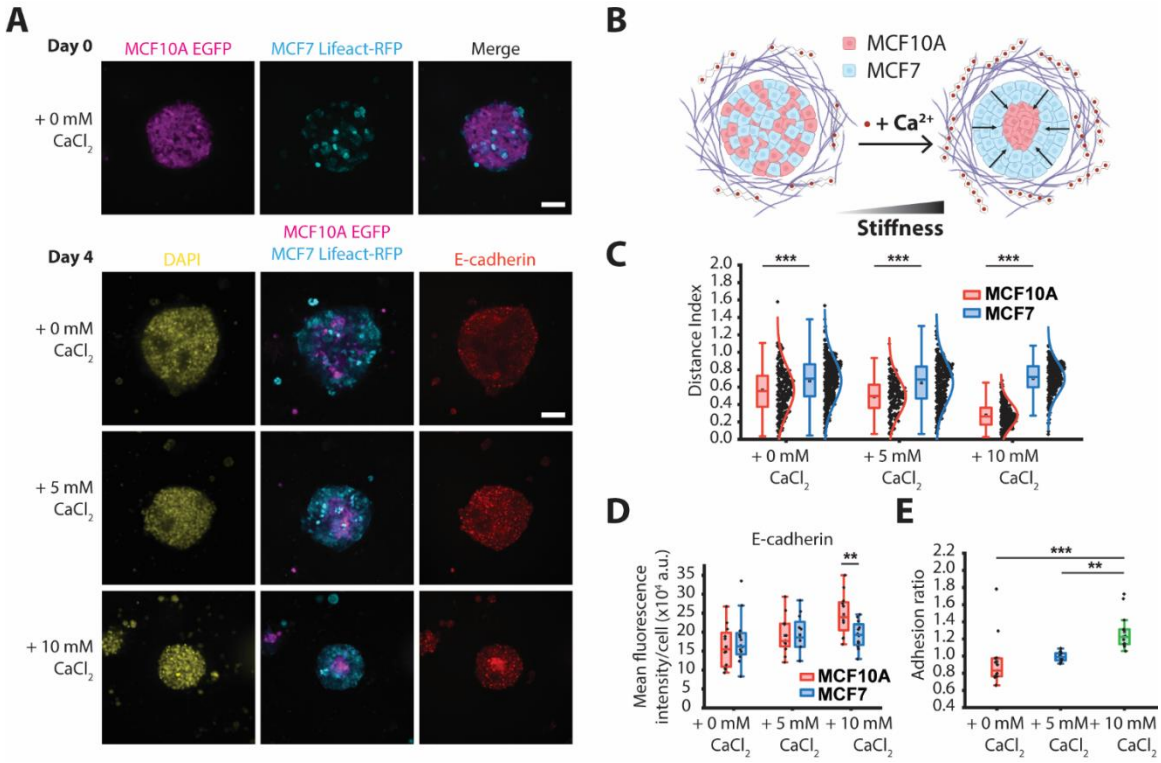

Figure 3.5. High confinement drives cell sorting in co-culture spheroids.

(A) Fluorescence images of MCF10A and MCF7 co-culture spheroids encapsulated in collagen-alginate hydrogels and imaged on day 0 (day of encapsulation). 0, 5 or 10 mM $CaCl_2$ was added on day 0, and the spheroids were imaged again on day 4. Spheroids were immunostained for E-cadherin and stained for DAPI. Scale bar: 90 µm. **(B)** Schematic depicting a MCF10A (red) and MCF7 (blue) co-culture spheroid embedded in a collagen-alginate hydrogel. Under high matrix confinement, MCF7 cells sort to the periphery and MCF10A cells form a cluster at the spheroid core. **(C)** Boxplot of distance index for MCF10A and MCF7 cells after 4 days of culture (n = 12 spheroids per condition). **(D)** Boxplot of E-cadherin fluorescence per cell for MCF10A and MCF7 co-culture spheroids on day 4 (n = 12 spheroids per condition). **(E)** Boxplot of the corresponding relative adhesion ratio of MCF10A and MCF7 co-culture spheroids. Scale bars are 90 µm. ∗∗ = $p < 0.01$, ∗∗∗ = $p < 0.001$.

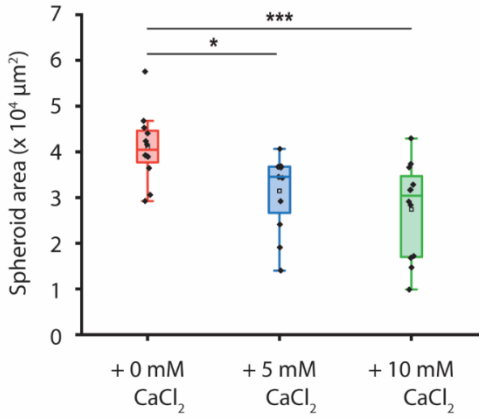

Figure 3.6. The size of MCF10A and MCF7 mixed spheroids decreases with increasing matrix stiffness.

Boxplot of spheroid area for MCF10A and MCF7 co-culture spheroids in collagen-alginate hydrogels after 4 days of culture with 0, 5 or 10 mM $CaCl_2$. * $p < 0.05$, *** $p < 0.001$.

Moreover, under high matrix stiffness, mixed spheroids transitioned from a homogeneous adhesion state to a sorted state with a defined core with high adhesion and a boundary compartment with low adhesion. These results suggest that physical confinement stress generated by the mechanical properties of the matrix was sensed by and transduced through cells, resulting in differential sorting. To confirm that the sorting behavior observed was not induced by the addition of calcium, I showed that the spheroids failed to sort when cultured in collagen gels with 10 mM $CaCl_2$ that had a Young's modulus of ~2 kPa (**Figure 3.7**). Together, these experiments indicate that, in our model system, cell sorting is driven by increased matrix stiffness and is dependent on cell-cell adhesions.

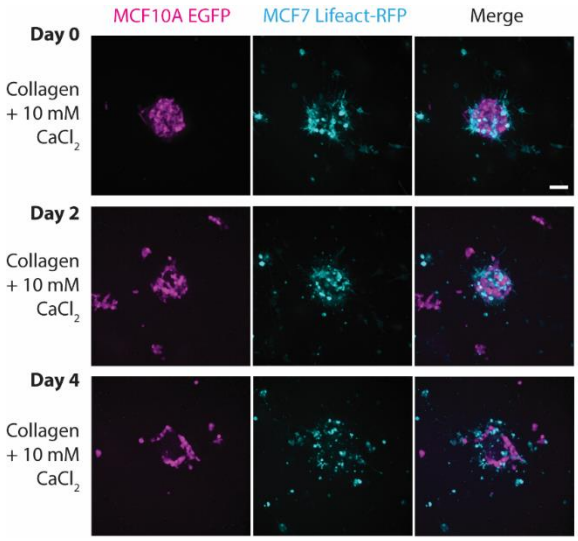

Figure 3.7. MCF10A and MCF7 co-culture spheroids fail to sort in collagen hydrogels.

Representative fluorescence images of MCF10A EGFP and MCF7 Lifeact-RFP co-culture spheroids embedded in collagen hydrogels with different concentrations of $CaCl_2$ and imaged at days 0, 2 and 4. On day 0, the spheroids were encapsulated and 10 mM $CaCl_2$ was added. Scale bar: 90 µm.

3.4.3 Tumor spheroid sorting depends on E-cadherin expression

When investigating the correlation between sorting and differential E-cadherin upregulation, I observed that monoculture MCF10A Lifeact-RFP and MCF10A EGFP spheroids failed to sort when subjected to high matrix confinement (**Figure 3.8A**), consistent with our hypothesis that sorting is linked to differences in cell–cell junction strength and stability. In the absence of alginate, MCF10A spheroids collectively invaded into the surrounding matrix when cultured in collagen gels with 10 mM $CaCl_2$ (**Figure 3.9**). However, when embedded in collagen-alginate gels, MCF10A spheroids neither sorted nor invaded due to a lack of space in the composite hydrogel network. MCF10A E-cadherin levels decreased when cultured in hydrogels with high matrix stiffness (**Figure 3.8B**), and a similar result was found when MCF10A cells were co-cultured

with invasive mesenchymal cells (**Figure 3.1B**). Thus, the sorting behavior observed in mixed spheroids is likely attributed to the difference in E-cadherin expression in breast cancer cells and normal breast epithelial cells.

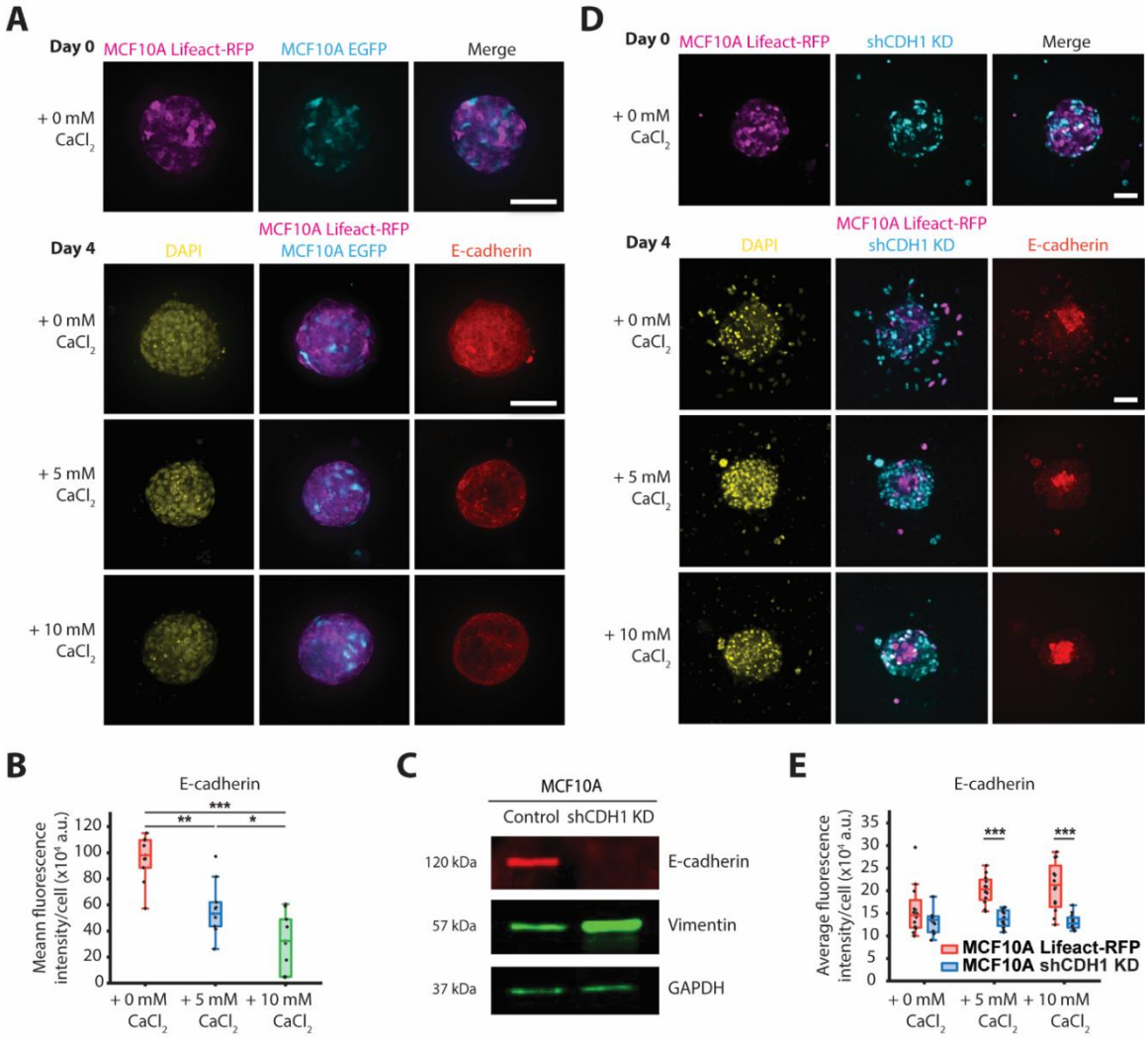

Figure 3.8. Tumor spheroid sorting depends on E-cadherin expression.

(A) Representative fluorescence images of MCF10A Lifeact-RFP and EGFP co-culture spheroids encapsulated in collagen-alginate hydrogels and imaged on day 0 (day of encapsulation) and day 4 (day of fixation). Spheroids were immunostained for E-cadherin and stained for DAPI. **(B)** Boxplot of E-cadherin fluorescence per cell for MCF10A Lifeact-RFP and EGFP spheroids in hydrogels with 0, 5 or 10 mM $CaCl_2$.

(C) Western blot illustrating IPTG-induced shCDH1 KD in MCF10A cells and of vimentin expression in MCF10A scramble and shCDH1 KD cells. GAPDH was used as the loading control. **(D)** Representative fluorescence images of MCF10A Lifeact-RFP and shCDH1 KD mixed spheroids imaged on days 0 and 4. $CaCl_2$ was added on day 0. **(E)** Boxplot of E-cadherin fluorescence per cell for MCF10A Lifeact-RFP and shCDH1 KD subpopulations in co-culture spheroids (n = 12 spheroids per condition). Scale bars are 90 µm. $* = p < 0.05$, $** = p < 0.01$, $*** = p < 0.001$.

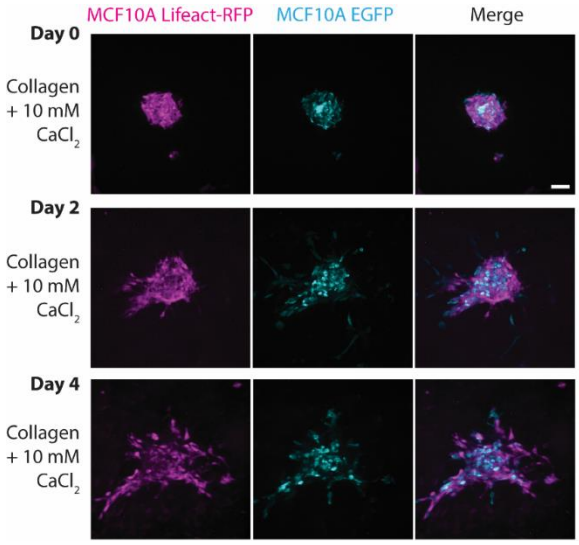

Figure 3.9. MCF10A spheroids cultured in collagen hydrogels invade into the surrounding matrix.

Representative fluorescence images of MCF10A Lifeact-RFP and EGFP spheroids embedded in collagen hydrogels and imaged at days 0, 2 and 4. On day 0, the spheroids were encapsulated and 10 mM $CaCl_2$ was added. Scale bar: 90 µm.

Next, I asked if differences in E-cadherin expression regulated spheroid sorting. I knocked down E-cadherin (encoded by CDH1 gene) in MCF10A cells with inducible short hairpin RNA (shRNA) (**Figure 3.8C**), as previously established (*41*, *127*), generating shCDH1 KD cells. Subsequently, MCF10A Lifeact-RFP and MCF10A shCDH1 KD co-culture spheroids were formed. The DAH proposes that strongly adhesive cells have a higher tissue surface tension and should preferentially adhere to each other and be enveloped by less adhesive cells. In agreement

with the DAH, Lifeact-RFP cells clustered together at the core of the spheroid and were surrounded by layers of shCDH1 KD cells (**Figure 3.8D**). In low-stiffness hydrogels, single cells detached from the spheroid and migrated into the surrounding matrix. Calculating the distance index for the distinct subpopulations in mixed spheroids generated a clear spatial separation between the different cell types in hydrogels with high matrix stiffness (**Figure 3.8D**). According to the DAH, tumors behave like fluids, and surface tension-like effects hold shCDH1 KD cells and non-invasive cancer cells within the spheroid boundary (*72, 74*). Since these cells lack the ability to remodel ECM, they are unable to break through compartment boundaries and invade into the surrounding matrix. shCDH1 KD cells in co-culture exhibit the same sorting behavior observed in MCF7 cells, showing that the sorting process is regulated by the difference in E-cadherin expression between the co-culture cell types (**Figure 3.8E**).

3.4.4 Sorted tumor spheroids unjam when matrix confinement is released

Having established that spheroid sorting is a result of increased matrix stiffness, I then investigated whether reducing matrix stiffness will permit invasion. Addition of the calcium chelator EGTA relieves crosslinked alginate by binding to and removing calcium ions from the crosslinked hydrogel, lowering matrix confinement. MCF10A Lifeact-RFP and MCF10A EGFP spheroids were used as a control and cultured in a medium with 10 mM $CaCl_2$ (**Figure 3.10A**). Then, after 4 days of culture, the spheroids were treated with 0 or 5 mM EGTA. Fluorescence imaging 2 days after treatment showed that EGTA-treated control spheroids did not migrate into the surrounding matrix (**Figure 3.10A**), indicating that EGTA treatment and reduced matrix stiffness do not initiate invasion in unsorted spheroids.

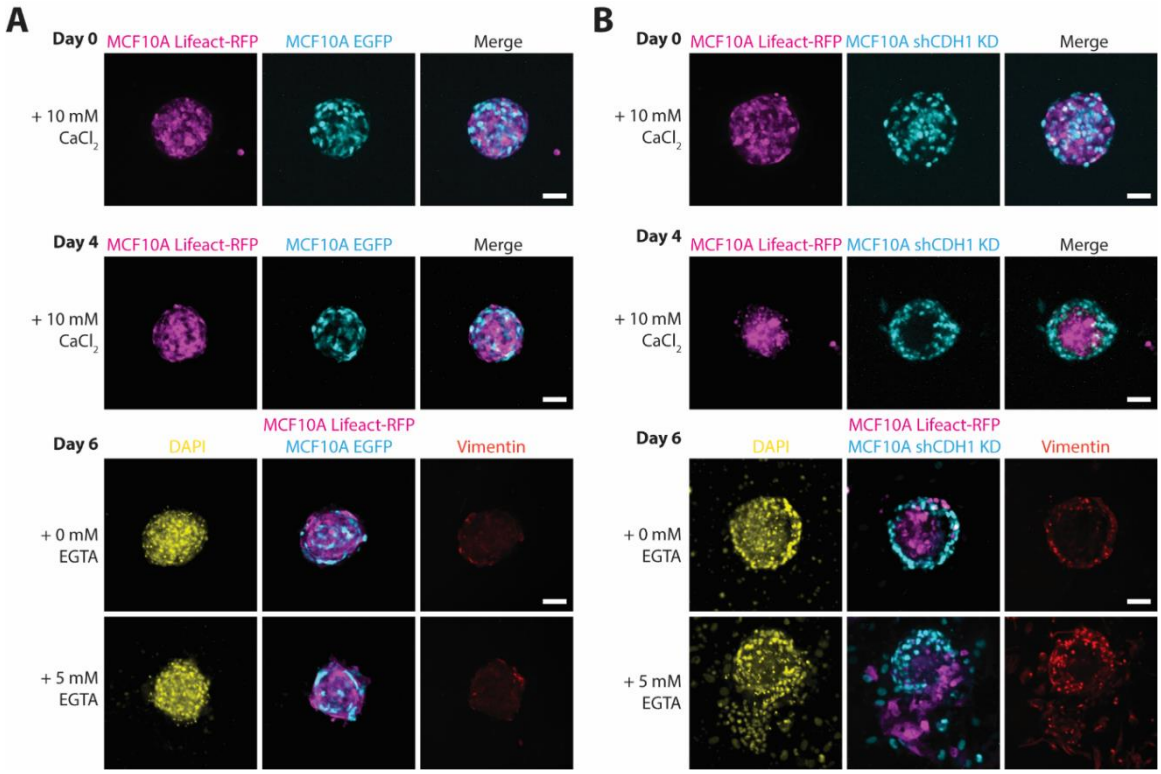

Figure 3.10. Sorted tumor spheroids unjam when matrix stiffness is lowered.

Representative fluorescence images of **(A)** MCF10A EGFP and **(B)** shCDH1 KD spheroids (co-cultured with MCF10A Lifeact-RFP cells) encapsulated in collagen-alginate hydrogels and imaged on day 0 (day of encapsulation), day 4, and day 6 (day of fixation). 0, 5 or 10 mM $CaCl_2$ was added on day 0. On day 4, the spheroids were incubated with 0 or 5 mM EGTA for 1 h, after which the solution was replaced with fresh medium, and the spheroids were cultured until day 6. Spheroids were immunostained for vimentin and stained for DAPI (n = 12 spheroids per condition). Scale bars are 90 μm.

Next, I explored whether lowering matrix stiffness restores single-cell migration in MCF10A Lifeact-RFP and shCDH1 KD spheroids. I hypothesized that reversing the crosslinking reduces the confinement pressure responsible for spheroid sorting and the lack of cell migration into the matrix. Spheroids that were not treated with EGTA maintained a sorted state and were unable to invade. In EGTA-treated spheroids, after matrix stiffness was lowered, MCF10A Lifeact-RFP cells emerged from the spheroid core by rupturing the surrounding shCDH1 KD cell layer

(**Figure 3.10B**). The downregulation of E-cadherin corresponded with the upregulation of the mesenchymal marker vimentin (**Figure 3.10C**), and vimentin expression in wildtype and shCDH1 KD cells was not influenced by confinement conditions (**Figure 3.11**). As a benign epithelial cell line, MCF10A cells express low levels of vimentin (**Figure 3.10**), and as EMT is known to replace the keratin cytoskeleton with vimentin (*72*), the upregulation of vimentin observed in shCDH1 KD cells suggests a partial EMT.

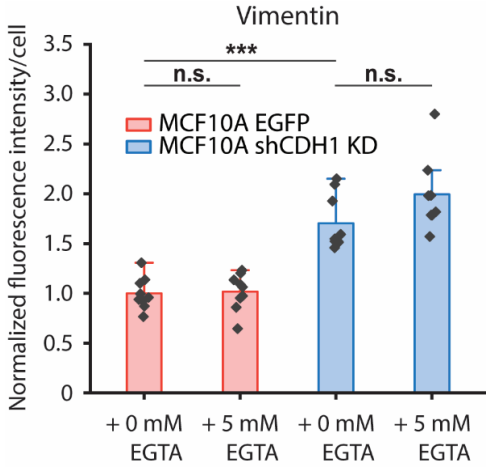

Figure 3.11. Vimentin expression was not influenced by changes in matrix stiffness.

Vimentin fluorescence per cell for MCF10A EGFP or shCDH1 KD cells in co-culture spheroids (with MCF10A Lifeact-RFP cells). On day 0, the spheroids were encapsulated in collagen-alginate hydrogels and 10 mM $CaCl_2$ was added. The samples were subsequently treated with 0 or 5 mM EGTA on day 4 and stained for DAPI and vimentin on day 6. *** $p < 0.001$, n.s. not significant.

3.4.5 Lowering matrix stiffness for sorted spheroids stimulates burst-like migration

To examine the migration of sorted spheroids upon lowering matrix stiffness, I performed timelapse imaging for a 24-h period following EGTA treatment. Thus far, I have analyzed spheroid

compartmentalization at different time scales, however time-lapse sequences are critical to capturing cell speed and trajectories. Since EGTA chelates calcium at a 1:1 ratio, I tested whether complete reversal of alginate crosslinking via the addition of 10 mM EGTA can further promote invasive behavior in co-culture spheroids. I generated two types of mixed spheroids: MCF10A Lifeact-RFP cells co-cultured with MCF10A EGFP or shCDH1 KD cells, and cultured the spheroids as previously described. On day 4, $CaCl_2$ was removed from the medium, and the spheroids were treated with 0 or 10 mM EGTA for 1 h prior to imaging. As expected, wildtype spheroids failed to sort or migrate regardless of EGTA treatment (**Figure 3.12**), whereas untreated mixed shCDH1 KD spheroids remained in a sorted state over the 24-h period (**Figure 3.13A**, top). At the spheroid core, where cell density is high, MCF10A Lifeact-RFP cells were jammed, whereas the surrounding shCDH1 KD cells were in a fluid-like yet confined state where fluctuations were contained by the barrier of high matrix confinement (**Figure 3.13B**, top). In sorted spheroids, EGTA treatment reduced matrix stiffness, resulting in the dissemination of both cell types (**Figure 3.13A and Figure 3.13B**, bottom). Cells that were sorted to the spheroid core rapidly migrated outwards into the matrix with high motility.

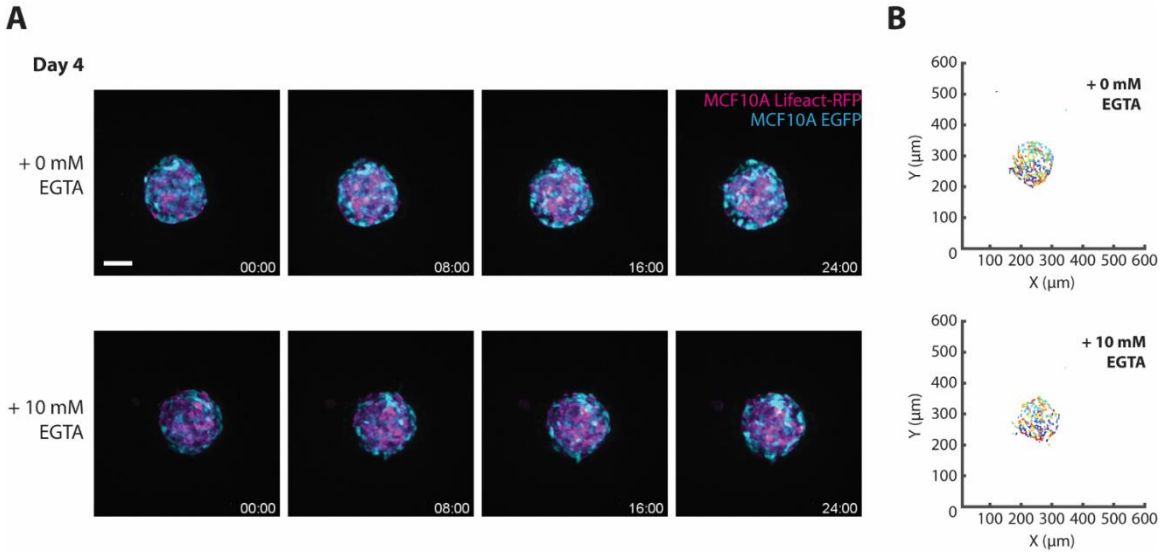

Figure 3.12. Wildtype spheroids do not sort or migrate regardless of EGTA treatment.

Timelapse of MCF10A Lifeact-RFP and EGFP co-culture spheroids over a 24 h period, starting on day 4 after incubation with 0 or 10 mM EGTA for 1 h, after which the solution was replaced with fresh medium prior to time-lapse imaging. **(B)** Corresponding tracked trajectories of MCF10A EGFP cells in spheroids treated with 0 mM EGTA (top) and 10 mM EGTA (bottom). Scale bar: 90 µm.

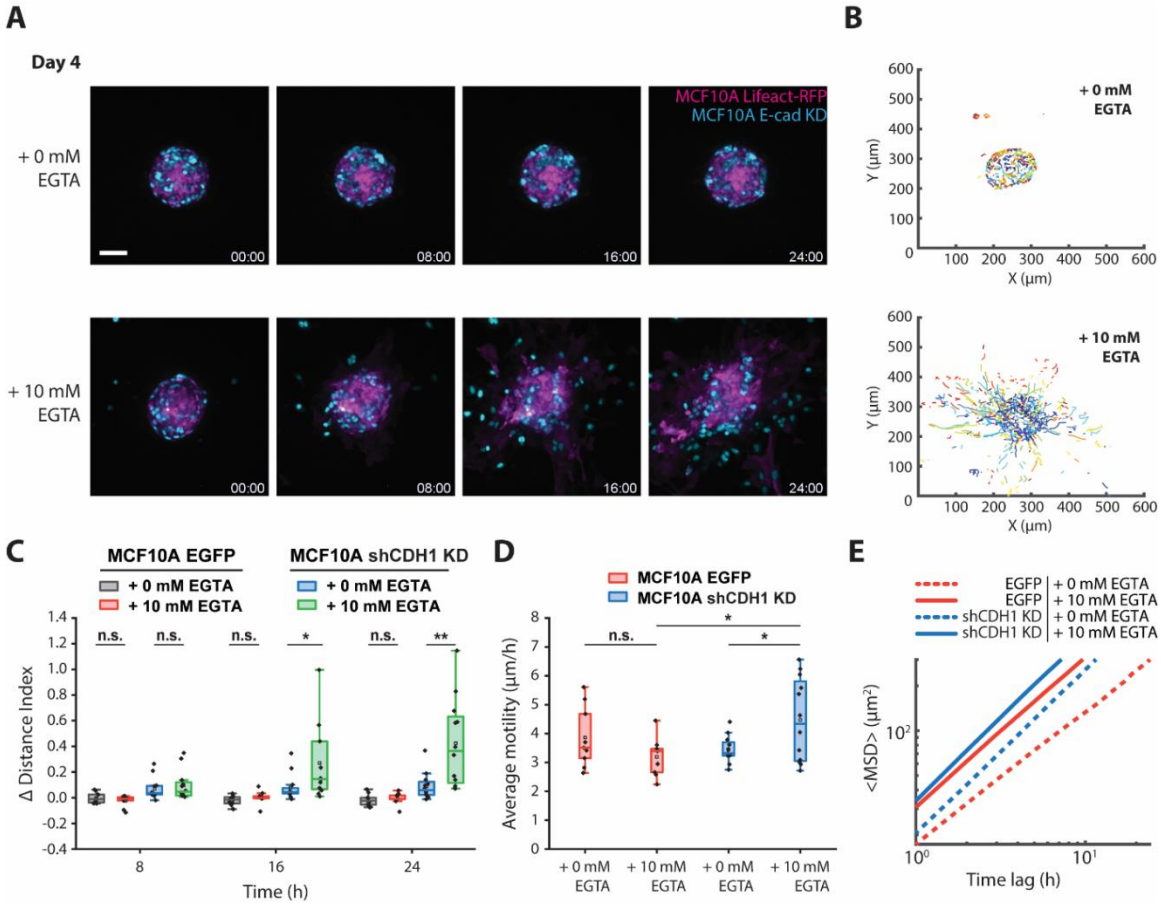

Figure 3.13. The reversal of alginate crosslinking stimulates burst-like migration in sorted spheroids.

(A) Timelapse of MCF10A Lifeact-RFP and shCDH1 co-culture spheroids over a 24-h period, starting on day 4 after incubation with 0 or 10 mM EGTA for 1 h, after which the solution was replaced with fresh medium prior to time-lapse imaging. **(B)** Corresponding tracked trajectories of MCF10A shCDH1 KD cells in spheroids treated with 0 mM EGTA (top) and 10 mM EGTA (bottom). **(C)** Boxplot of distance index for MCF10A EGFP or shCDH1 KD cells in co-culture spheroids (with MCF10A Lifeact-RFP cells) analyzed at 8-hour intervals over 24 h. A positive change in distance index indicates cell motion away from the spheroid core. **(D)** Boxplot of average cell motility for MCF10A EGFP or shCDH1 KD cells (n = 9–12 spheroids per condition). **(E)** MSDs for MCF10A EGFP or shCDH1 KD cells plotted over a 24-h period. Each line represents the mean MSD for n = 12 spheroids. The plots are displayed in log-log scale. Scale bars are 90 µm.

The results presented thus far led us to hypothesize that the jamming—unjamming transition

in 3D can be manipulated by modulating matrix stiffness. To statistically quantify the spatial organization of spheroids over time, I tracked individual MCF10A EGFP or MCF10A shCDH1 KD cells within the two types of mixed spheroids and calculated the change in distance index compared to the initial time point. The average distance travelled by shCDH1 KD cells away from the spheroid core in treated spheroids was significantly higher than in non-treated spheroids (**Figure 3.13C**). Corresponding to the change in distance index (quantified as the difference between the mean distance index of cells for a given spheroid at a specified time point and the cells' initial mean distance index), EGTA treatment triggered and accelerated the migration of shCDH1 KD cells, whereas wildtype MCF10A cell motility was not impacted (**Figure 3.13D**). Computation of the MSD revealed that EGTA treatment increased diffusivity for both cell types, however shCDH1 KD cells were more diffusive than their wildtype counterparts under the same conditions (**Figure 3.13E**).

3.4.6 In theory and experiment, matrix confinement governs spheroid sorting and invasion

In order to understand the impact of matrix confinement on cellular invasion, we utilized a SPV model (*18, 184*), which mimics the dynamics of a heterogeneous tissue comprised of two different types of cells. Our simulations produced a well-sorted tissue, a result of setting differential adhesions parameters (*74, 75*) at cell-cell junctions (**Figure 3.14**). Using the sorted tissue as a starting point, we manipulated the cell-medium contact tensions (τ) to study changes in cell sorting and invasion behaviors.

Figure 3.15A presents representative snapshots illustrating cellular dispersion under conditions of high (left), medium (middle) and low (right) confinement stress (σ_n). These computational results suggest that cells in a well-sorted state manage to breach their boundaries and invade the ECM when confinement is diminished. In order to quantify this cellular dispersion of

cells, we calculated a sorting index, defined as $I = 1 - N_{cluster}/N$, where $N_{cluster}$ is the count of isolated cell clusters and N is the total cell count for each cell type. In instances where the cells are fully sorted, each cell type would form a single cluster, resulting in a sorting index of $I \approx 1$. If the cells are dispersed, they form a mixed state, and each cell forms an isolated cluster unconnected from others, making the sorting index 0. The sorting index I, as a function of σ_n, is shown in **Figure 3.15B**. We can classify the behavior of the cell dispersion into three distinct phases. On the left of the white dashed line, the tissue experiences high confinement. Both A and B cells remain sorted with sorting index $I \approx 1$, corresponding to the left snapshot of **Figure 3.15A** (marked by a star). The middle region, located between the white and black dashed lines, shows that the outer-layered red B cells have dispersed while the A cells stayed sorted, corresponding to the middle snapshot in **Figure 3.15A** (marked by a circle). On the right of the black dashed line, the confinement has essentially vanished. The B cells have completely dispersed, and A cells begin to invade into the ECM, corresponding to the right snapshot in **Figure 3.15A** (marked by a square).

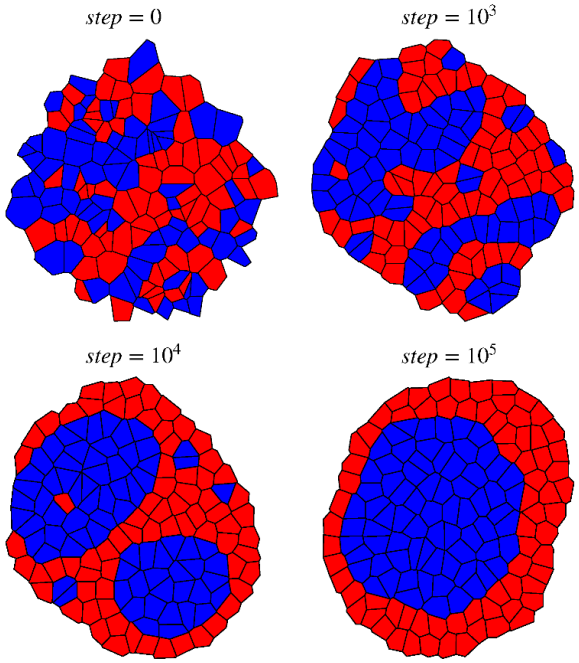

Figure 3.14. Segregation of a heterogeneous tissue with two cell types, blue A cells and red B cells under differential adhesions.

Differential adhesion values are set to be $\tau_{AB} > \frac{\tau_{AA}+\tau_{BB}}{2}$ to achieve a sorted state.

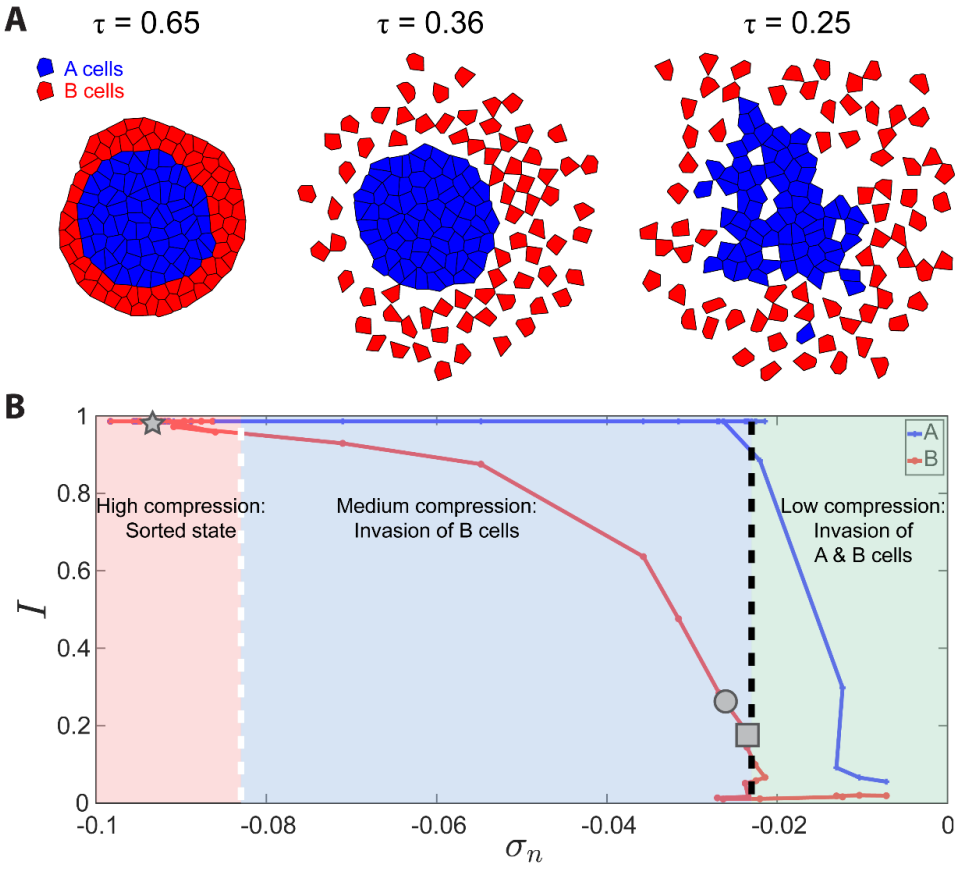

Figure 3.15. SPV simulations portraying a heterogeneous tissue with two cell types, blue A cells and red B cells.

(A) Representative snapshots of cell invasion into the ECM under varying confinement levels. Left: high confinement prevents dispersion. Middle: dispersion of the outer-layered B cells. Right: both A and B cells invade under low confinement. The three snapshots are marked as star, circle, and square in panel **(B)**. **(B)** Cell sorting index *I* is plotted as a function of compressive stress σ_n. By downregulating σ_n, the cells could disperse into the ECM and the sorting index decreases. The dashed white and black lines denote the commencement of dispersion for B and A cells respectively. The invasion behavior bifurcates into three distinct regimes: (1) Red region to the left of the white dashed line indicates high compressive stress and a sorted tissue. (2) Blue region between white and black dashed lines signifies dispersed B cells and sorted A cells. (3) Green region to the right of the black dashed line represents vanishing compressive stress and unsorted A and B cells.

Taken together, our results corroborate a model in which matrix stiffness promotes spheroid sorting in an adhesion-dependent manner and subsequently affects cellular unjamming processes

(**Figure 3.16**). Starting from a mixture of wildtype and shCDH1 KD spheroids encapsulated in collagen-alginate hydrogels, the addition of 10 mM $CaCl_2$ crosslinked the hydrogel, increasing matrix stiffness and confinement, which caused the spheroids to sort. The ability of cells to invade the surrounding matrix hinges on the competition between the forces generated by the cells and the resistance exerted by the matrix. Crosslinking the hydrogel amplifies its yield stress which hinders spheroid volume expansion (*198*). At the spheroid core where cell density is high, the adhesive wildtype cells cannot overcome the solid stress to intercalate positions with neighboring cells, leading to a jammed state (*199*). Conversely, shCDH1 KD cells at the spheroid boundary are not jammed, however the cells do not have sufficient energy to escape their compartment boundary. By reversing the crosslinking, the resistance to cell motion is removed, and the cells flow in an unjamming transition, reminiscent of the release of solid stress and elastic energy when the mechanical confining structure of an excised tumor is disrupted (*200*). 5 mM EGTA treatment partially reversed the crosslinking and correspondingly reduced ECM confinement. As a result, the compacted wildtype cells escaped from the spheroid core as a strand and broke through the surrounding layers of shCDH1 KD cells. When the crosslinking was completely reversed by the addition of 10 mM EGTA, the cells displayed collective and super-diffusive motion as they were pushed into the matrix with high velocity.

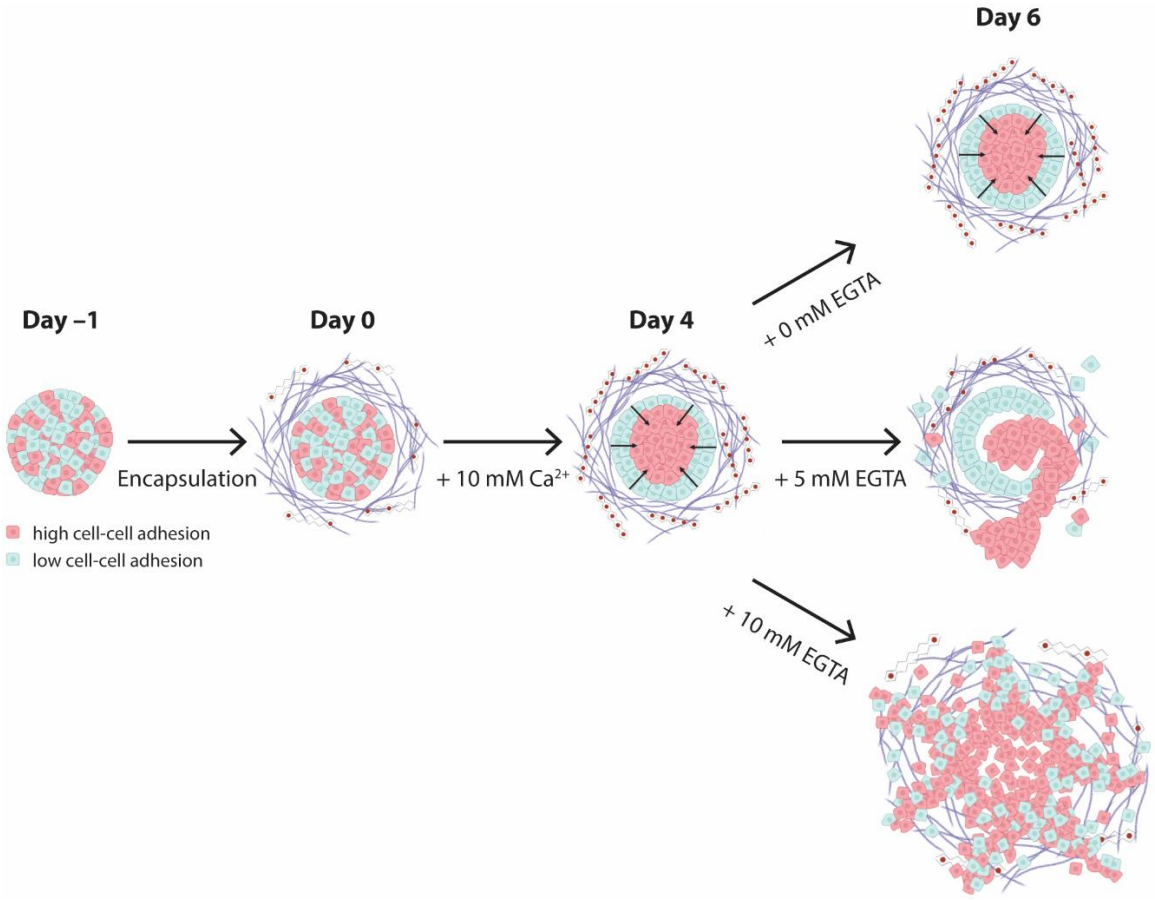

Figure 3.16. Tumor spheroid sorting and burst-like migration in a composite hydrogel with tunable stiffness.

Summary depicting a spheroid generated from a mixture of cells with high cell-cell adhesion (red) and cells with low cell-cell adhesion (blue) on day –1, encapsulation of the spheroid in a collagen-alginate hydrogel on day 0 and sorting under high-confinement ECM on day 4. The rightmost panel depicts, on day 6, the spheroid sustaining the sorted state after 0 mM EGTA treatment (top), a strand-like cluster emerging from the spheroid core after 5 mM EGTA treatment (middle) and burst-like unjamming after 10 mM EGTA treatment (bottom).

3.5 Discussion

In the present study, I show that tuning matrix stiffness regulates 3D spheroid sorting and collective cell migration into the ECM. ECM stiffness is known to play a significant role in cancer spread and metastasis in the body (*100, 201, 202*), and I first establish that single-cell cancer

migration is restricted by matrix stiffness in collagen-alginate hydrogels, where collagen provides cell adhesion sites and alginate limits degradation by MMPs. I then demonstrate the sorting of non-invasive cancer cells and normal breast epithelial cells in co-culture spheroids. The DAH assumes that sorting is a result of cells rearranging to minimize interfacial tension, which is directly proportional to differences in cell-cell adhesion (*11*, *72*, *74*), and as a result, spheroid sorting achieves an equilibrium thermodynamic state (*74*). In hydrogels with minimal crosslinking, sorting does not occur, and the spheroid size increases after 4 days of culture as cells proliferate. However, in response to high matrix confinement, spheroids exhibit sorting behavior, and the pressure inside the spheroids increase. In monoculture spheroids of benign breast epithelial cells, E-cadherin expression is reduced in response to high matrix stiffness, suggesting that in the absence of mesenchymal cells to induce sorting and secrete enzymes to remodel the matrix, normal cells undergo a partial EMT to promote cell invasion (*203*). Normal cells adapt to confined conditions by adjusting the properties of the cellular collective, however an undegradable hydrogel with low available ECM space presents a barrier that the cells are unable to overcome.

By crosslinking the hydrogel, the barrier to cell motion into the matrix is high, and the cells become jammed from the increased solid stress resulting from spheroid sorting. Stably downregulating E-cadherin identifies differences in intercellular adhesion as the primary driver of cell sorting and jamming. Spheroid sorting generates high local cell density in the core, where cells strengthen cell-cell adhesions, reduce cell volume, and exhibit jammed behavior. In this jammed state, cells are constrained by adhesion and the tension along cell-cell interfaces increases (*9*, *11*, *17*). One open question is how stress fluctuations driven by nearby cell division impact cell motility and structural rearrangements in the dense spheroid core (*11*). Core cells require energy to escape the boundary constraints imposed by their neighbors and the surrounding matrix. Less adhesive

mesenchymal cells are relegated to the outer edges of the spheroid and exist in an unjammed state, where the cells can rearrange within the compartment boundary. Cell sorting, which requires cell-cell adhesions, leads to a buildup of pressure within the spheroid, and reducing matrix stiffness results in a pressure difference between the spheroid and the surrounding matrix. Burst-like cellular motion was recorded in soft collagen matrices (0.5 mg/ml) and attributed to the pressure increase within the cancer aggregate due to cell swelling (*79*). In this study, I provide evidence that manipulating matrix stiffness directly impacts 3D spheroid sorting, as well as individual and collective cell invasion. In comparison to single-cell cancer migration, pressure-driven burst-like migration provides an outlet for cells confined by the spheroid boundary, and tumor cells can rapidly escape into the surrounding matrix.

Our findings present a composite hydrogel with mechanically tunable properties while maintaining a constant collagen concentration. Hydrogel stiffness is modified by the crosslinking of sodium alginate into calcium alginate and the reversal of crosslinking via the calcium chelator EGTA. In tumor development, cancer cells are confined by compartment boundaries until a late stage (*72*, *204*). Primary tumors are encapsulated and confined by a basement membrane, and as the tumor cells proliferate, the tumor experiences high confinement stress and is driven to sort according to the DAH. In a degradable matrix, the highly proliferative cancer cells sorted to the spheroid boundary secrete MMPs to remodel the surrounding matrix, reducing ECM confinement. This decrease in confinement can instigate an unjamming transition, leading to a rapid spread of tumor cells. Our work presents new insights into the impact of matrix mechanical properties on the mechanisms of collective cell motion in the primary tumor and cancer migration towards distant metastatic sites as individual cells and as cellular aggregates.

Chapter 4 Conclusions and Future Perspectives

4.1. Overview

In this dissertation, I have demonstrated that adhesion-dependent cellular responses to mechanical compression play an important role in collective cell motion and jamming transitions in 2D monolayers and 3D spheroids. In Chapter 2, I found that the compression-induced unjamming transition in an epithelial monolayer of cancer cells is distinct from EMT and is mediated by cell shape changes linked to strengthened cell-cell adhesions. Further, I showed that compressive stress accelerates the collective cell migration of breast cancer 4T1 cells via cell elongation and increased E-cadherin-mediated cell-cell adhesions. In Chapter 3, I utilized a 3D spheroid model to demonstrate that physical confinement in a collagen-alginate composite hydrogel directly impacts cell sorting and invasion in mixed spheroids. In a spheroid comprised of two cell types with differences in adhesiveness, increased matrix stiffness promotes cell sorting and results in pressure accumulation within the spheroid core. When matrix confinement is lowered, the cells exhibit burst-like migration, rapidly escaping from the confines of the spheroid. However, many unanswered questions remain about the parameters governing unjamming transitions in epithelial tissues and primary tumors, including the role of pressure-driven burst-like migration within tumors in vivo, the incorporation of different cell types and types of soft hydrogel materials to replicate the complex tumor microenvironment, and the role of mechanosensitive channels in regulating cell migration in response to mechanical stimuli. Throughout this conclusion chapter, I will discuss potential future directions of my findings.

4.2. Chapter 2 summary and future directions

Prior to my work, computational studies defined a critical cell shape index that marks the jamming threshold (*18, 35*). By elongating their shapes, cells can overcome the constraints of high cell density to gain motility while maintaining epithelial characteristics in a transition distinct from EMT. However, the cell-cell adhesions and cell-substrate forces that generate this preferred cell shape are not as easily quantified. In Chapter 2, I discovered that, in breast cancer 4T1 cells, focal adhesions largely disassembled at regions of cell-cell contacts in response to mechanical load while E-cadherin localization at intercellular adhesion sites increased. Despite this, traction stresses were sustained at the free cell edge. As a result, cells within the bulk cell layer presented lower traction forces and higher cell-cell adhesions under compression, allowing for highly fluid-like migration where the bulk cells were more easily pulled by the cells at the leading edge during wound healing.

4.2.1. Regulation of mechanosensitive ion channels in cell migration

In contrast to granular systems, which can withstand high compressive stresses but cannot support tensile stress (*3*), the mechanical stress in a confluent cell layer is predominantly tensile (*122*). Tensile stretch, which impacts cell shape, enhances invadopodia formation, and triggers motility pathways, can predispose tumor cells to invasive behaviors, transmigration, and jamming transitions (*64*).

Cells encounter tensile stretch as they navigate through constrained spaces, such as narrow channels and dense ECM environments (*64*). During invasion through the ECM and processes such as intravasation and extravasation, migrating cells experience compression due to constricted pathways (*95, 205*). In response to these physical limitations, cells generate forces to deform their

shapes to squeeze through narrow passages, enabling migration within confined 3D regions. Jamming transitions during 3D confined migration offers insights into the mechanisms through which cells can become trapped during migration in the primary tumor or in attempts to invade into the ECM (*20, 50*). As cells navigate tight spaces within the dense ECM, they encounter increased mechanical resistance. Cell motion can be hindered if the mechanical forces exerted by the cells exceed a certain threshold, and the cells can become immobilized, impeding migration (*99*).

Mechanical stimuli have been shown to reshape epithelial cell-cell junctions through the elongation and contraction of junctions via mechanosensitive channels (*153*), however the precise molecular mechanisms that translate mechanical cues into changes in invasive behavior remain poorly understood. Earlier work from our lab revealed that the exogenous expression of the mechanosensitive channel of large conductance (MscL) in cancer cells inhibits cell entry into narrow 3D channels (*205*). Another mechanosensitive channel of particular interest is Piezo1, which has recently been shown to bind to E-cadherin and modulate membrane trafficking.

Piezo1 regulates cell migration in response to various mechanical stimuli and mediates cell motility in both individual and collective migration (*206–209*). In Dictyostelium amoebae migration, Piezo1 facilitates cell movement under compressive stress by switching from F-actin–driven pseudopods to bleb-driven motility (*210*). Moreover, previous work from our lab demonstrated that mechanical compression activates Piezo1, leading to enhanced matrix degradation, actin protrusion formation, and an influx of calcium ions (*128*).

Given that Piezo channels are tethered to the actin cytoskeleton through the cadherin-β-catenin complex (*211*), Piezo1 and E-cadherin may work together to transmit adhesion-cytoskeleton forces. A compelling aspect is the potential involvement of Piezo1 mechanotransduction in the regulation of E-cadherin expression due to the role of Piezo1 in transducing mechanical forces

applied externally and internally at the plasma membrane (*208*). As a result, the influence of mechanosensitive channels potentially extends to governing E-cadherin turnover, thereby linking mechanotransduction and cellular adhesion dynamics.

4.3. Chapter 3 summary and future directions

Primary tumors are encapsulated within a basement membrane and are subject to increased confinement stress as they grow, leading to a buildup of internal pressure driven by cell proliferation (*166*). This mounting pressure can give rise to the rupture of the basement membrane, either by mechanical tension or through active degradation by cancer cells. As individual cancer cells navigate the rigid surrounding matrix and the basement membrane, they encounter constraints such as the dense ECM and physical obstacles, resulting in slow and inefficient migration.

Clinical studies have demonstrated that reduced E-cadherin expression within metastatic breast tumors in mice triggers detachment at the single-cell level yet is not sufficient to enhance distant metastasis (*50*). However, cell sorting provides cancer cells with an efficient way of relocating towards the tumor periphery. At the tumor boundary, cancer cells gain greater access to essential nutrients and secrete MMPs to remodel the surrounding matrix, increasing their potential for invasion and dissemination.

In Chapter 3, I found that cells rearrange within spheroids according to the differential adhesion hypothesis in response to increased physical confinement, causing a buildup of pressure within the spheroid. Tumor cell sorting can generate increased pressure within the solid tumor mass, and upon a reduction in physical confinement due to degradation of the ECM, this accumulation of pressure can effectively propel the cancer cells at the tumor periphery away from the primary tumor

site with high velocity.

High pressure within the spheroid can result in a spontaneous burst-like motility of tumor cells that effectively disrupts the cell arrest that typifies high cell density within the spheroid core (*79*). This burst-like migration, driven by the pressure difference between the spheroid and the degraded ECM, allows cancer cells to gain access to distant sites of metastasis. Burst-like migration occurs mostly in the form of cellular aggregates, rather than individual cells, increasing the potential for micrometastasis (*79*). This involves tumor cell clusters travelling to distant sites within the body where they establish small secondary tumors.

4.3.1. Sorting of tumor cells based on stiffness

It is well-known that many tumors are rigid masses that are significantly stiffer than their surrounding tissue (*197, 212*). Breast tumors are typically composed of cancer cell clusters ensconced within a stiff stromal environment characterized by an excessive deposition of ECM – a strong tumor promoter (*94*). Interestingly, soft cancer cells, which have been shown to be softer than normal epithelial cells, reside within rigid tumors (*76, 160*).

Primary tumors, from the scale of tissues to individual cells, possess high mechanical heterogeneity (*213, 214*). A wide range of cell stiffness exists in tumors, ranging from very stiff cells to cells softer than those found in healthy tissue (*76*). Notably, tumors tend to harbor a larger fraction of softer cancer cells, which are more likely to undergo pronounced shifts in membrane tension and are more susceptible to deformation under a given compressive stress. This can yield reduced endocytosis and turnover of membrane proteins (*157*). Due to their increased deformability, cancer cells are more motile and can navigate past one another more easily, resulting in jammed islands of rigid cells surrounded by fluid-like streams of soft, motile cells.

Cell stiffness has been linked to E-cadherin turnover (*158, 159*), where the effect of cell mechanics on membrane trafficking potentially contributes to fluctuations in cell surface E-cadherin levels within epithelial monolayers and 3D aggregates in response to mechanical stimuli. Intriguingly, applying mechanical load can engender disparate responses across cells of varying stiffness, even within the confines of the same tissue or tumor (*99*). As a result, fluidization of certain regions can occur while other areas of the collective remain solid-like.

Within tumors, cells of similar stiffness tend to congregate, giving rise to distinctive mechanical niches marked by clusters of stiff cells enveloped by softer cells (*76, 215*). These clusters of rigid cells within tumors contribute to tumor heterogeneity and the process of cell sorting. Cell sorting based on stiffness can influence the metastatic potential of tumor cells since softer cancer cells may be more adept at invading the ECM. Furthermore, the inherent resistance of stiffer cells to mechanical forces could potentially drive the selective migration of softer cancer cells.

The downregulation of keratin following EMT contributes to cell softening (*216*), which allows cells to migrate more efficiently through dense ECM, up until the size of the nucleus becomes an inhibiting factor (*144*). Beyond this, cancer cell softening can trigger cell unjamming, thus promoting a collective motility transition in cancer cell clusters within tumors, thereby contributing to metastatic progression.

I propose utilizing micropipette aspiration to apply suction forces to 3D co-culture spheroids, aiming to measure the deformability of the spheroid structure. This approach allows us to investigate the mechanical properties of the spheroid, offering insights into potential mechanical heterogeneity arising from interactions among various cell types and ECM gradients. The results will shed light on the deformability and mechanical properties of cell spheroids and their impact on cell migration and behavior. Nonetheless, because the micropipette aspiration technique primarily

targets cells on the spheroid's surface, it is essential to explore alternative methods for sampling cells within the interior of a 3D spheroid.

4.3.2. Cell swelling increases pressure within tumors

Micropipette aspiration experiments offer insights into individual and collective cell behaviors within spheroids, including phenomena such as cell swelling (*217*). Cell swelling can be attributed to various factors, including shifts in ion concentrations, osmotic imbalances, and changes in membrane permeability (*218*). Generally, swelling tends to impede the migration of tumor cells through narrow spaces, as swollen cells encounter difficulties in navigating tight passages. However, cell swelling has recently been observed to precede burst-like migration in 3D cellular aggregates (*79*). Swelling results in heightened tension within the cell membrane, is linked to changes in cell shape, and affects the alignment and coordination of migrating cell clusters (*79, 218, 219*). Given that the volume of cellular aggregates is influenced by confinement stress, changes in cell volume, such as swelling, contributes to fluctuations in pressure within the aggregates.

While increased collagen density induces local cell individualization (*50*), lower collagen concentration leads to cell swelling and death (*79*). Moreover, the latter triggers bursts of cells to stream out of the cellular aggregate in the direction of least mechanical resistance. While there is evidence that swelling relies on cell-ECM adhesion and cell contractility and is associated with an increase in pressure within aggregates (*79*), little is known about its role in cancer progression.

4.3.3. Extracellular fluid viscosity affects spheroid fusion

Migrating cells within the tumor microenvironment encounter physical cues that induce cell swelling and alterations in membrane tension, including ECM stiffness, fluid shear stress, interstitial fluid pressure, and fluid viscosity (*45, 219–221*). While most in vitro cell assays use

medium with a viscosity close to water (0.7 cP), the interstitial fluid's viscosity varies up to 3.5 cP (*219*). Intriguingly, recent research reveals that increased viscosity enhances cell motility on 2D surfaces, in confinement, and facilitates cell dissemination from tumor spheroids (*219*). Elevated viscosity is found to trigger actin-based ARP2/3 complex-dependent networks, enhancing NHE1 polarization through ezrin. Consequently, cell swelling occurs, raising membrane tension, activating TRPV4, inducing calcium influx, and heightening RHOA-dependent contractility. The combined events of actin remodeling, NHE1 swelling, and RHOA contractility increase cell motility in high-viscosity settings (*219*).

I propose conducting a spheroid fusion assay under elevated viscosity conditions to investigate cell motility and cell-cell interactions. Viscosity might hinder spheroid fusion by altering cell-cell adhesions, affecting the capacity of cells to adhere and connect. Spheroid fusion necessitates alterations in cell shape and membrane dynamics, which extracellular fluid viscosity can influence. Preliminary experiments reveal that spheroids comprised of normal breast epithelial cells fuse at the interface between the individual spheroids, while non-metastatic breast cancer spheroids exhibit strong super-diffusivity (**Figure 4.1**).

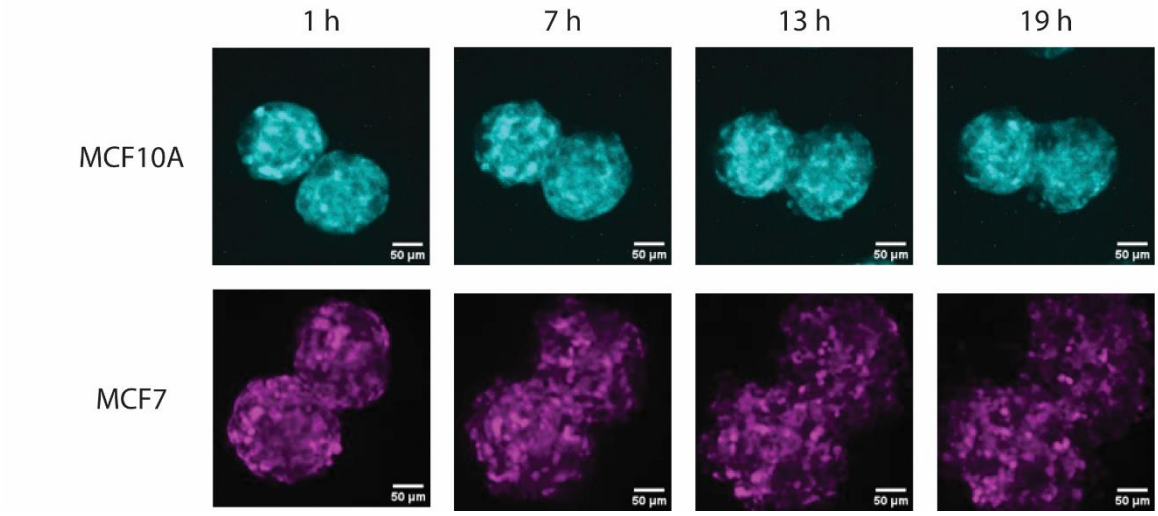

Figure 4.1. Spheroid fusion in high-viscosity medium.

Spheroids comprised of MCF10A EGFP (top) or MCF7 Lifeact-RFP (bottom) cells fuse and exhibit varying degrees of tissue fluidity in high-viscosity medium (8 cP). The cancer cell spheroids behave more fluid-like than the non-tumorigenic epithelial spheroids.

4.3.4. Measuring mechanical stress in tissues and tumors

Plasma membrane tension is a global mechanical regulator that coordinates diverse cellular processes, from the processes of endocytosis and exocytosis to actin filament polymerization and cytoskeleton-mediated force transmission (*222, 223*). Employing a membrane tension sensor to measure tension along cell-cell interfaces within various regions of tissue and cellular aggregates would elucidate how different tumor areas respond to mechanical input and microenvironmental forces. Local variations in membrane tension play a role in sub-cellular processes, impacting cell shape, migration, and membrane trafficking (*223*). By detecting force discrepancies across a cell layer, a membrane tension sensor pinpoints variations in response to mechanical stresses, particularly as cells within the tissue strive to minimize these stresses. Such sensor utilization could clarify how mechanical cues such as matrix stiffness influence cell behavior and provide insight

into pressure buildup in different regions of multicellular spheroids.

One approach involves utilizing an optical membrane tension sensor developed in our lab by repurposing MscL via insertion of circularly permuted GFP (cpGFP) to generate an OFF sensor (*224*). This alters the fluorescence intensity of the MscL tension reporter based on the mechanical tension sensed by the cell. Analyzing fluorescence intensity changes quantifies membrane tension, providing insights into how stiffness gradients within tumors influence cell-cell interactions and invasive behavior. Additionally, in tumors, mechanical compression tends to exacerbate heterogeneities in cell-cell and cell-ECM adhesions (*41, 190*). A membrane tension sensor could help unravel how these factors influence cell behavior. In such instances, cells might cluster differently, move independently from their neighbors, or break free from the cellular collective.

4.3.5. A multi-modal bioreactor to apply physical stimuli to hydrogel-encapsulated 3D spheroids

In this dissertation, I investigate the impact of physical confinement on tumor spheroid sorting and migration through the modulation of chemical crosslinking in the matrix environment. Although tumor spheroids undergo confinement stress, changing the matrix stiffness alone does not sufficiently capture the complex and dynamical mechanical loading present in vivo (*56*).

To address this, developing a device that applies compression, fluid shear, and stretch in a coordinated manner can offer a more physiologically comprehensive approach to replicating the mechanical forces present in vivo in 3D tumor models. A potential design involves a multi-modal bioreactor capable of generating controlled and dynamic mechanical forces. This can include the integration of microfluidic channels for regulating fluid shear stress, plates for applying compressive forces, and motors for inducing strain. In addition, biocompatible materials could be

integrated to mimic in vivo conditions. The concept involves polymerizing hydrogel-encapsulated 3D spheroids within the device. This results in the hydrogel adhering to collagen-coated polydimethylsiloxane chambers, thereby allowing the application of compressive and tensile forces. Additionally, fluid shear can be achieved through microchannels that flow between the chambers. The results have the potential to shed light on how mechanical forces influence cell behavior and tissue development. Furthermore, this approach could subject engineered constructs to physiologically relevant mechanical forces, thereby enhancing tissue maturation, alignment, and overall function.

4.4. Conclusions

In this dissertation, I illustrate the direct influence of changes in compressive and confinement stresses on collective cell motion in 2D monolayer and 3D spheroid models. Cell jamming is often used to describe the transition from migratory to resting cell states during collective migration. Together with recent work from other groups, the contents of this thesis highlight how mechanical stress on cells can regulate unjamming transitions in cell monolayers and multicellular spheroids. The observed burst-like migration in heterogeneous spheroids arises from heightened pressure within the spheroid core, which is a result of cell sorting driven by differences in cell adhesiveness.

Understanding how mechanical input and forces from the tumor microenvironment influence cell behavior and migration patterns in 2D and 3D contexts remains an important question in mechanobiology. It becomes apparent that our knowledge of forces and force generation excludes unprecedented mechanisms that drive collective cell behavior and motion in the field of tumor biophysics.

Bibliography

1. A. J. Liu, S. R. Nagel, Jamming is not just cool any more. *Nature*. **396** (1998), pp. 21–22.
2. J. Zhang, T. S. Majmudar, M. Sperl, R. P. Behringer, Jamming for a 2D granular material. *Soft Matter*. **6**, 2982–2991 (2010).
3. R. P. Behringer, Jamming in granular materials. *C R Phys*. **16**, 10–25 (2015).
4. R. P. Behringer, B. Chakraborty, The physics of jamming for granular materials: a review. *Reports on Progress in Physics*. **82**, 012601 (2018).
5. V. Trappe, V. Prasad, L. Cipelletti, P. N. Segre, D. A. Weitz, Jamming phase diagram for attractive particles. *Nature 2001 411:6839*. **411**, 772–775 (2001).
6. P. Das, H. A. Vinutha, S. Sastry, Unified phase diagram of reversible–irreversible, jamming, and yielding transitions in cyclically sheared soft-sphere packings. *Proc Natl Acad Sci U S A*. **117**, 10203–10209 (2020).
7. M. P. Ciamarra, M. Nicodemi, A. Coniglio, Recent results on the jamming phase diagram. *Soft Matter*. **6**, 2871–2874 (2010).
8. E. Brown, N. Rodenberg, J. Amend, A. Mozeika, E. Steltz, M. R. Zakin, H. Lipson, H. M. Jaeger, Universal robotic gripper based on the jamming of granular material. *Proc Natl Acad Sci U S A*. **107**, 18809–18814 (2010).
9. S. Garcia, E. Hannezo, J. Elgeti, J. F. Joanny, P. Silberzan, N. S. Gov, Physics of active jamming during collective cellular motion in a monolayer. *Proc Natl Acad Sci U S A*. **112**, 15314–15319 (2015).
10. W. Kang, J. Ferruzzi, C. P. Spatarelu, Y. L. Han, Y. Sharma, S. A. Koehler, J. A. Mitchel, A.

Khan, J. P. Butler, D. Roblyer, M. H. Zaman, J. A. Park, M. Guo, Z. Chen, A. F. Pegoraro, J. J. Fredberg, A novel jamming phase diagram links tumor invasion to non-equilibrium phase separation. *iScience*. **24**, 103252 (2021).

11. E. Lawson-Keister, M. L. Manning, Jamming and arrest of cell motion in biological tissues. *Curr Opin Cell Biol*. **72**, 146–155 (2021).
12. E. Blauth, H. Kubitschke, P. Gottheil, S. Grosser, J. A. Käs, Jamming in Embryogenesis and Cancer Progression. *Front Phys*. **9**, 445 (2021).
13. R. Alert, X. Trepat, Physical Models of Collective Cell Migration. *https://doi.org/10.1146/annurev-conmatphys-031218-013516*. **11**, 77–101 (2020).
14. P. Rørth, Collective cell migration. *Annu Rev Cell Dev Biol*. **25**, 407–429 (2009).
15. A. Shellard, R. Mayor, Rules of collective migration: from the wildebeest to the neural crest. *Philosophical Transactions of the Royal Society B*. **375** (2020), doi:10.1098/RSTB.2019.0387.
16. M. Sadati, N. Taheri Qazvini, R. Krishnan, C. Y. Park, J. J. Fredberg, Collective migration and cell jamming. *Differentiation*. **86**, 121–125 (2013).
17. L. Atia, D. Bi, Y. Sharma, J. A. Mitchel, B. Gweon, S. A. Koehler, S. J. Decamp, B. Lan, J. H. Kim, R. Hirsch, A. F. Pegoraro, K. H. Lee, J. R. Starr, D. A. Weitz, A. C. Martin, J. A. Park, J. P. Butler, J. J. Fredberg, Geometric constraints during epithelial jamming. *Nature Physics 2018 14:6*. **14**, 613–620 (2018).
18. D. Bi, X. Yang, M. C. Marchetti, M. L. Manning, Motility-driven glass and jamming transitions in biological tissues. *Phys Rev X*. **6**, 021011 (2016).
19. L. Oswald, S. Grosser, D. M. Smith, J. A. Käs, Jamming transitions in cancer. *J Phys D Appl Phys*. **50**, 483001 (2017).

20. A. Haeger, M. Krause, K. Wolf, P. Friedl, Cell jamming: Collective invasion of mesenchymal tumor cells imposed by tissue confinement. *Biochimica et Biophysica Acta (BBA) - General Subjects*. **1840**, 2386–2395 (2014).

21. K. J. Cheung, V. Padmanaban, V. Silvestri, K. Schipper, J. D. Cohen, A. N. Fairchild, M. A. Gorin, J. E. Verdone, K. J. Pienta, J. S. Bader, A. J. Ewald, Polyclonal breast cancer metastases arise from collective dissemination of keratin 14-expressing tumor cell clusters. *Proc Natl Acad Sci U S A*. **113**, E854–E863 (2016).

22. J. Fares, M. Y. Fares, H. H. Khachfe, H. A. Salhab, Y. Fares, Molecular principles of metastasis: a hallmark of cancer revisited. *Signal Transduct Target Ther*. **5** (2020), doi:10.1038/S41392-020-0134-X.

23. Z. Zhao, A. Ukidve, J. Kim, S. Mitragotri, Targeting Strategies for Tissue-Specific Drug Delivery. *Cell*. **181**, 151–167 (2020).

24. P. Friedl, J. Locker, E. Sahai, J. E. Segall, Classifying collective cancer cell invasion. *Nature Cell Biology 2012 14:8*. **14**, 777–783 (2012).

25. J. A. Park, L. Atia, J. A. Mitchel, J. J. Fredberg, J. P. Butler, Collective migration and cell jamming in asthma, cancer and development. *J Cell Sci*. **129**, 3375–3383 (2016).

26. L. Atia, J. J. Fredberg, N. S. Gov, A. F. Pegoraro, Are cell jamming and unjamming essential in tissue development? *Cells & Development*. **168**, 203727 (2021).

27. K. D. Nnetu, M. Knorr, J. Käs, M. Zink, The impact of jamming on boundaries of collectively moving weak-interacting cells. *New J Phys*. **14** (2012), doi:10.1088/1367-2630/14/11/115012.

28. P. Friedl, D. Gilmour, Collective cell migration in morphogenesis, regeneration and cancer. *Nat Rev Mol Cell Biol*. **10** (2009), pp. 445–457.

29. K. Campbell, J. Casanova, A common framework for EMT and collective cell migration.

Development. **143**, 4291–4300 (2016).

30. X. Trepat, M. R. Wasserman, T. E. Angelini, E. Millet, D. A. Weitz, J. P. Butler, J. J. Fredberg, Physical forces during collective cell migration. *Nature Physics 2009 5:6*. **5**, 426–430 (2009).

31. X. Trepat, E. Sahai, Mesoscale physical principles of collective cell organization. *Nature Physics 2018 14:7*. **14**, 671–682 (2018).

32. O. Chepizhko, M. C. Lionetti, C. Malinverno, C. Giampietro, G. Scita, S. Zapperi, C. A. M. La Porta, From jamming to collective cell migration through a boundary induced transition. *Soft Matter*. **14**, 3774–3782 (2018).

33. D. Bi, J. H. Lopez, J. M. Schwarz, M. L. Manning, A density-independent rigidity transition in biological tissues. *Nat Phys*. **11**, 1074–1079 (2015).

34. X. Yang, D. Bi, M. Czajkowski, M. Merkel, M. L. Manning, M. C. Marchetti, Correlating cell shape and cellular stress in motile confluent tissues. *Proc Natl Acad Sci U S A*. **114**, 12663–12668 (2017).

35. J. A. Park, J. H. Kim, D. Bi, J. A. Mitchel, N. T. Qazvini, K. Tantisira, C. Y. Park, M. McGill, S. H. Kim, B. Gweon, J. Notbohm, R. Steward, S. Burger, S. H. Randell, A. T. Kho, D. T. Tambe, C. Hardin, S. A. Shore, E. Israel, D. A. Weitz, D. J. Tschumperlin, E. P. Henske, S. T. Weiss, M. L. Manning, J. P. Butler, J. M. Drazen, J. J. Fredberg, Unjamming and cell shape in the asthmatic airway epithelium. *Nat Mater*. **14**, 1040 (2015).

36. D. Bi, J. H. Lopez, J. M. Schwarz, M. Lisa Manning, Energy barriers and cell migration in densely packed tissues. *Soft Matter*. **10**, 1885–1890 (2014).

37. D. T. Tambe, C. Corey Hardin, T. E. Angelini, K. Rajendran, C. Y. Park, X. Serra-Picamal, E. H. Zhou, M. H. Zaman, J. P. Butler, D. A. Weitz, J. J. Fredberg, X. Trepat, Collective cell

guidance by cooperative intercellular forces. *Nature Materials 2011 10:6*. **10**, 469–475 (2011).

38. P. Friedl, R. Mayor, Tuning Collective Cell Migration by Cell–Cell Junction Regulation. *Cold Spring Harb Perspect Biol*. **9**, a029199 (2017).

39. M. Poujade, E. Grasland-Mongrain, A. Hertzog, J. Jouanneau, P. Chavrier, B. Ladoux, A. Buguin, P. Silberzan, Collective migration of an epithelial monolayer in response to a model wound. *Proc Natl Acad Sci U S A*. **104**, 15988–15993 (2007).

40. A. Palamidessi, C. Malinverno, E. Frittoli, S. Corallino, E. Barbieri, S. Sigismund, G. V. Beznoussenko, E. Martini, M. Garre, I. Ferrara, C. Tripodo, F. Ascione, E. A. Cavalcanti-Adam, Q. Li, P. P. Di Fiore, D. Parazzoli, F. Giavazzi, R. Cerbino, G. Scita, Unjamming overcomes kinetic and proliferation arrest in terminally differentiated cells and promotes collective motility of carcinoma. *Nature Materials 2019 18:11*. **18**, 1252–1263 (2019).

41. G. Cai, A. Nguyen, Y. Bashirzadeh, S.-S. Lin, D. Bi, A. P. Liu, Compressive stress drives adhesion-dependent unjamming transitions in breast cancer cell migration. *Front Cell Dev Biol*. **0**, 1983 (2022).

42. J. H. Kim, A. F. Pegoraro, A. Das, S. A. Koehler, S. A. Ujwary, B. Lan, J. A. Mitchel, L. Atia, S. He, K. Wang, D. Bi, M. H. Zaman, J. A. Park, J. P. Butler, K. H. Lee, J. R. Starr, J. J. Fredberg, Unjamming and collective migration in MCF10A breast cancer cell lines. *Biochem Biophys Res Commun*. **521**, 706–715 (2020).

43. H. Yamaguchi, J. Wyckoff, J. Condeelis, Cell migration in tumors. *Curr Opin Cell Biol*. **17**, 559–564 (2005).

44. V. Gensbittel, M. Kräter, S. Harlepp, I. Busnelli, J. Guck, J. G. Goetz, Mechanical Adaptability of Tumor Cells in Metastasis. *Dev Cell*. **56**, 164–179 (2021).

45. W. J. Polacheck, I. K. Zervantonakis, R. D. Kamm, Tumor cell migration in complex microenvironments. *Cell Mol Life Sci*. **70**, 1335 (2013).

46. I. Pastushenko, C. Blanpain, EMT Transition States during Tumor Progression and Metastasis. *Trends Cell Biol*. **29**, 212–226 (2019).

47. R. K. Jain, J. D. Martin, T. Stylianopoulos, The role of mechanical forces in tumor growth and therapy. *Annu Rev Biomed Eng*. **16**, 321 (2014).

48. M. A. Nieto, R. Y. Y. J. Huang, R. A. A. Jackson, J. P. P. Thiery, EMT: 2016. *Cell*. **166**, 21–45 (2016).

49. J. A. Mitchel, A. Das, M. J. O'Sullivan, I. T. Stancil, S. J. DeCamp, S. Koehler, O. H. Ocaña, J. P. Butler, J. J. Fredberg, M. A. Nieto, D. Bi, J. A. Park, In primary airway epithelial cells, the unjamming transition is distinct from the epithelial-to-mesenchymal transition. *Nature Communications 2020 11:1*. **11**, 1–14 (2020).

50. O. Ilina, P. G. Gritsenko, S. Syga, J. Lippoldt, C. A. M. La Porta, O. Chepizhko, S. Grosser, M. Vullings, G. J. Bakker, J. Starruß, P. Bult, S. Zapperi, J. A. Käs, A. Deutsch, P. Friedl, Cell–cell adhesion and 3D matrix confinement determine jamming transitions in breast cancer invasion. *Nature Cell Biology 2020 22:9*. **22**, 1103–1115 (2020).

51. A. D. Doyle, R. J. Petrie, M. L. Kutys, K. M. Yamada, Dimensions in cell migration. *Curr Opin Cell Biol*. **25** (2013), pp. 642–649.

52. A. Saraswathibhatla, J. Notbohm, Tractions and Stress Fibers Control Cell Shape and Rearrangements in Collective Cell Migration. *Phys Rev X*. **10**, 011016 (2020).

53. G. F. Le Bras, K. J. Taubenslag, C. D. Andl, The regulation of cell-cell adhesion during epithelial-mesenchymal transition, motility and tumor progression. *Cell Adh Migr*. **6**, 365 (2012).

54. M. K. Driscoll, G. Danuser, Quantifying Modes of 3D Cell Migration. *Trends Cell Biol*. **25**, 749–759 (2015).

55. A. Pawluchin, M. Galic, Moving through a changing world: Single cell migration in 2D vs. 3D. *Front Cell Dev Biol*. **10**, 1080995 (2022).

56. A. Pathak, S. Kumar, Biophysical regulation of tumor cell invasion: moving beyond matrix stiffness. *Integrative Biology*. **3**, 267–278 (2011).

57. K. M. Yamada, A. D. Doyle, J. Lu, Cell–3D matrix interactions: recent advances and opportunities. *Trends Cell Biol*. **32**, 883–895 (2022).

58. B. M. Baker, C. S. Chen, Deconstructing the third dimension – how 3D culture microenvironments alter cellular cues. *J Cell Sci*. **125**, 3015 (2012).

59. S. Van Helvert, C. Storm, P. Friedl, Mechanoreciprocity in cell migration. *Nat Cell Biol*. **20**, 8 (2018).

60. M. Krause, K. Wolf, Cancer cell migration in 3D tissue: Negotiating space by proteolysis and nuclear deformability. *Cell Adh Migr*. **9**, 357 (2015).

61. C. Denais, J. Lammerding, Nuclear Mechanics in Cancer. *Adv Exp Med Biol*. **773**, 435 (2014).

62. D. S. Reynolds, K. M. Tevis, W. A. Blessing, Y. L. Colson, M. H. Zaman, M. W. Grinstaff, Breast Cancer Spheroids Reveal a Differential Cancer Stem Cell Response to Chemotherapeutic Treatment. *Sci Rep*. **7**, 10382–10382 (2017).

63. K. M. Yamada, M. Sixt, Mechanisms of 3D cell migration. *Nature Reviews Molecular Cell Biology 2019 20:12*. **20**, 738–752 (2019).

64. N. Gjorevski, A. S. Piotrowski, V. D. Varner, C. M. Nelson, Dynamic tensile forces drive collective cell migration through three-dimensional extracellular matrices. *Scientific Reports*

2015 5:1. **5**, 1–13 (2015).

65. P. T. Caswell, T. Zech, Actin-Based Cell Protrusion in a 3D Matrix. *Trends Cell Biol*. **28**, 823–834 (2018).

66. T. Lämmermann, M. Sixt, Mechanical modes of 'amoeboid' cell migration. *Curr Opin Cell Biol*. **21**, 636–644 (2009).

67. D. Vesperini, G. Montalvo, B. Qu, F. Lautenschläger, Characterization of immune cell migration using microfabrication. *Biophys Rev*. **13**, 185 (2021).

68. K. Paňková, D. Rösel, M. Novotný, J. Brábek, The molecular mechanisms of transition between mesenchymal and amoeboid invasiveness in tumor cells. *Cellular and Molecular Life Sciences*. **67**, 63 (2010).

69. R. J. Petrie, K. M. Yamada, At the leading edge of three-dimensional cell migration. *J Cell Sci*. **125**, 5917 (2012).

70. R. J. Petrie, N. Gavara, R. S. Chadwick, K. M. Yamada, Nonpolarized signaling reveals two distinct modes of 3D cell migration. *Journal of Cell Biology*. **197**, 439–455 (2012).

71. A. S. Khoo, T. M. Valentin, S. E. Leggett, D. Bhaskar, E. M. Bye, S. Benmelech, B. C. Ip, I. Y. Wong, Breast Cancer Cells Transition from Mesenchymal to Amoeboid Migration in Tunable Three-Dimensional Silk-Collagen Hydrogels. *ACS Biomater Sci Eng*. **5**, 4341–4354 (2019).

72. S. Pawlizak, A. W. Fritsch, S. Grosser, D. Ahrens, T. Thalheim, S. Riedel, T. R. Kießling, L. Oswald, M. Zink, M. L. Manning, J. A. Käs, Testing the differential adhesion hypothesis across the epithelial−mesenchymal transition. *New J Phys*. **17**, 083049 (2015).

73. M. Skamrahl, J. Schünemann, M. Mukenhirn, H. Pang, J. Gottwald, M. Jipp, M. Ferle, A. Rübeling, T. A. Oswald, A. Honigmann, A. Janshoff, Cellular segregation in cocultures is

driven by differential adhesion and contractility on distinct timescales. *Proc Natl Acad Sci U S A*. **120**, e2213186120 (2023).

74. R. A. Foty, M. S. Steinberg, The differential adhesion hypothesis: a direct evaluation. *Dev Biol*. **278**, 255–263 (2005).

75. M. S. Steinberg, Differential adhesion in morphogenesis: a modern view. *Curr Opin Genet Dev*. **17**, 281–286 (2007).

76. T. Fuhs, F. Wetzel, A. W. Fritsch, X. Li, R. Stange, S. Pawlizak, T. R. Kießling, E. Morawetz, S. Grosser, F. Sauer, J. Lippoldt, F. Renner, S. Friebe, M. Zink, K. Bendrat, J. Braun, M. H. Oktay, J. Condeelis, S. Briest, B. Wolf, L. C. Horn, M. Höckel, B. Aktas, M. C. Marchetti, M. L. Manning, A. Niendorf, D. Bi, J. A. Käs, Rigid tumours contain soft cancer cells. *Nature Physics 2022 18:12*. **18**, 1510–1519 (2022).

77. R. C. Boot, G. H. Koenderink, P. E. Boukany, Spheroid mechanics and implications for cell invasion. *https://doi.org/10.1080/23746149.2021.1978316*. **6** (2021), doi:10.1080/23746149.2021.1978316.

78. A. J. Kabla, Collective cell migration: leadership, invasion and segregation. *J R Soc Interface*. **9**, 3268 (2012).

79. S. Raghuraman, A. S. Schubert, S. Bröker, A. Jurado, A. Müller, M. Brandt, B. E. Vos, A. D. Hofemeier, F. Abbasi, M. Stehling, R. Wittkowski, J. Ivaska, T. Betz, Pressure Drives Rapid Burst-Like Coordinated Cellular Motion from 3D Cancer Aggregates. *Advanced Science*. **9**, 2104808 (2022).

80. P. Purkayastha, M. K. Jaiswal, T. P. Lele, Molecular cancer cell responses to solid compressive stress and interstitial fluid pressure. *Cytoskeleton*. **78**, 312–322 (2021).

81. K. Białkowska, P. Komorowski, M. Bryszewska, K. Miłowska, Spheroids as a Type of

Three-Dimensional Cell Cultures—Examples of Methods of Preparation and the Most Important Application. *Int J Mol Sci*. **21**, 1–17 (2020).

82. S. Lagies, M. Schlimpert, S. Neumann, A. Wäldin, B. Kammerer, C. Borner, L. Peintner, Cells grown in three-dimensional spheroids mirror in vivo metabolic response of epithelial cells. *Communications Biology 2020 3:1*. **3**, 1–10 (2020).

83. A. J. McKenzie, S. R. Hicks, K. V. Svec, H. Naughton, Z. L. Edmunds, A. K. Howe, The mechanical microenvironment regulates ovarian cancer cell morphology, migration, and spheroid disaggregation. *Scientific Reports 2018 8:1*. **8**, 1–20 (2018).

84. B. Pinto, A. C. Henriques, P. M. A. Silva, H. Bousbaa, Three-Dimensional Spheroids as In Vitro Preclinical Models for Cancer Research. *Pharmaceutics*. **12**, 1–38 (2020).

85. G. Mehta, A. Y. Hsiao, M. Ingram, G. D. Luker, S. Takayama, Opportunities and Challenges for use of Tumor Spheroids as Models to Test Drug Delivery and Efficacy. *J Control Release*. **164**, 192 (2012).

86. M. Zanoni, F. Piccinini, C. Arienti, A. Zamagni, S. Santi, R. Polico, A. Bevilacqua, A. Tesei, 3D tumor spheroid models for in vitro therapeutic screening: a systematic approach to enhance the biological relevance of data obtained. *Sci Rep*. **6** (2016), doi:10.1038/SREP19103.

87. B. C. Low, C. Q. Pan, G. V. Shivashankar, A. Bershadsky, M. Sudol, M. Sheetz, YAP/TAZ as mechanosensors and mechanotransducers in regulating organ size and tumor growth. *FEBS Lett*. **588**, 2663–2670 (2014).

88. J. Y. Lee, J. K. Chang, A. A. Dominguez, H. pyo Lee, S. Nam, J. Chang, S. Varma, L. S. Qi, R. B. West, O. Chaudhuri, YAP-independent mechanotransduction drives breast cancer progression. *Nature Communications 2019 10:1*. **10**, 1–9 (2019).

89. H. Okuyama, J. Kondo, Y. Sato, H. Endo, A. Nakajima, J. M. Piulats, Y. Tomita, T. Fujiwara, Y. Itoh, A. Mizoguchi, M. Ohue, M. Inoue, Dynamic Change of Polarity in Primary Cultured Spheroids of Human Colorectal Adenocarcinoma and Its Role in Metastasis. *Am J Pathol*. **186**, 899–911 (2016).

90. R. Baghban, L. Roshangar, R. Jahanban-Esfahlan, K. Seidi, A. Ebrahimi-Kalan, M. Jaymand, S. Kolahian, T. Javaheri, P. Zare, Tumor microenvironment complexity and therapeutic implications at a glance. *Cell Communication and Signaling 2020 18:1*. **18**, 1–19 (2020).

91. H. Zhou, M. Wang, Y. Zhang, Q. Su, Z. Xie, X. Chen, R. Yan, P. Li, T. Li, X. Qin, H. Yang, C. Wu, F. You, S. Li, Y. Liu, Functions and clinical significance of mechanical tumor microenvironment: cancer cell sensing, mechanobiology and metastasis. *Cancer Commun*. **42**, 374–400 (2022).

92. V. Salvatore, G. Teti, S. Focaroli, M. C. Mazzotti, A. Mazzotti, M. Falconi, The tumor microenvironment promotes cancer progression and cell migration. *Oncotarget*. **8**, 9608 (2017).

93. Y. Wang, K. F. Goliwas, P. E. Severino, K. P. Hough, D. Van Vessem, H. Wang, S. Tousif, R. P. Koomullil, A. R. Frost, S. Ponnazhagan, J. L. Berry, J. S. Deshane, Mechanical strain induces phenotypic changes in breast cancer cells and promotes immunosuppression in the tumor microenvironment. *Laboratory Investigation 2020 100:12*. **100**, 1503–1516 (2020).

94. E. Henke, R. Nandigama, S. Ergün, Extracellular Matrix in the Tumor Microenvironment and Its Impact on Cancer Therapy. *Front Mol Biosci*. **6**, 160 (2019).

95. M. W. Pickup, J. K. Mouw, V. M. Weaver, The extracellular matrix modulates the hallmarks of cancer. *EMBO Rep*. **15**, 1243 (2014).

96. Q. Liu, Q. Luo, Y. Ju, G. Song, Role of the mechanical microenvironment in cancer

development and progression. *Cancer Biol Med*. **17**, 282 (2020).

97. J. L. Guan, Role of focal adhesion kinase in integrin signaling. *Int J Biochem Cell Biol*. **29**, 1085–1096 (1997).

98. M. J. Paszek, N. Zahir, K. R. Johnson, J. N. Lakins, G. I. Rozenberg, A. Gefen, C. A. Reinhart-King, S. S. Margulies, M. Dembo, D. Boettiger, D. A. Hammer, V. M. Weaver, Tensional homeostasis and the malignant phenotype. *Cancer Cell*. **8**, 241–254 (2005).

99. P. A. Janmey, D. A. Fletcher, C. A. Reinhart-King, Stiffness Sensing by Cells. *Physiol Rev*. **100**, 695 (2020).

100. J. Winkler, A. Abisoye-Ogunniyan, K. J. Metcalf, Z. Werb, Concepts of extracellular matrix remodelling in tumour progression and metastasis. *Nature Communications 2020 11:1*. **11**, 1–19 (2020).

101. P. Lu, K. Takai, V. M. Weaver, Z. Werb, Extracellular Matrix Degradation and Remodeling in Development and Disease. *Cold Spring Harb Perspect Biol*. **3** (2011), doi:10.1101/CSHPERSPECT.A005058.

102. C. Bonnans, J. Chou, Z. Werb, Remodelling the extracellular matrix in development and disease. *Nat Rev Mol Cell Biol*. **15**, 786 (2014).

103. C. Hoffmann, N. E. H. Djerir, A. Danckaert, J. Fernandes, P. Roux, C. Charrueau, A. M. Lachagès, F. Charlotte, I. Brocheriou, K. Clément, J. Aron-Wisnewsky, F. Foufelle, V. Ratziu, B. Hainque, D. Bonnefont-Rousselot, P. Bigey, V. Escriou, Hepatic stellate cell hypertrophy is associated with metabolic liver fibrosis. *Scientific Reports 2020 10:1*. **10**, 1–13 (2020).

104. R. Gauvin, R. Parenteau-Bareil, M. R. Dokmeci, W. D. Merryman, A. Khademhosseini, Hydrogels and microtechnologies for engineering the cellular microenvironment. *Wiley*

Interdiscip Rev Nanomed Nanobiotechnol. **4**, 235–246 (2012).

105. S. R. Caliari, J. A. Burdick, A practical guide to hydrogels for cell culture. *Nature Methods 2016 13:5*. **13**, 405–414 (2016).

106. M. W. Tibbitt, K. S. Anseth, Hydrogels as Extracellular Matrix Mimics for 3D Cell Culture. *Biotechnol Bioeng*. **103**, 655 (2009).

107. S. Maji, H. Lee, Engineering Hydrogels for the Development of Three-Dimensional In Vitro Models. *International Journal of Molecular Sciences 2022, Vol. 23, Page 2662*. **23**, 2662 (2022).

108. K. Wolf, S. Alexander, V. Schacht, L. M. Coussens, U. H. von Andrian, J. van Rheenen, E. Deryugina, P. Friedl, Collagen-based cell migration models in vitro and in vivo. *Semin Cell Dev Biol*. **20** (2009), pp. 931–941.

109. A. Jabłońska-Trypuć, M. Matejczyk, S. Rosochacki, A. J. Jabłon´, J.-T. Trypuc´, Matrix metalloproteinases (MMPs), the main extracellular matrix (ECM) enzymes in collagen degradation, as a target for anticancer drugs. *https://doi.org/10.3109/14756366.2016.1161620*. **31**, 177–183 (2016).

110. X. Li, Q. Sun, Q. Li, N. Kawazoe, G. Chen, Functional hydrogels with tunable structures and properties for tissue engineering applications. *Front Chem*. **6**, 417160 (2018).

111. J. Zhu, Bioactive Modification of Poly(ethylene glycol) Hydrogels for Tissue Engineering. *Biomaterials*. **31**, 4639 (2010).

112. E. E. Charrier, K. Pogoda, R. Li, C. Y. Park, J. J. Fredberg, P. A. Janmey, A novel method to make viscoelastic polyacrylamide gels for cell culture and traction force microscopy. *APL Bioeng*. **4**, 36104 (2020).

113. C. Liu, D. Lewin Mejia, B. Chiang, K. E. Luker, G. D. Luker, Hybrid collagen alginate

hydrogel as a platform for 3D tumor spheroid invasion. *Acta Biomater*. **75**, 213–225 (2018).

114. U. S. K. Madduma-Bandarage, S. V. Madihally, Synthetic hydrogels: Synthesis, novel trends, and applications. *J Appl Polym Sci*. **138**, 50376 (2021).

115. V. Ajeti, A. P. Tabatabai, A. J. Fleszar, M. F. Staddon, D. S. Seara, C. Suarez, M. S. Yousafzai, D. Bi, D. R. Kovar, S. Banerjee, M. P. Murrell, Wound healing coordinates actin architectures to regulate mechanical work. *Nat Phys*. **15**, 696–705 (2019).

116. R. Staneva, F. El Marjou, J. Barbazan, D. Krndija, S. Richon, A. G. Clark, D. M. Vignjevic, Cancer cells in the tumor core exhibit spatially coordinated migration patterns. *J Cell Sci*. **132** (2019), doi:10.1242/JCS.220277/VIDEO-3.

117. S. Grosser, J. Lippoldt, L. Oswald, M. Merkel, D. M. Sussman, F. Renner, P. Gottheil, E. W. Morawetz, T. Fuhs, X. Xie, S. Pawlizak, A. W. Fritsch, B. Wolf, L. C. Horn, S. Briest, B. Aktas, M. L. Manning, J. A. Kas, Cell and Nucleus Shape as an Indicator of Tissue Fluidity in Carcinoma. *Phys Rev X*. **11**, 011033 (2021).

118. J. M. Northcott, I. S. Dean, J. K. Mouw, V. M. Weaver, Feeling Stress: The Mechanics of Cancer Progression and Aggression. *Front Cell Dev Biol*. **6**, 17 (2018).

119. P. Friedl, S. Alexander, Cancer invasion and the microenvironment: Plasticity and reciprocity. *Cell*. **147** (2011), pp. 992–1009.

120. D. Bi, J. H. Lopez, J. M. Schwarz, M. Lisa Manning, Energy barriers and cell migration in densely packed tissues. *Soft Matter*. **10**, 1885–1890 (2014).

121. R. Farhadifar, J. C. Röper, B. Aigouy, S. Eaton, F. Jülicher, The Influence of Cell Mechanics, Cell-Cell Interactions, and Proliferation on Epithelial Packing. *Current Biology*. **17**, 2095–2104 (2007).

122. G. Charras, A. S. Yap, Tensile Forces and Mechanotransduction at Cell–Cell Junctions.

Current Biology. **28**, R445–R457 (2018).

123. P. Kanchanawong, G. Shtengel, A. M. Pasapera, E. B. Ramko, M. W. Davidson, H. F. Hess, C. M. Waterman, Nanoscale architecture of integrin-based cell adhesions. *Nature*. **468**, 580–584 (2010).

124. J. M. Tse, G. Cheng, J. A. Tyrrell, S. A. Wilcox-Adelman, Y. Boucher, R. K. Jain, L. L. Munn, Mechanical compression drives cancer cells toward invasive phenotype. *Proceedings of the National Academy of Sciences*. **109**, 911–916 (2012).

125. C. Malinverno, S. Corallino, F. Giavazzi, M. Bergert, Q. Li, M. Leoni, A. Disanza, E. Frittoli, A. Oldani, E. Martini, T. Lendenmann, G. Deflorian, G. v. Beznoussenko, D. Poulikakos, K. H. Ong, M. Uroz, X. Trepat, D. Parazzoli, P. Maiuri, W. Yu, A. Ferrari, R. Cerbino, G. Scita, Endocytic reawakening of motility in jammed epithelia. *Nat Mater*. **16**, 587–596 (2017).

126. E. G. Rens, R. M. H. Merks, Cell Shape and Durotaxis Explained from Cell-Extracellular Matrix Forces and Focal Adhesion Dynamics. *iScience*. **23**, 101488 (2020).

127. J. M. Muncie, N. M. E. Ayad, J. N. Lakins, X. Xue, J. Fu, V. M. Weaver, Mechanical Tension Promotes Formation of Gastrulation-like Nodes and Patterns Mesoderm Specification in Human Embryonic Stem Cells. *Dev Cell*. **55**, 679-694.e11 (2020).

128. M. Luo, G. Cai, K. K. Y. Ho, K. Wen, Z. Tong, L. Deng, A. P. Liu, Compression enhances invasive phenotype and matrix degradation of breast Cancer cells via Piezo1 activation. *BMC Mol Cell Biol*. **23**, 1–17 (2022).

129. M. Deforet, M. C. Parrini, L. Petitjean, M. Biondini, A. Buguin, J. Camonis, P. Silberzan, Automated velocity mapping of migrating cell populations (AVeMap). *Nat Methods*. **9**, 1081–1083 (2012).

130. Y. Bashirzadeh, S. Chatterji, D. Palmer, S. Dumbali, S. Qian, V. Maruthamuthu, Stiffness

Measurement of Soft Silicone Substrates for Mechanobiology Studies Using a Widefield Fluorescence Microscope. *JoVE (Journal of Visualized Experiments)*. **2018**, e57797 (2018).

131. Y. Bashirzadeh, S. Qian, V. Maruthamuthu, Non-intrusive measurement of wall shear stress in flow channels. *Sens Actuators A Phys*. **271**, 118–123 (2018).

132. X. Tan, J. Heureaux, A. P. Liu, Cell Spreading Area Regulates Clathrin-Coated Pit Dynamics on Micropatterned Substrate. *Integr Biol (Camb)*. **7**, 1033 (2015).

133. W. Thielicke, E. J. Stamhuis, PIVlab – Towards User-friendly, Affordable and Accurate Digital Particle Image Velocimetry in MATLAB. *J Open Res Softw*. **2** (2014), doi:10.5334/JORS.BL.

134. Y. Bashirzadeh, S. Dumbali, S. Qian, V. Maruthamuthu, Mechanical Response of an Epithelial Island Subject to Uniaxial Stretch on a Hybrid Silicone Substrate. *Cell Mol Bioeng*. **12**, 33 (2019).

135. J. P. Butler, I. M. Toli-Nørrelykke, B. Fabry, J. J. Fredberg, Traction fields, moments, and strain energy that cells exert on their surroundings. *Am J Physiol Cell Physiol*. **282**, 595–605 (2002).

136. S. V. Plotnikov, B. Sabass, U. S. Schwarz, C. M. Waterman, High-Resolution Traction Force Microscopy. *Methods Cell Biol*. **123**, 367 (2014).

137. B. Sabass, M. L. Gardel, C. M. Waterman, U. S. Schwarz, High Resolution Traction Force Microscopy Based on Experimental and Computational Advances. *Biophys J*. **94**, 207 (2008).

138. U. S. Schwarz, N. Q. Balaban, D. Riveline, A. Bershadsky, B. Geiger, S. A. Safran, Calculation of forces at focal adhesions from elastic substrate data: the effect of localized force and the need for regularization. *Biophys J*. **83**, 1380 (2002).

139. D. M. Sussman, cellGPU: Massively parallel simulations of dynamic vertex models. *Comput*

Phys Commun. **219**, 400–406 (2017).

140. K. Tao, M. Fang, J. Alroy, G. G. Gary, Imagable 4T1 model for the study of late stage breast cancer. *BMC Cancer*. **8**, 1–19 (2008).

141. S. Yang, J. J. Zhang, X. Y. Huang, Mouse Models for Tumor Metastasis. *Methods Mol Biol*. **928**, 221 (2012).

142. B. Schrörs, S. Boegel, C. Albrecht, T. Bukur, V. Bukur, C. Holtsträter, C. Ritzel, K. Manninen, A. D. Tadmor, M. Vormehr, U. Sahin, M. Löwer, Multi-Omics Characterization of the 4T1 Murine Mammary Gland Tumor Model. *Front Oncol*. **10**, 1195 (2020).

143. C. Denais, J. Lammerding, Nuclear Mechanics in Cancer. *Adv Exp Med Biol*. **773**, 435 (2014).

144. T. Fischer, A. Hayn, C. T. Mierke, Effect of Nuclear Stiffness on Cell Mechanics and Migration of Human Breast Cancer Cells. *Front Cell Dev Biol*. **8** (2020), doi:10.3389/FCELL.2020.00393/FULL.

145. C. Rianna, M. Radmacher, S. Kumar, Direct evidence that tumor cells soften when navigating confined spaces. *Mol Biol Cell*. **31**, 1726 (2020).

146. A. B. Roberts, J. Zhang, V. Raj Singh, M. Nikolić, E. Moeendarbary, R. D. Kamm, P. T. C. So, G. Scarcelli, Tumor cell nuclei soften during transendothelial migration. *J Biomech*. **121**, 110400 (2021).

147. P. Friedl, K. Wolf, J. Lammerding, Nuclear mechanics during cell migration. *Curr Opin Cell Biol*. **23**, 55–64 (2011).

148. A. M. Mendonsa, T.-Y. Na, B. M. Gumbiner, E-cadherin in contact inhibition and cancer. *Oncogene 2018 37:35*. **37**, 4769–4780 (2018).

149. D. M. Dykxhoorn, Y. Wu, H. Xie, F. Yu, A. Lal, F. Petrocca, D. Martinvalet, E. Song, B.

Lim, J. Lieberman, miR-200 Enhances Mouse Breast Cancer Cell Colonization to Form Distant Metastases. *PLoS One*. **4**, e7181 (2009).

150. L. Balasubramaniam, A. Doostmohammadi, T. B. Saw, G. H. N. S. Narayana, R. Mueller, T. Dang, M. Thomas, S. Gupta, S. Sonam, A. S. Yap, Y. Toyama, R. M. Mège, J. M. Yeomans, B. Ladoux, Investigating the nature of active forces in tissues reveals how contractile cells can form extensile monolayers. *Nat Mater*, 1–11 (2021).

151. J. P. Thiery, H. Acloque, R. Y. J. Huang, M. A. Nieto, Epithelial-Mesenchymal Transitions in Development and Disease. *Cell*. **139**, 871–890 (2009).

152. M. K. Jolly, K. E. Ware, S. Gilja, J. A. Somarelli, H. Levine, EMT and MET: necessary or permissive for metastasis? *Mol Oncol*. **11**, 755–769 (2017).

153. S. Varadarajan, S. A. Chumki, R. E. Stephenson, E. R. Misterovich, J. L. Wu, C. E. Dudley, I. S. Erofeev, A. B. Goryachev, A. L. Miller, Mechanosensitive calcium flashes promote sustained RhoA activation during tight junction remodeling. *Journal of Cell Biology*. **221** (2022), doi:10.1083/JCB.202105107.

154. D. Pinheiro, Y. Bellaïche, Mechanical Force-Driven Adherens Junction Remodeling and Epithelial Dynamics. *Dev Cell*. **47**, 3–19 (2018).

155. N. Borghi, M. Sorokina, O. G. Shcherbakova, W. I. Weis, B. L. Pruitt, W. J. Nelson, A. R. Dunn, E-cadherin is under constitutive actomyosin-generated tension that is increased at cell-cell contacts upon externally applied stretch. *Proc Natl Acad Sci U S A.* **109**, 12568–12573 (2012).

156. J. Wang, J. Jiang, X. Yang, G. Zhou, L. Wang, B. Xiao, Tethering Piezo channels to the actin cytoskeleton for mechanogating via the cadherin-β-catenin mechanotransduction complex. *Cell Rep*. **38**, 110342 (2022).

157. A. P. Kowalczyk, B. A. Nanes, Adherens junction turnover: regulating adhesion through cadherin endocytosis, degradation, and recycling. *Subcell Biochem*. **60**, 197 (2012).

158. N. M. Willy, J. P. Ferguson, S. D. Huber, S. P. Heidotting, E. Aygün, S. A. Wurm, E. Johnston-Halperin, M. G. Poirier, C. Kural, Membrane mechanics govern spatiotemporal heterogeneity of endocytic clathrin coat dynamics. *Mol Biol Cell*. **28**, 3480 (2017).

159. X. S. Wu, S. Elias, H. Liu, J. Heureaux, P. J. Wen, A. P. Liu, M. M. Kozlov, L. G. Wu, Membrane Tension Inhibits Rapid and Slow Endocytosis in Secretory Cells. *Biophys J*. **113**, 2406 (2017).

160. L. M. Lee, A. P. Liu, A microfluidic pipette array for mechanophenotyping of cancer cells and mechanical gating of mechanosensitive channels. *Lab Chip*. **15**, 264 (2015).

161. C. Alibert, B. Goud, J. B. Manneville, Are cancer cells really softer than normal cells? *Biol Cell*. **109**, 167–189 (2017).

162. T. Déjardin, P. S. Carollo, F. Sipieter, P. M. Davidson, C. Seiler, D. Cuvelier, B. Cadot, C. Sykes, E. R. Gomes, N. Borghi, Nesprins are mechanotransducers that discriminate epithelial–mesenchymal transition programs. *J Cell Biol*. **219** (2020), doi:10.1083/JCB.201908036.

163. F. Van Zijl, G. Krupitza, W. Mikulits, Initial steps of metastasis: Cell invasion and endothelial transmigration. *Mutat Res*. **728**, 23 (2011).

164. J. Fares, M. Y. Fares, H. H. Khachfe, H. A. Salhab, Y. Fares, Molecular principles of metastasis: a hallmark of cancer revisited. *Signal Transduction and Targeted Therapy 2020 5:1*. **5**, 1–17 (2020).

165. J. M. Northcott, I. S. Dean, J. K. Mouw, V. M. Weaver, Feeling Stress: The Mechanics of Cancer Progression and Aggression. *Front Cell Dev Biol*. **6**, 17 (2018).

166. H. Yan, D. Ramirez-Guerrero, J. Lowengrub, M. Wu, Stress generation, relaxation and size control in confined tumor growth. *PLoS Comput Biol*. **17**, e1009701 (2021).

167. A. F. Mertz, Y. Che, S. Banerjee, J. M. Goldstein, K. A. Rosowski, S. F. Revilla, C. M. Niessen, M. C. Marchetti, E. R. Dufresne, V. Horsley, Cadherin-based intercellular adhesions organize epithelial cell-matrix traction forces. *Proc Natl Acad Sci U S A*. **110**, 842–847 (2013).

168. T. Lecuit, A. S. Yap, E-cadherin junctions as active mechanical integrators in tissue dynamics. *Nature Cell Biology 2015 17:5*. **17**, 533–539 (2015).

169. Y. Kang, J. Massagué, Epithelial-mesenchymal transitions: Twist in development and metastasis. *Cell*. **118**, 277–279 (2004).

170. J. F. Lima, S. Nofech-Mozes, J. Bayani, J. M. S. Bartlett, EMT in Breast Carcinoma—A Review. *Journal of Clinical Medicine 2016, Vol. 5, Page 65*. **5**, 65 (2016).

171. D. Hanahan, R. A. Weinberg, The Hallmarks of Cancer. *Cell*. **100**, 57–70 (2000).

172. D. P. Tabassum, K. Polyak, Tumorigenesis: it takes a village. *Nature Reviews Cancer 2015 15:8*. **15**, 473–483 (2015).

173. K. J. Cheung, E. Gabrielson, Z. Werb, A. J. Ewald, Collective Invasion in Breast Cancer Requires a Conserved Basal Epithelial Program. *Cell*. **155**, 1639 (2013).

174. K. J. Cheung, A. J. Ewald, Illuminating breast cancer invasion: diverse roles for cell–cell interactions. *Curr Opin Cell Biol*. **30**, 99 (2014).

175. L. Perrin, E. Belova, B. Bayarmagnai, E. Tüzel, B. Gligorijevic, Invadopodia enable cooperative invasion and metastasis of breast cancer cells. *Communications Biology 2022 5:1*. **5**, 1–14 (2022).

176. A. Huttenlocher, A. R. Horwitz, Integrins in Cell Migration. *Cold Spring Harb Perspect Biol*.

3, 1–16 (2011).

177. C. M. Lo, H. B. Wang, M. Dembo, Y. L. Wang, Cell Movement Is Guided by the Rigidity of the Substrate. *Biophys J*. **79**, 144–152 (2000).

178. A. Saez, M. Ghibaudo, A. Buguin, P. Silberzan, B. Ladoux, Rigidity-driven growth and migration of epithelial cells on microstructured anisotropic substrates. *Proc Natl Acad Sci U S A*. **104**, 8281–8286 (2007).

179. M. R. Ng, A. Besser, G. Danuser, J. S. Brugge, Substrate stiffness regulates cadherin-dependent collective migration through myosin-II contractility. *Journal of Cell Biology*. **199**, 545–563 (2012).

180. B. Sun, The mechanics of fibrillar collagen extracellular matrix. *Cell Rep Phys Sci*. **2** (2021), doi:10.1016/j.xcrp.2021.100515.

181. T. Hu, A. C. Y. Lo, Collagen–Alginate Composite Hydrogel: Application in Tissue Engineering and Biomedical Sciences. *Polymers (Basel)*. **13** (2021), doi:10.3390/POLYM13111852.

182. G. E. Wheeler, A. Purkayastha, E. N. Bunker, D. M. Bortz, X. Liu, Protocol for Analysis and Consolidation of TrackMate Outputs for Measuring Two-Dimensional Cell Motility using Nuclear Tracking. *J Vis Exp*. **2021** (2021), doi:10.3791/62885.

183. N. Tarantino, J. Y. Tinevez, E. F. Crowell, B. Boisson, R. Henriques, M. Mhlanga, F. Agou, A. Israël, E. Laplantine, Tnf and il-1 exhibit distinct ubiquitin requirements for inducing NEMO-IKK supramolecular structures. *Journal of Cell Biology*. **204**, 231–245 (2014).

184. D. M. Sussman, cellGPU: Massively parallel simulations of dynamic vertex models. *Comput Phys Commun*. **219**, 400–406 (2017).

185. T. Nagai, H. Honda, A dynamic cell model for the formation of epithelial tissues.

https://doi.org/10.1080/13642810108205772. **81**, 699–719 (2009).

186. L. Hufnagel, A. A. Teleman, H. Rouault, S. M. Cohen, B. I. Shraiman, On the mechanism of wing size determination in fly development. *Proc Natl Acad Sci U S A*. **104**, 3835–3840 (2007).

187. R. Farhadifar, J. C. Röper, B. Aigouy, S. Eaton, F. Jülicher, The Influence of Cell Mechanics, Cell-Cell Interactions, and Proliferation on Epithelial Packing. *Current Biology*. **17**, 2095–2104 (2007).

188. D. B. Staple, R. Farhadifar, J. C. Röper, B. Aigouy, S. Eaton, F. Jülicher, Mechanics and remodelling of cell packings in epithelia. *The European Physical Journal E 2010 33:2*. **33**, 117–127 (2010).

189. A. G. Fletcher, M. Osterfield, R. E. Baker, S. Y. Shvartsman, Vertex Models of Epithelial Morphogenesis. *Biophys J*. **106**, 2291–2304 (2014).

190. X. Li, A. Das, D. Bi, Mechanical Heterogeneity in Tissues Promotes Rigidity and Controls Cellular Invasion. *Phys Rev Lett*. **123**, 058101 (2019).

191. A. Szabó, R. Ünnep, E. Méhes, W. O. Twal, W. S. Argraves, Y. Cao, A. Czirók, Collective cell motion in endothelial monolayers. *Phys Biol*. **7**, 046007 (2010).

192. S. Ishihara, K. Sugimura, Bayesian inference of force dynamics during morphogenesis. *J Theor Biol*. **313**, 201–211 (2012).

193. L. Yan, D. Bi, Multicellular Rosettes Drive Fluid-solid Transition in Epithelial Tissues. *Phys Rev X*. **9**, 011029 (2019).

194. Y. Shen, B. U. S. Schmidt, H. Kubitschke, E. W. Morawetz, B. Wolf, J. A. Käs, W. Losert, Detecting heterogeneity in and between breast cancer cell lines. *Cancer Convergence 2020 4:1*. **4**, 1–11 (2020).

195. M. H. Lee, P. H. Wu, J. R. Staunton, R. Ros, G. D. Longmore, D. Wirtz, Mismatch in Mechanical and Adhesive Properties Induces Pulsating Cancer Cell Migration in Epithelial Monolayer. *Biophys J*. **102**, 2731 (2012).

196. C. Liu, M. Li, Z. X. Dong, D. Jiang, X. Li, S. Lin, D. Chen, X. Zou, X. D. Zhang, G. D. Luker, Heterogeneous microenvironmental stiffness regulates pro-metastatic functions of breast cancer cells. *Acta Biomater*. **131**, 326–340 (2021).

197. H. T. Nia, L. L. Munn, R. K. Jain, Physical traits of cancer. *Science (1979)*. **370** (2020), doi:10.1126/SCIENCE.AAZ0868/ASSET/5D0A72D9-30DE-4D81-96F5-8D7E0B0B58B2/ASSETS/GRAPHIC/370_AAZ0868_F3.JPEG.

198. I. Gladukh, M. Podorozhna, Study of structural and mechanical properties of sodium alginate gels. *EUREKA: Health Sciences*, 82–89 (2021).

199. W. Lee, N. Kalashnikov, S. Mok, R. Halaoui, E. Kuzmin, A. J. Putnam, S. Takayama, M. Park, L. McCaffrey, R. Zhao, R. L. Leask, C. Moraes, Dispersible hydrogel force sensors reveal patterns of solid mechanical stress in multicellular spheroid cultures. *Nature Communications 2019 10:1*. **10**, 1–14 (2019).

200. H. T. Nia, H. Liu, G. Seano, M. Datta, D. Jones, N. Rahbari, J. Incio, V. P. Chauhan, K. Jung, J. D. Martin, V. Askoxylakis, T. P. Padera, D. Fukumura, Y. Boucher, F. J. Hornicek, A. J. Grodzinsky, J. W. Baish, L. L. Munn, R. K. Jain, Solid stress and elastic energy as measures of tumour mechanopathology. *Nature Biomedical Engineering 2016 1:1*. **1**, 1–11 (2016).

201. V. Gkretsi, T. Stylianopoulos, Cell Adhesion and Matrix Stiffness: Coordinating Cancer Cell Invasion and Metastasis. *Front Oncol*. **8**, 145 (2018).

202. L. Wullkopf, A. K. V. West, N. Leijnse, T. R. Cox, C. D. Madsen, L. B. Oddershede, J. T. Erler, Cancer cells' ability to mechanically adjust to extracellular matrix stiffness correlates

with their invasive potential. *Mol Biol Cell*. **29**, 2378 (2018).

203. M. Saitoh, Involvement of partial EMT in cancer progression. *The Journal of Biochemistry*. **164**, 257–264 (2018).

204. E. Batlle, D. G. Wilkinson, Molecular Mechanisms of Cell Segregation and Boundary Formation in Development and Tumorigenesis. *Cold Spring Harb Perspect Biol*. **4** (2012), doi:10.1101/CSHPERSPECT.A008227.

205. J. Heureaux-Torres, K. E. Luker, H. Haley, M. Pirone, L. M. Lee, Y. Herrera, G. D. Luker, A. P. Liu, The effect of mechanosensitive channel MscL expression in cancer cells on 3D confined migration. *APL Bioeng*. **2** (2018), doi:10.1063/1.5019770.

206. S. A. Gudipaty, J. Lindblom, P. D. Loftus, M. J. Redd, K. Edes, C. F. Davey, V. Krishnegowda, J. Rosenblatt, Mechanical stretch triggers rapid epithelial cell division through Piezo1. *Nature 2017 543:7643*. **543**, 118–121 (2017).

207. Y. Yu, X. Wu, S. Liu, H. Zhao, B. Li, H. Zhao, X. Feng, Piezo1 regulates migration and invasion of breast cancer cells via modulating cell mechanobiological properties. *Acta Biochim Biophys Sin (Shanghai)*. **53**, 10–18 (2020).

208. C. Li, S. Rezania, S. Kammerer, A. Sokolowski, T. Devaney, A. Gorischek, S. Jahn, H. Hackl, K. Groschner, C. Windpassinger, E. Malle, T. Bauernhofer, W. Schreibmayer, Piezo1 forms mechanosensitive ion channels in the human MCF-7 breast cancer cell line. *Sci Rep*. **5** (2015), doi:10.1038/SREP08364.

209. J. R. Holt, W. Z. Zeng, E. L. Evans, S. H. Woo, S. Ma, H. Abuwarda, M. Loud, A. Patapoutian, M. M. Pathak, Spatiotemporal dynamics of PIEZO1 localization controls keratinocyte migration during wound healing. *Elife*. **10** (2021), doi:10.7554/ELIFE.65415.

210. N. Srivastava, D. Traynor, M. Piel, A. J. Kabla, R. R. Kay, Pressure sensing through Piezo

channels controls whether cells migrate with blebs or pseudopods. *Proc Natl Acad Sci U S A.* **117**, 2506–2512 (2020).

211. J. Wang, J. Jiang, X. Yang, G. Zhou, L. Wang, B. Xiao, Tethering Piezo channels to the actin cytoskeleton for mechanogating via the cadherin-β-catenin mechanotransduction complex. *Cell Rep*. **38**, 110342 (2022).

212. M. Egeblad, E. S. Nakasone, Z. Werb, Tumors as organs: complex tissues that interface with the entire organism. *Dev Cell*. **18**, 884 (2010).

213. I. Dagogo-Jack, A. T. Shaw, Tumour heterogeneity and resistance to cancer therapies. *Nature Reviews Clinical Oncology 2017 15:2*. **15**, 81–94 (2017).

214. R. Fisher, L. Pusztai, C. Swanton, Cancer heterogeneity: implications for targeted therapeutics. *Br J Cancer*. **108**, 479 (2013).

215. E. L. Baker, J. Lu, D. Yu, R. T. Bonnecaze, M. H. Zaman, Cancer Cell Stiffness: Integrated Roles of Three-Dimensional Matrix Stiffness and Transforming Potential. *Biophys J*. **99**, 2048 (2010).

216. K. Seltmann, A. W. Fritsch, J. A. Käs, T. M. Magin, Keratins significantly contribute to cell stiffness and impact invasive behavior. *Proc Natl Acad Sci U S A.* **110**, 18507–18512 (2013).

217. R. C. Boot, A. Roscani, L. van Buren, S. Maity, G. H. Koenderink, P. E. Boukany, High-throughput mechanophenotyping of multicellular spheroids using a microfluidic micropipette aspiration chip. *Lab Chip*. **23**, 1768 (2023).

218. Y. L. Han, A. F. Pegoraro, H. Li, K. Li, Y. Yuan, G. Xu, Z. Gu, J. Sun, Y. Hao, S. K. Gupta, Y. Li, W. Tang, H. Kang, L. Teng, J. J. Fredberg, M. Guo, Cell swelling, softening and invasion in a three-dimensional breast cancer model. *Nature Physics 2019 16:1*. **16**, 101–108 (2019).

219. K. Bera, A. Kiepas, I. Godet, Y. Li, P. Mehta, B. Ifemembi, C. D. Paul, A. Sen, S. A. Serra, K. Stoletov, J. Tao, G. Shatkin, S. J. Lee, Y. Zhang, A. Boen, P. Mistriotis, D. M. Gilkes, J. D. Lewis, C. M. Fan, A. P. Feinberg, M. A. Valverde, S. X. Sun, K. Konstantopoulos, Extracellular fluid viscosity enhances cell migration and cancer dissemination. *Nature 2022 611:7935*. **611**, 365–373 (2022).

220. Q. Huang, X. Hu, W. He, Y. Zhao, S. Hao, Q. Wu, S. Li, S. Zhang, M. Shi, Fluid shear stress and tumor metastasis. *Am J Cancer Res*. **8**, 763 (2018).

221. M. Wu, H. B. Frieboes, S. R. McDougall, M. A. J. Chaplain, V. Cristini, J. Lowengrub, The effect of interstitial pressure on tumor growth: coupling with the blood and lymphatic vascular systems. *J Theor Biol*. **320**, 131 (2013).

222. A. Diz-Muñoz, D. A. Fletcher, O. D. Weiner, Use the force: Membrane tension as an organizer of cell shape and motility. *Trends Cell Biol*. **23**, 47 (2013).

223. E. Sitarska, A. Diz-Muñoz, Pay attention to membrane tension: Mechanobiology of the cell surface. *Curr Opin Cell Biol*. **66**, 11–18 (2020).

224. Y. Y. Hsu, A. M. Resto Irizarry, J. Fu, A. P. Liu, Mechanosensitive Channel-Based Optical Membrane Tension Reporter. *ACS Sens*. **8**, 12–18 (2023).